

# **HASP 2016**

## **Science Report of Payload # 7**

**University of North Florida and University of North Dakota**



## **Ozone Sensors Payload and its Applications (OSPA)**

**Students Team:**

**Jesse Lard (UNF) (Team Leader),**

**Christopher Farkas**

**and Kenneth Emanuel (Consultant)**

**Faculty Advisors:**

**Dr. Nirmalkumar G. Patel**

**Department of Physics, University of North Florida, Jacksonville, FL 32224**

**and**

**Dr. Ron Fevig**

**Department of Space Studies, University of North Dakota, Grand Forks, ND 58202**

# Index

<b>Section</b>	<b>Contents</b>	<b>Page</b>
<b>1</b>	Introduction and Mission Objectives	<b>3</b>
<b>2</b>	Fabrication of Nanocrystalline Thin Film Gas Sensors	<b>8</b>
<b>3</b>	Working Principles of Gas Sensors	<b>12</b>
<b>4</b>	Calibration of Gas Sensors	<b>14</b>
<b>5</b>	Fabrication of Payload Body	<b>18</b>
<b>6</b>	Electronic Circuits	<b>30</b>
<b>7</b>	Integration of Payload and Thermal Vacuum Test	<b>35</b>
<b>8</b>	Launching of Payload	<b>50</b>
<b>9</b>	Results and Discussions	<b>58</b>
<b>9.1</b>	How ozone profile measured?	<b>58</b>
<b>9.2</b>	Balloon Flight Profile and Response of Pressure Sensor	<b>59</b>
<b>9.3</b>	Power Budget during the Flight	<b>61</b>
<b>9.4</b>	Thermal Stability of the Payload	<b>62</b>
<b>9.5</b>	Measurements of Photovoltage Profile during the Flight	<b>66</b>
<b>9.6</b>	Discussion of Response of Gas Sensors Profiles	<b>70</b>
<b>9.7</b>	Response of Ozone Sensors during the Flight	<b>76</b>
<b>9.8</b>	Measurements of ozone profile in the stratosphere and comparison with the theoretical profile	<b>83</b>
<b>10</b>	Problems, Failure Analysis and Future Plan	<b>89</b>
<b>11</b>	Conclusions	<b>89</b>
<b>12</b>	Acknowledgements	<b>90</b>
<b>13</b>	Presentation of Research Work	<b>91</b>

## 1. Introduction and Mission Objectives

After success of the HASP flights made during 2008 to 2015, University of North Florida (UNF) and University of North Dakota (UND) team decided to go for the HASP2016 balloon flight to measure the ozone profile in the stratosphere again using an improved and smaller version of payload consist of the nanocomposite ozone gas and reducing gases sensors, the pressure sensor, GPS and improved version of software and microcontroller circuit. About 90% of ozone is concentrated between 15 and 32 kilometers above the earth's surface (stratospheric ozone). It is also found at ground level in lower concentrations where it is a key component of smog over major cities (tropospheric ozone). The atmospheric layers defined by changes in temperature are shown in fig.1 (a), while the presence of ozone layer in the stratosphere is shown in fig. 1(b).

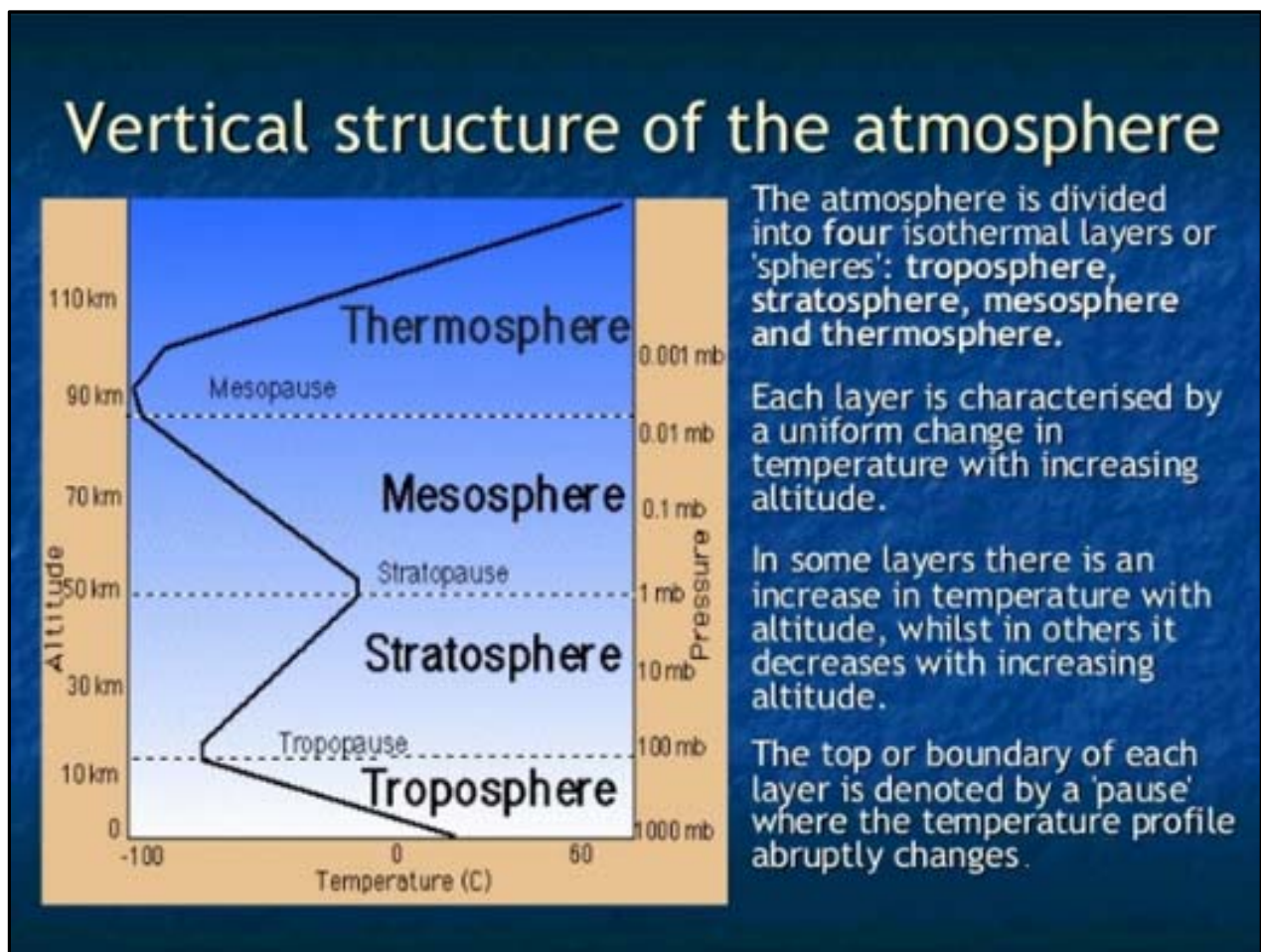


Fig.1 (a) shows the atmospheric layers defined by changes in temperature.

Courtesy: <http://slideplayer.com/slide/230655/>

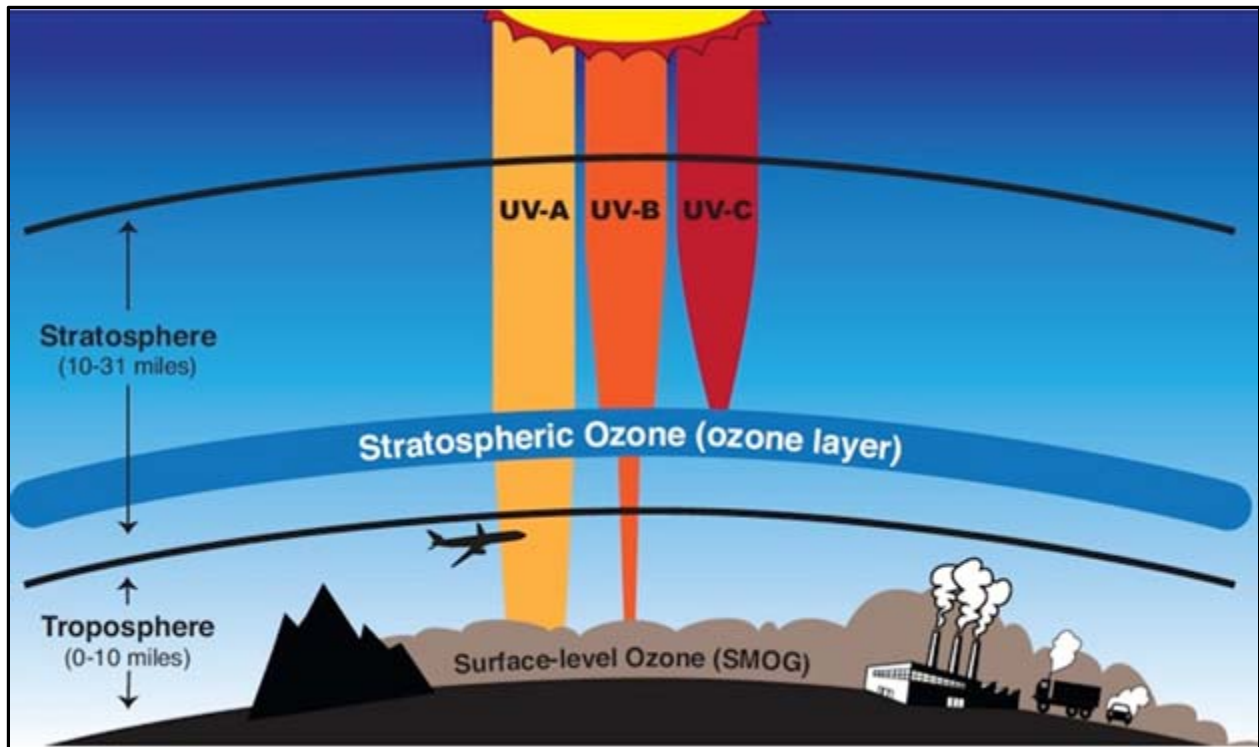
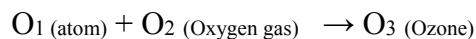
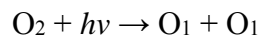


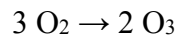
Fig.1 (b) The Ozone layer in the stratosphere.

Courtesy : <https://mynasadata.larc.nasa.gov/oyw/celebrate-world-ozone-day-with-nasa-september-16th-2014/>

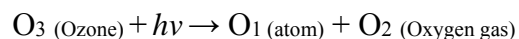
**Generation of Ozone in the Stratosphere:** Oxygen gas ( $O_2$ ) is present in the atmosphere. High energy or shorter wavelength UV light ( $h\nu$ ) collides with the oxygen molecule ( $O_2$ ), causing it to split into two oxygen atoms. These atoms are unstable, and they prefer being "bound" to something else. The free oxygen atoms then smash into other molecules of oxygen, forming ozone ( $O_3$ ).



The overall reaction between oxygen and ozone formation is:



The ozone is destroyed in the process that protects us from UV-B and UV-C rays emitted by the Sun. When ozone ( $O_3$ ) absorbs UV light ( $h\nu$ ), it will split the molecule into one free oxygen atom ( $O_1$ ) and one molecule of oxygen gas ( $O_2$ ). Thus, absorption of UV-B and UV-C leads to the destruction of ozone



Ozone is valuable to us because it absorbs harmful UV radiation during its destruction process (fig.2 (a)). A dynamic equilibrium is established in these reactions. The ozone concentration varies due to the amount of radiation of light received from the sun.

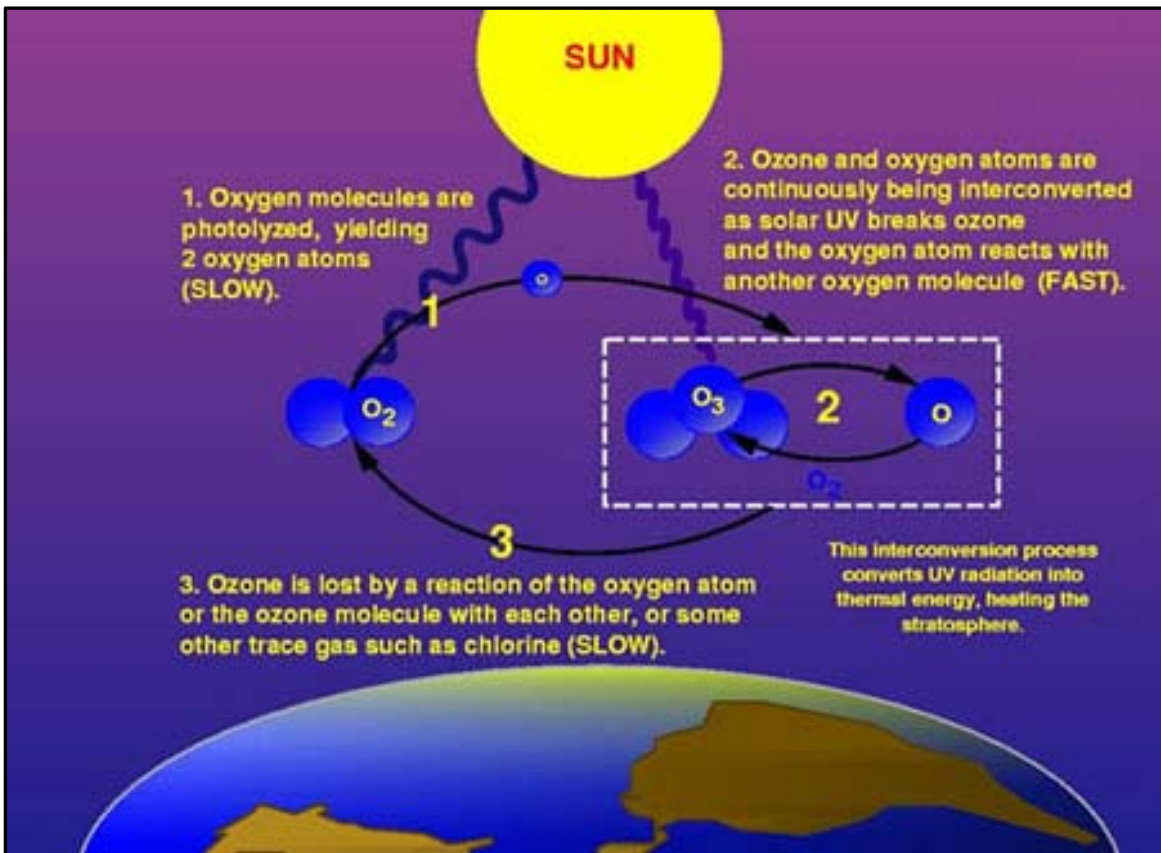


Fig. 2(a) Generation of ozone in the presence of UV light in stratosphere.

Courtesy: <https://www.summitlearning.org/guest/focusareas/562>

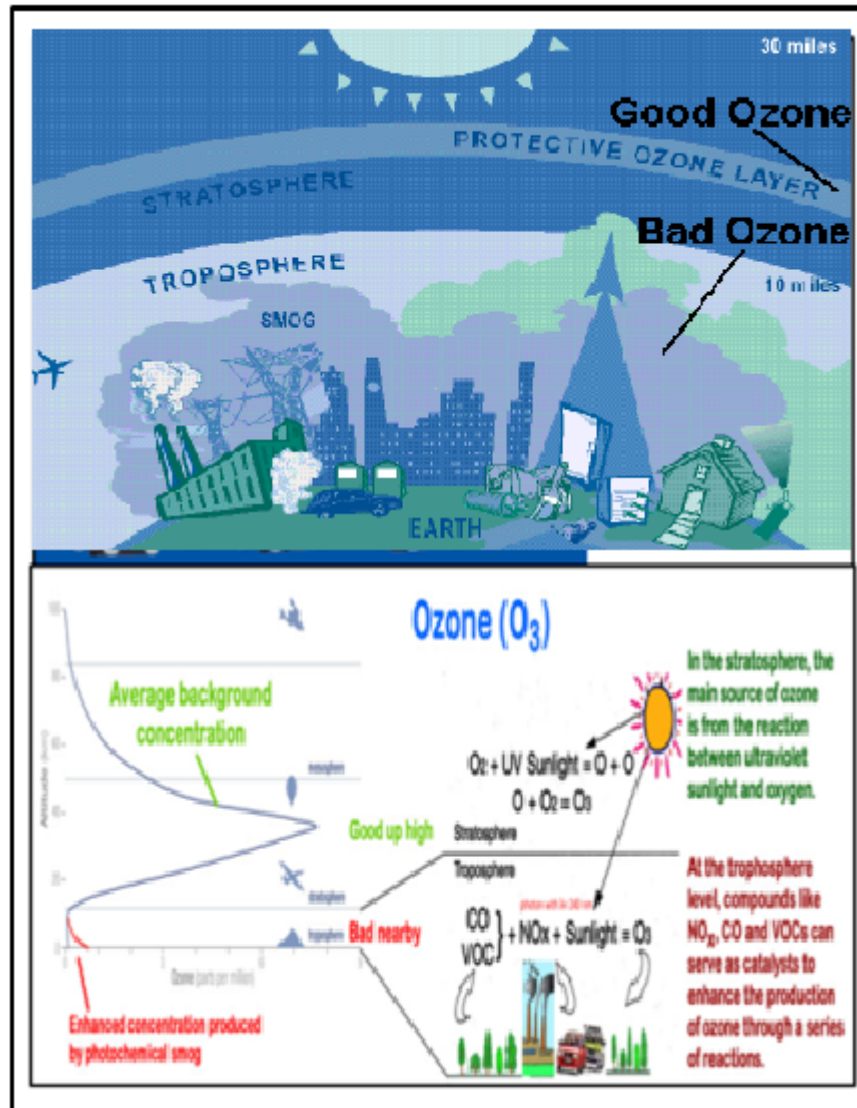


Fig. 2 (b) Good and bad ozone. Courtesy: [http://tecalive.mtu.edu/envengtext/ch12\\_criteria.htm](http://tecalive.mtu.edu/envengtext/ch12_criteria.htm)

**Generation of Ozone in the Troposphere:** Ozone in the troposphere is bad. It creates the respiratory problem, destroys polymers and reduces the plant growth. This ozone is contributing to the smog and greenhouse gases created by human activities, which is shown in fig.2 (b). Ozone close to the ground surface does not exist in high enough concentrations to shield us from UV light.

Pollutant gases, particularly, reactive halogen gases such as chlorine and bromine compounds in the atmosphere are responsible to cause the ozone depletion, which is mainly observed in the 'ozone hole' over Antarctica and over the North Pole. Most of the chlorine, and nearly half of the bromine in the stratosphere, where most of the depletion has been observed, comes from human activities. Fig. 2 (c) shows a schematic illustrating the life cycle of the chlorofluorocarbons (CFCs); how they are transported up into the upper stratosphere/lower mesosphere, how sunlight

breaks down the compounds and then how their breakdown products descend into the polar vortex.

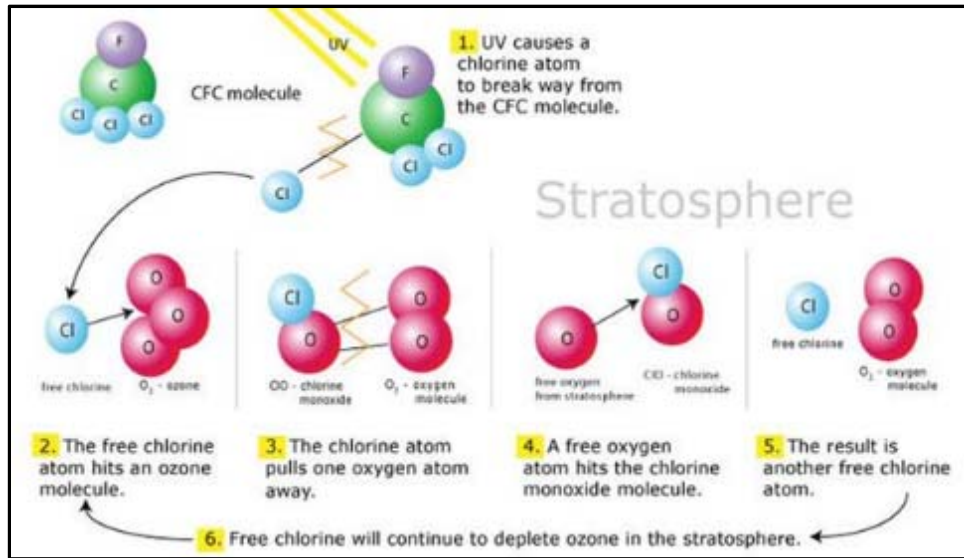


Fig. 2 (c) Chemical processes of ozone depletion and CFCs.

Courtesy: <https://environmental-chemistry.wikispaces.com/Ozone+Depletion>.

Fig. 2(d) show the typical data plots of polar ozone depletion.

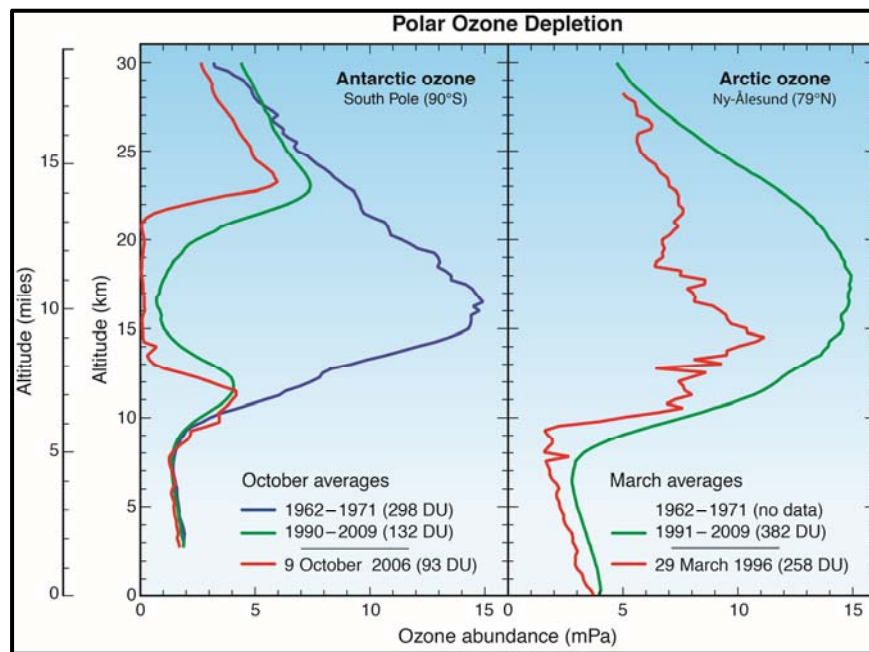


Fig. 2 (d) Depletion of polar ozone.

Courtesy: <http://www.esrl.noaa.gov/csd/assessments/ozone/2010/twentyquestions/>

Looking into this global issue of ozone depletion, we are working on the development of ozone sensors and low weight sensors payload to measure the ozone profile in the stratosphere on the real time mode using the HASP balloon flight since 2008. HASP-NASA provided a platform for 12 small payloads and 4 large payloads. The maximum mass limit was 20 kg for a large payload and 3 kg for a small payload. UND and UNF jointly had one small payload to measure the ozone profile in the stratosphere. UNF team fabricated the gas sensors system, payload body, microcontroller circuit, software, and electronic communication circuits. The HASP had an onboard computer, power supply batteries, GPS, video camera, and communication link for all payloads. UNF team was participated the workshop at the NASA-Columbia Scientific Balloon Facility (CSBF) in Palestine, Texas during July 31 to August 5, 2016 for the integration of the sensors payload with the HASP. Ozone sensor payload was then integrated with the HASP platform. The UND-UNF payload successfully passed all required thermal vacuum tests and certified for the flight. Then, the HASP2016 flight was launched successfully by NASA-CSBF on September 1, 2016 from Fort Sumner, New Mexico. The flight was terminated on September 2, 2016 near Grand View, AZ. The total flight duration was about 18 hours and 19 minutes. During the flight, the UNF ozone sensors array detected and measured ozone in the stratosphere. The payload sent out the data files during the flight without any problem. After the termination of the balloon flight, the payload landed safely on the ground using a parachute. Then, the payload was recovered. The technical details, pictures and science results of this flight are highlighted in this report.

## 2. Fabrication of Nanocrystalline Thin Film Gas Sensors

Ozone sensors were fabricated by UNF team at Dr. Patel's Sensors Laboratory at the UNF. Fig.3 (a) and (b) shows thermal vacuum deposition system and electron beam deposition system, respectively, were used to fabricate nanocrystalline nanocomposite thin film gas sensors for the detection of ozone gas.



Fig. 3 (a) Thermal vacuum deposition system and (b) electron beam deposition system.



Fig. 4(a) shows the top view of one typical low magnification scanning electron microscope image of the Indium Tin Oxide (ITO) thin film gas sensor having two gold electrodes for external electrical contacts. Fig. 4 (b) shows a typical array of 8 ITO thin film gas sensors fabricated on an approximately 2.5cm x 2.5cm ultra cleaned glass slide. The glass slides were throughlly cleaned by the ultrasonic cleaner, detergent, solvent and baked in the ovan. The interface of the cicuit board to the array is also shown in fig. 4(b).

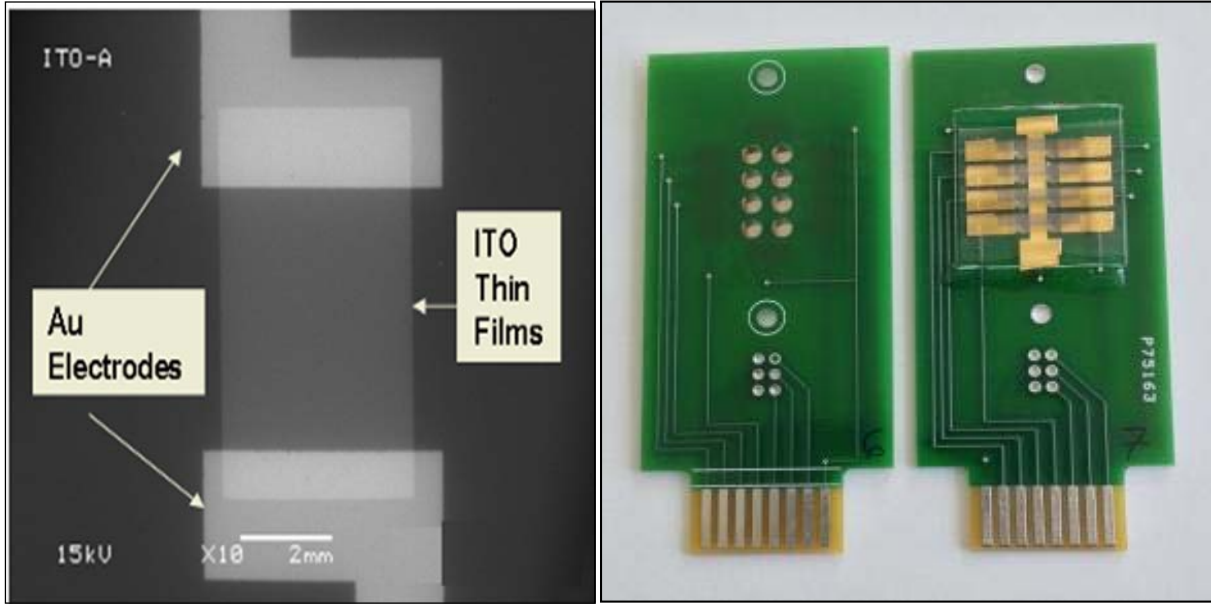


Fig.4 (a) Scanning electron microscope image of top view of one ITO thin film gas sensor (Size: 2 x2 mm), (b) Top and bottom view of 8 gas sensor array interface with the printed circuit board (Size: 4 x 7 cm) (UNF Patent pending).

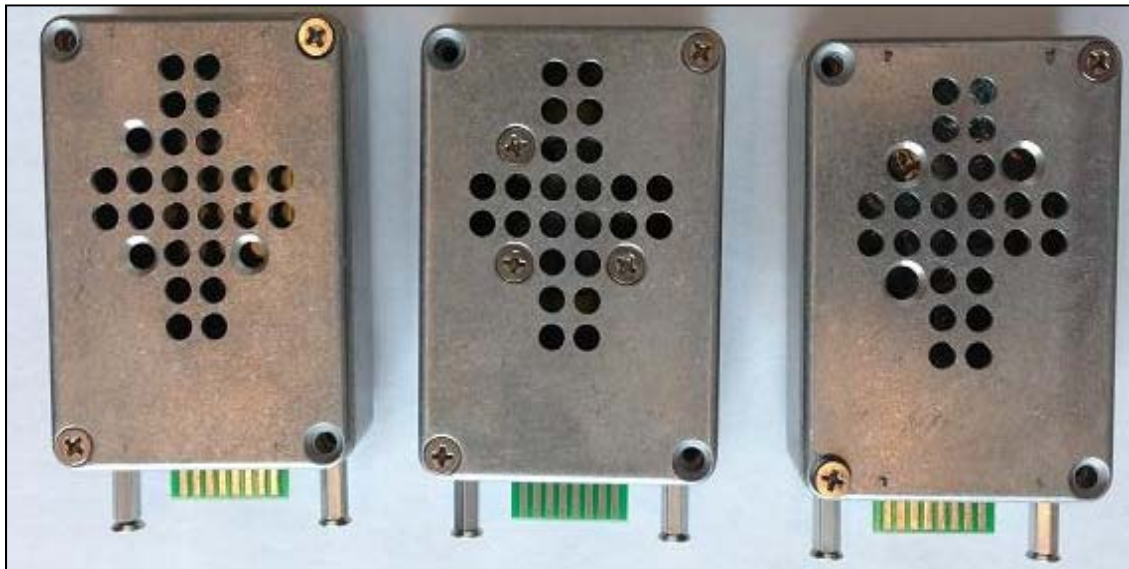


Fig. 4(c) Sensors boxes # 1, 2 and 3. Size of box: 5.5 x 2.5 x 8.0 cm.

Three types of sensor array boxes were fabricated as shown in Fig. 4(c). Each type of sensor array was mounted in a separate box. In addition to the sensors box for the payload, three backup sensors PCB boxes were fabricated. All sensors boxes were calibrated by UNF students' team at different time period and then tested in the thermal vacuum test chamber at CSBF, Palestine, TX.

**We fabricated several new sensors at different growth conditions every year in order to improve the performance and optimization of fabrication parameters such as thickness of film, substrate temperature, deposition rate and doping concentration, etc.**

**Box #1** sensors are nanocrystalline ITO thin film deposited on glass for detection of ozone.

**Box #2** sensors are ZnO + ITO thin films deposited on glass for detection of ozone.

**Box #3** sensors are nanocomposite of ITO +SnO<sub>2</sub> thin films deposited on glass for detection of Ozone and smog in the Atmosphere / Troposphere,

**Backup Box # 4, 5 and 6, Backup PCB # 7, 8 and 9.**

Fig. 5 (a) shows the picture of housing for the UNF sensors, consisting of an array of 8 gas sensors interfaced with a printed circuit board (PCB), flexible Kapton heater (MINCO make HK 5573R30.0 L12BU), temperature sensor ( Analog Device TMP36), electrical fan (SUNON, MC25060V2-0000-A99, DC 5V, 0.38W) and a 16 wires flat cable. One end of flat cable has a female card edge connector to connect sensor PCB (Make: 3M, MCS16K-ND), while other end has 16 pin female to connect microcontroller PCB.

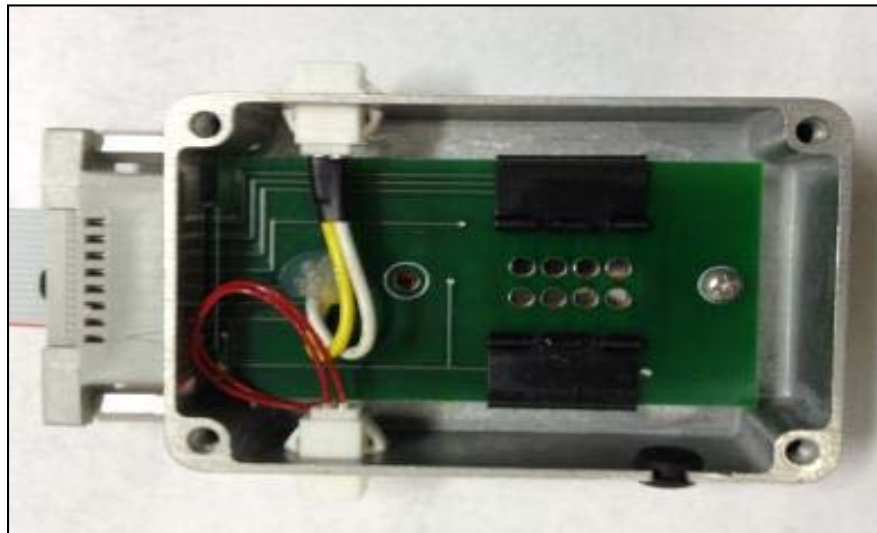


Fig.5 (a) Inner view of UNF Ozone sensors box.

The pin information of sensor PCB and connector are shown in fig. 5(b) and (c), respectively.

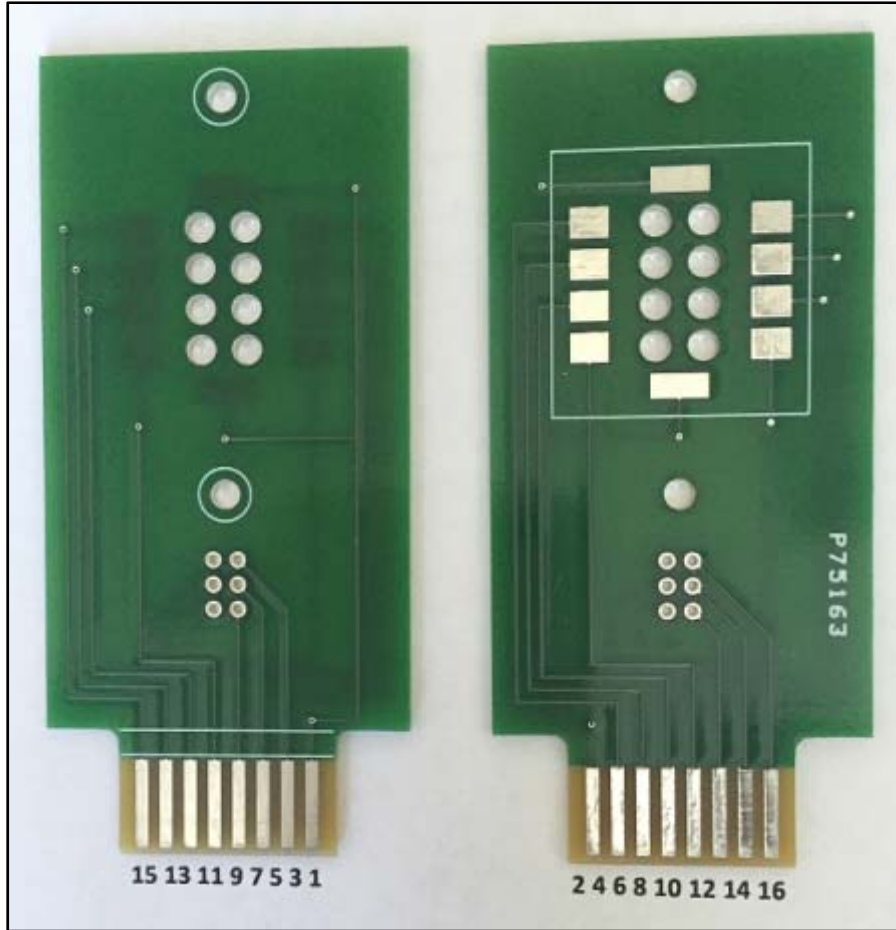


Fig.5 (b) Pin numbers of sensor PCB.

Pin number per connector datasheet							
1	3	5	7	9	11	13	15
Common	Temp Sensor	Temp Sensor	Temp Sensor	Gas Sensor	Gas Sensor	Gas Sensor	Gas Sensor
Open	Gas Sensor	Gas Sensor	Gas Sensor	Gas Sensor	Light Sensor	Light Sensor	Pin not used
2	4	6	8	10	12	14	16
Pin number per connector datasheet							

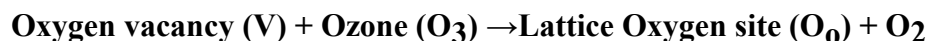
Fig.5 (c) Pin information for connection of 16 pins female card edge connector with sensor PCB.

### 3. Working Principles of Gas Sensors

#### **Interaction of oxidizing gas on surface of n-type ITO thin film sensor**

Upon adsorption of charge accepting molecules at the vacancy sites, namely from oxidizing gases such as ozone (O<sub>3</sub>), these electrons are effectively depleted from the conduction band of ITO. This leads to an increase in the electrical resistance of n-type ITO.

*For ozone gas:*

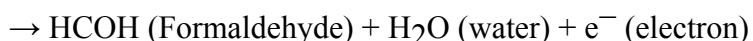
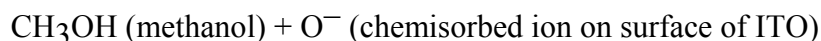


Vacancies can be filled by the reaction with ozone. Filled vacancies are effectively electron traps and as a consequence the resistance of the sensor increases upon reaction with ozone.

#### **Interaction of reducing gas on surface of n-type ITO thin film sensor**

Oxygen vacancies on ITO surfaces are electrically and chemically active. These vacancies function as n-type donors decreasing the electrical resistivity of ITO. Reducing gases such as CO, H<sub>2</sub> and alcohol vapors result in detectable decreases in the electrical resistance of n-type ITO.

*For reducing gas, e.g. methanol:*



Vapors come in contact with the surface and react with chemisorbed oxygen ions O<sup>-</sup> or O<sup>2-</sup> and re-inject electrons into the conduction band.

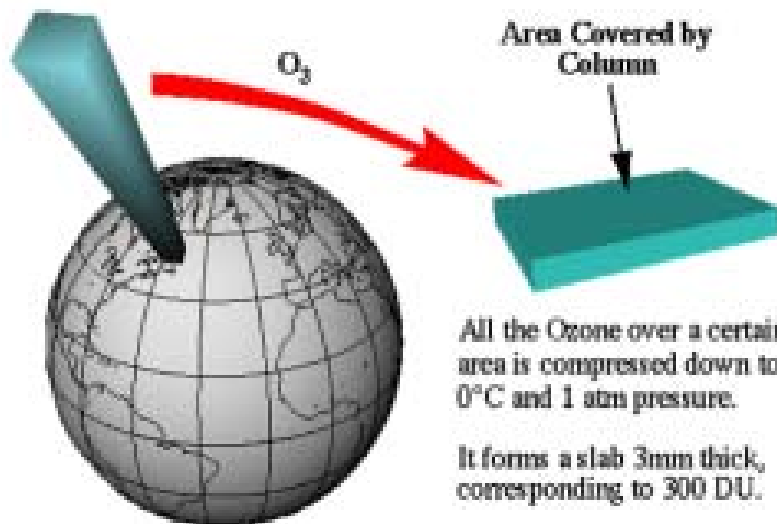
In summary, the electrical resistance of ITO increases in the presence of oxidizing gases such as ozone. Upon adsorption of the charge accepting molecules at the vacancy sites, namely oxidizing gases such as ozone, electrons are effectively depleted from the conduction band, leading to an increase in the electrical resistance of n-type ITO. Note that our three different types of sensors boxes have n-type semiconductor gas sensors.

## Units for measurement of ozone

In the presence study, we used part per million (ppm) units for determination of ozone concentration. We calibrated our sensors in the closed chamber using a digital ozone meter, which has unit in ppm only.

Ozone is also measured by the Dobson spectrometer in Dobson Units (DU). Our sensors are very cheap, smaller in size, low mass and easy to interface with electronic compared to that of Dobson spectrometer.

1 Dobson Unit (DU) is defined to be 0.01 mm thickness of gas at STP (0°C, 1 atm); the ozone layer represented above is then ~300 DU



Global Average Ozone: 300 DU=3 mm



Ozone Hole Average: 100 DU=1 mm



## 4. Calibration of Gas Sensors

The ITO sensors array was first tested and calibrated in the test chamber at UNF. The test chamber was adjusted to the identical conditions of temperature and pressure as in the stratosphere. Fig. 6(a) and (b) shows the pictures of ozone generator and detector used for the calibration of sensors. An ozone generator (Ozone Solutions, Model# OMZ-3400) was used as the source of ozone, which generated 0 to 12 ppm ozone gas.

A digital ozone detector (Eco Sensors, Inc., Model:A-21ZX) was used to measure the concentration of ozone in part per million (ppm). The Keithley digital multimeters and electrometers attached with computer having LabView program were used for the measurements of the ITO sensor's resistance.



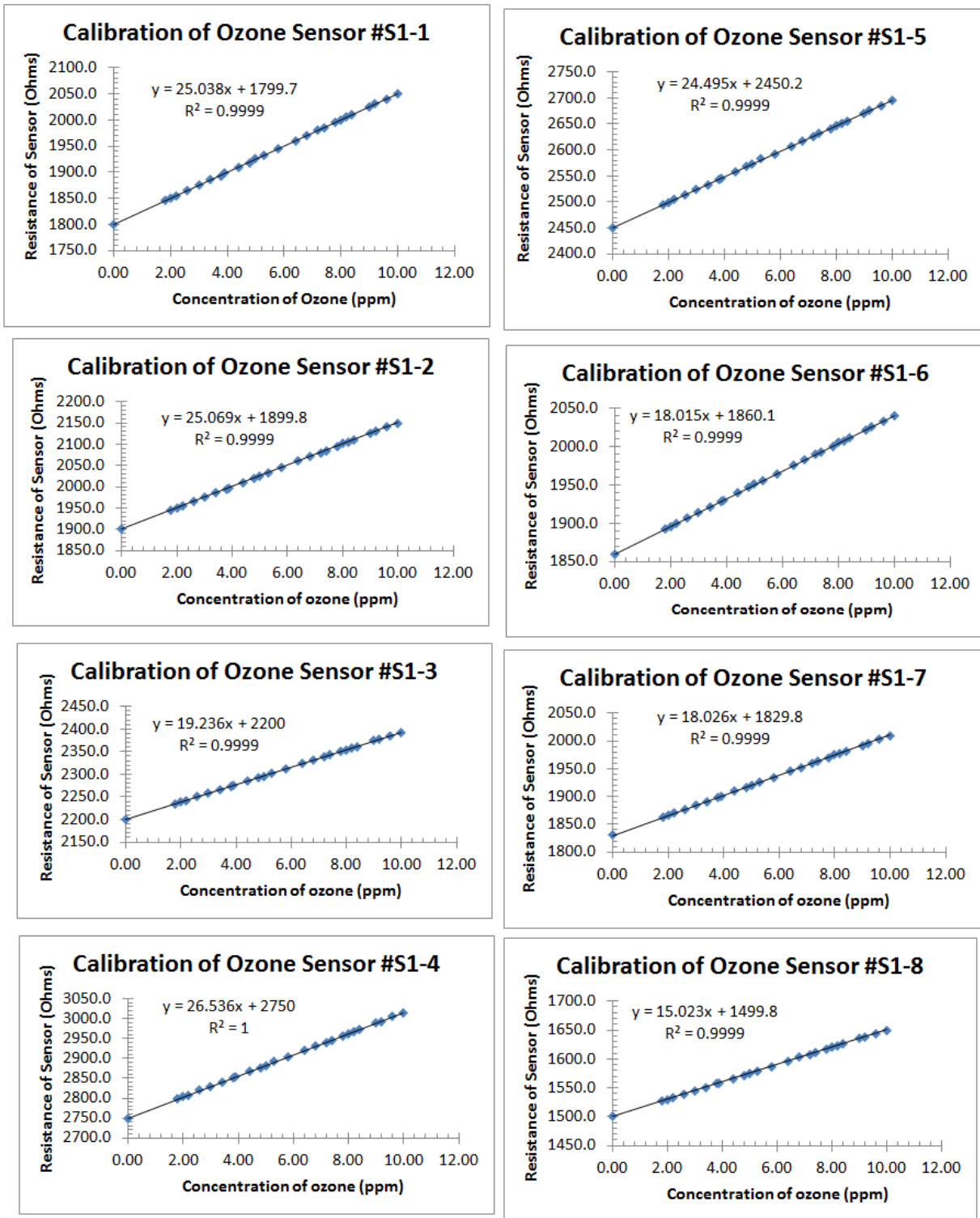
Fig.6(a) Ozone generator and (b) digital ozone detector.

All the 24 sensors of sensors box was calibrated simultaneously under identical conditions of pressure, temperature and concentration of ozone in the test chamber. The sensors were calibrated with ozone gas in the range of 0.02 to about 10.00 ppm in the test chamber in the same run. The usual variation of ozone in the stratosphere is about 3.0 to 10.0 ppm. The measured data fit linearly and trend line equations for each plot were determined.

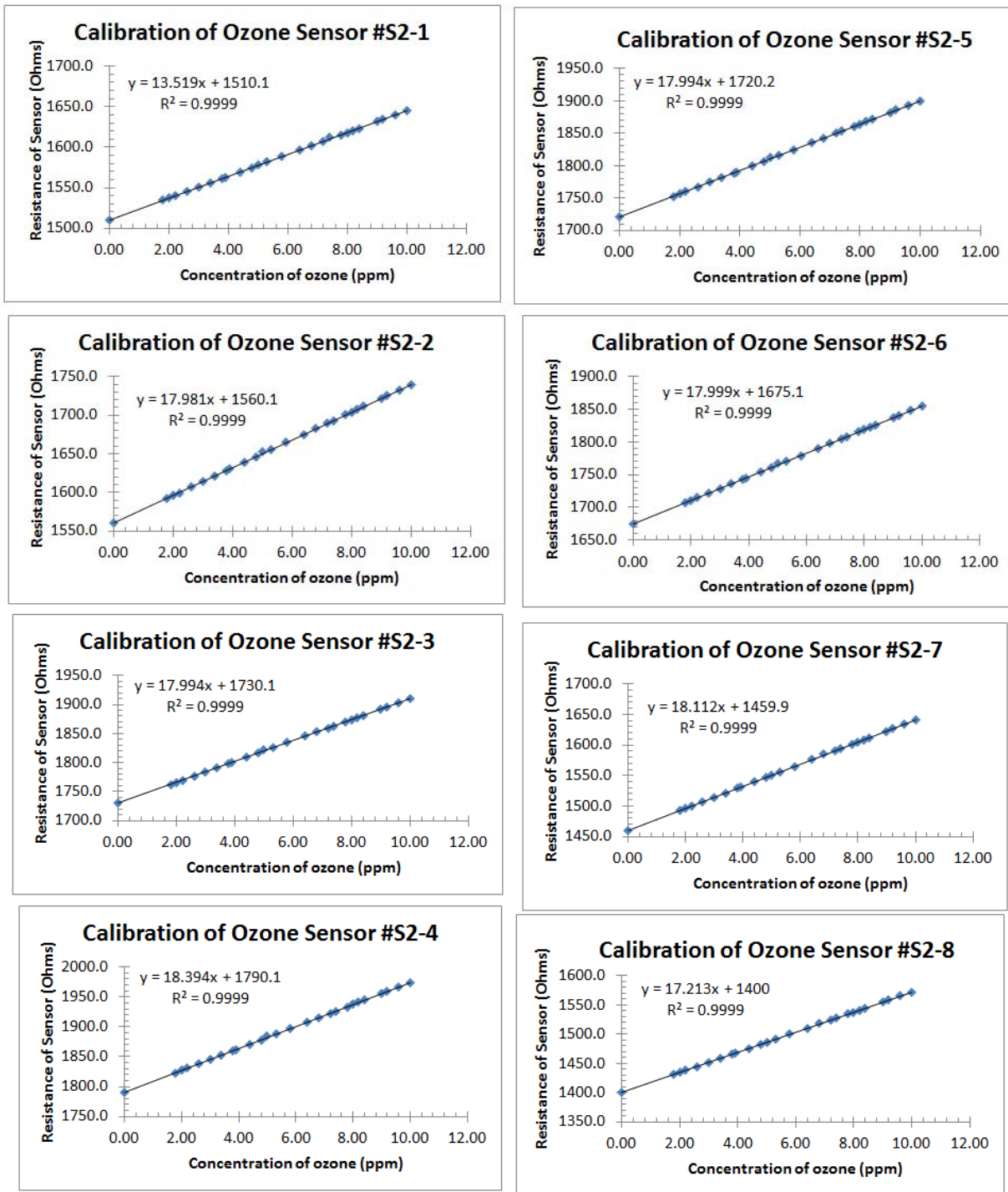
Figs.7 (a) show the calibration plots ozone sensors Box#1 having sensors # S1-1 to S1-8. These sensors were made of nanocrystalline ITO thin film gas sensors fabricated on the glass.

Figs.7 (b) show the calibration plots ozone sensors Box#2 having sensors # S2-1 to S2-8. These sensors were made of nanocomposite of ZnO + ITO thin film and were fabricated on the glass.

Figs.7 (c) show the calibration plots ozone sensors Box#3 having sensors # S3-1 to S3-8. These sensors were made of nanocomposite of ITO +SnO<sub>2</sub> thin film and were fabricated on the glass.

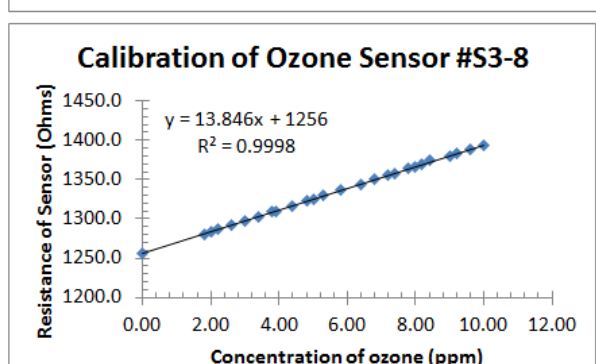
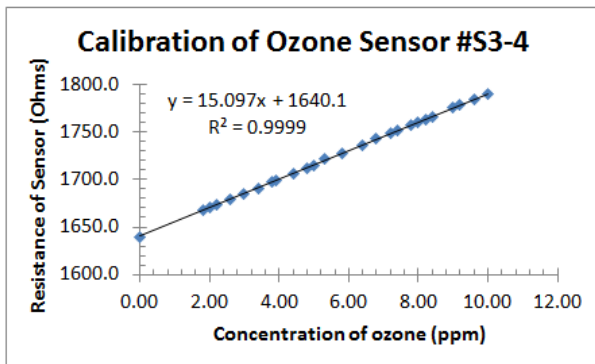
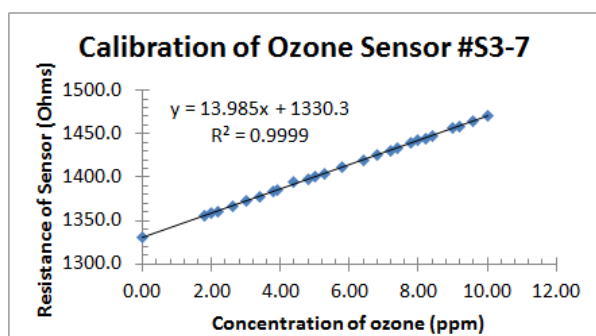
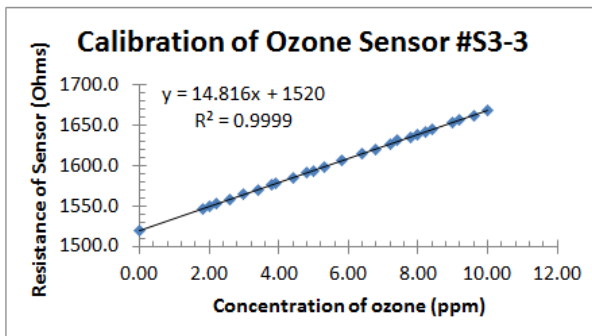
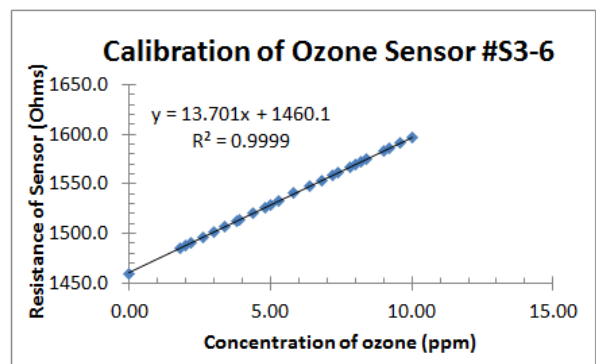
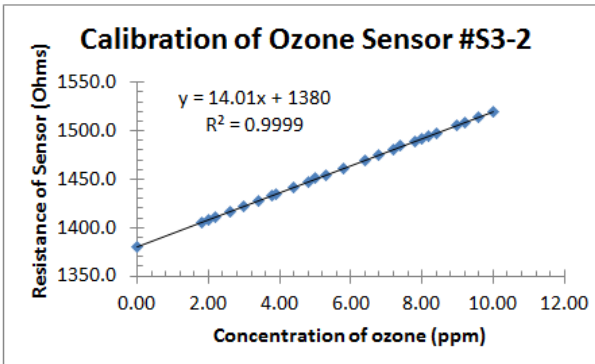
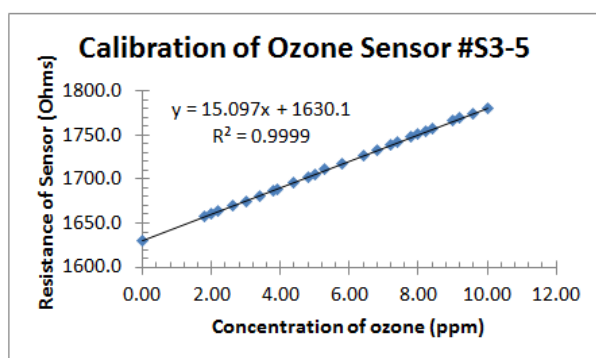
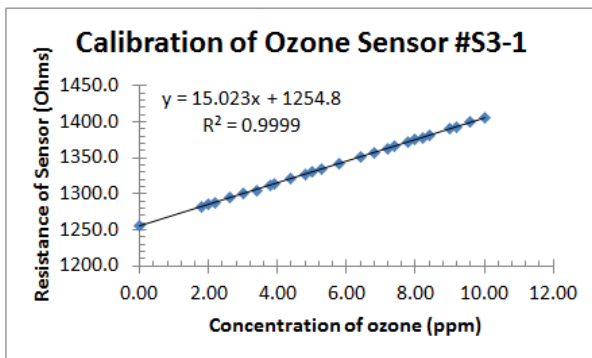


Figs.7 (a) show the calibration plots ozone sensors Box#1 having ITO thin film gas sensors # S1-1 to S1-8.



Figs.7 (b) show the calibration plots ozone sensors Box#2 having ZnO+ITO thin film gas sensors # S2-1 to S2-8.





Figs.7 (c) show the calibration plots ozone sensors Box# 3 having ITO+SnO<sub>2</sub> thin film gas sensors # S3-1 to S3-8.

All sensors were calibrated at three different times and showed nearly the same nature of response each time. Small variations in the slope and y-intercept values were observed due to the variation of sensor thickness and experimental error.

## 5. Fabrication of Payload Body

The height of 2016 payload was reduced to about 228.6 mm ( $\approx$  about 9 inches) from 304.8 mm ( $\approx$  about 12 inches) height of the 2014 payload. Because of reduce in the height; the payload greatly reduced the mass. The 2016 payload retained it's easy to open and close design utilizing the top plate for access to the PCB as well as all sensor boxes. The payload continues to feature a rectangular design due to its robustness as well as for its low rate of outgassing under extreme pressure drops. This design is optimal for the team's goal of a reusable payload body. The details of design and drawing are shown in fig. 8 (a) to (o). Joe Silas made design and drawings of the payload body using AutoCAD. UNF students did fabrication work of the payload boy in the UNF workshop.

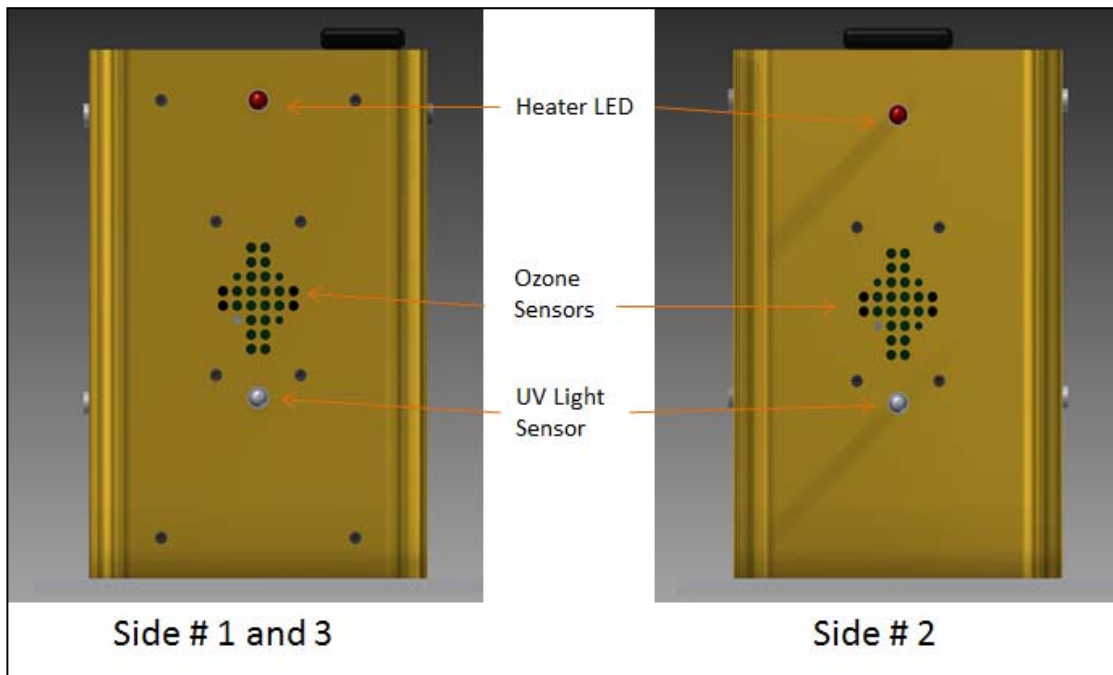


Fig. 8 (a) Side view design of the payload

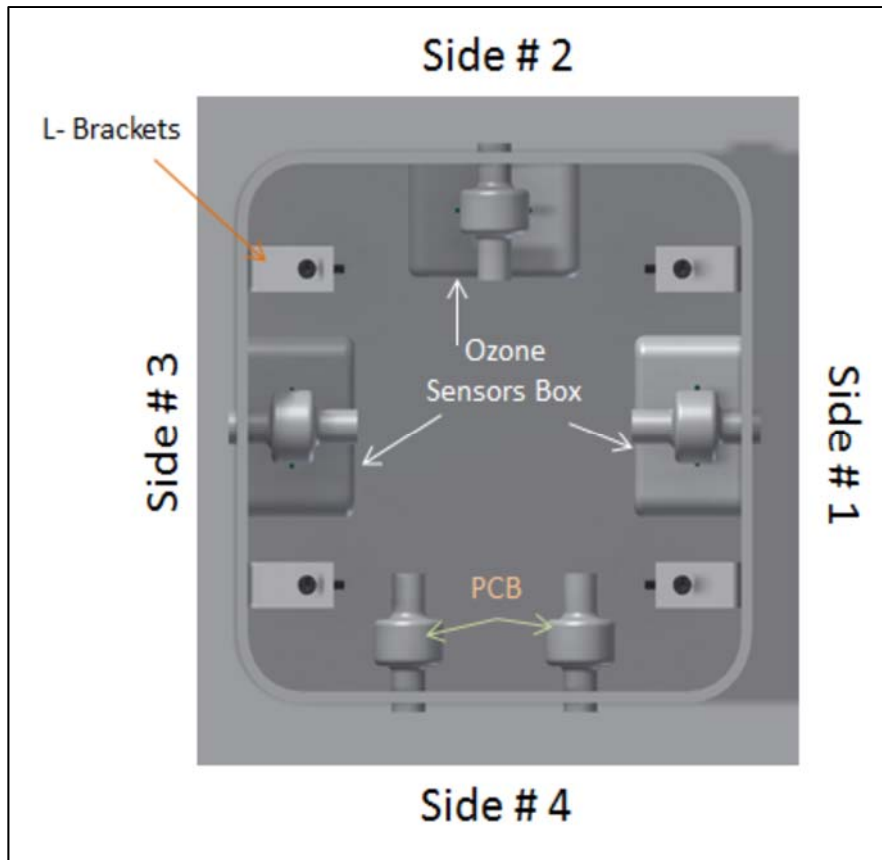


Fig. 8 (b) Top view design of the payload

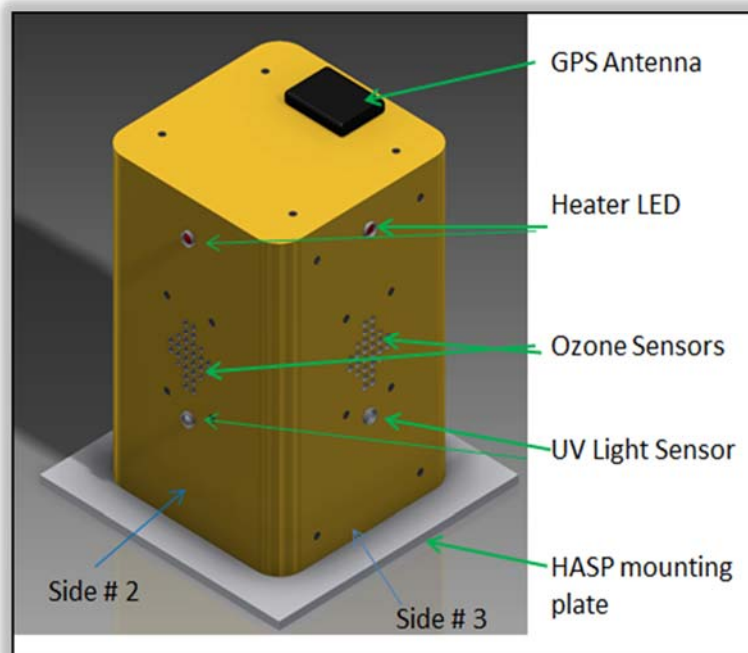


Fig.8 (c) Design of payload body.

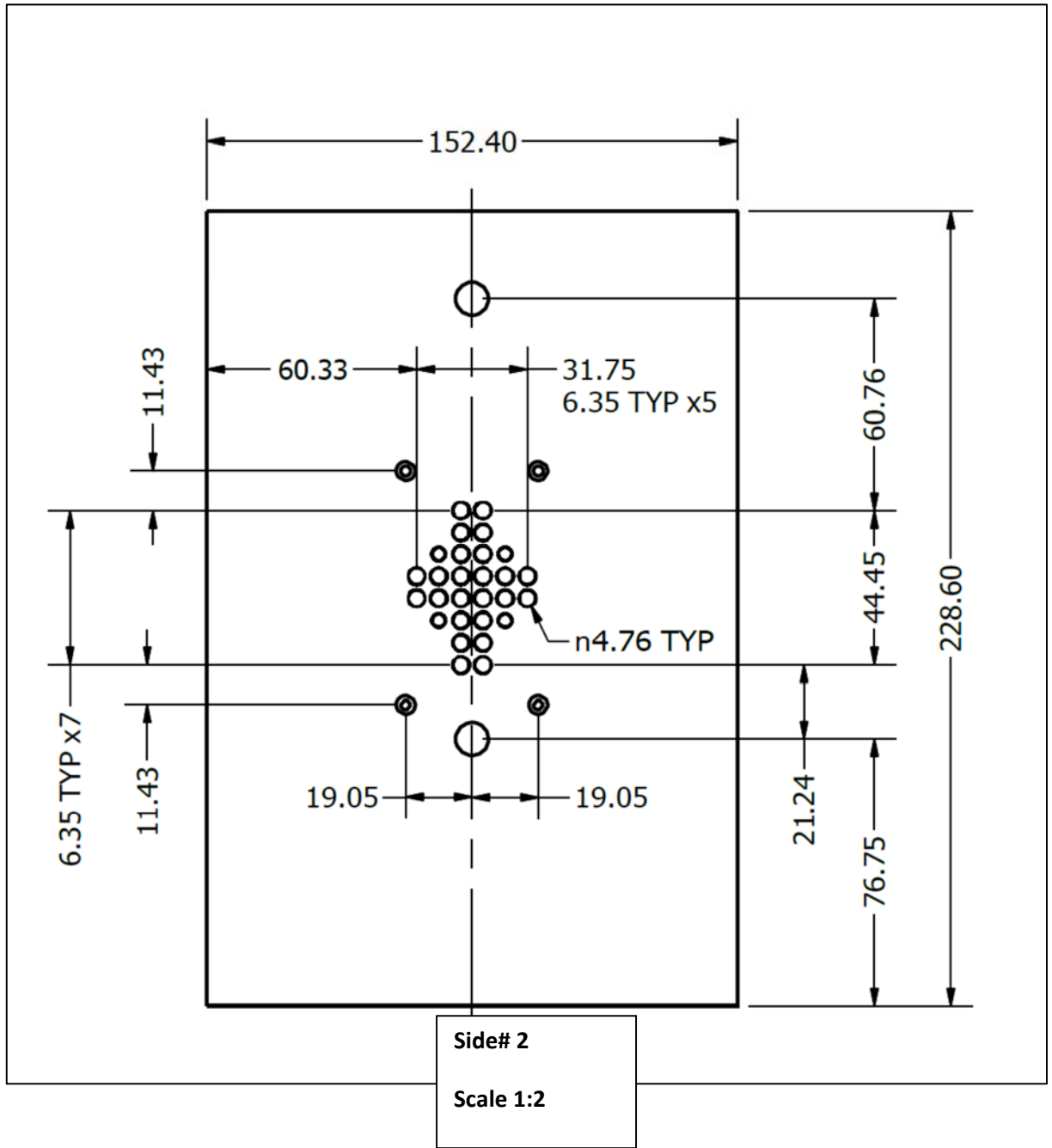


Fig. 8 (d) Design of side # 2 of the payload. All dimensions are in mm.

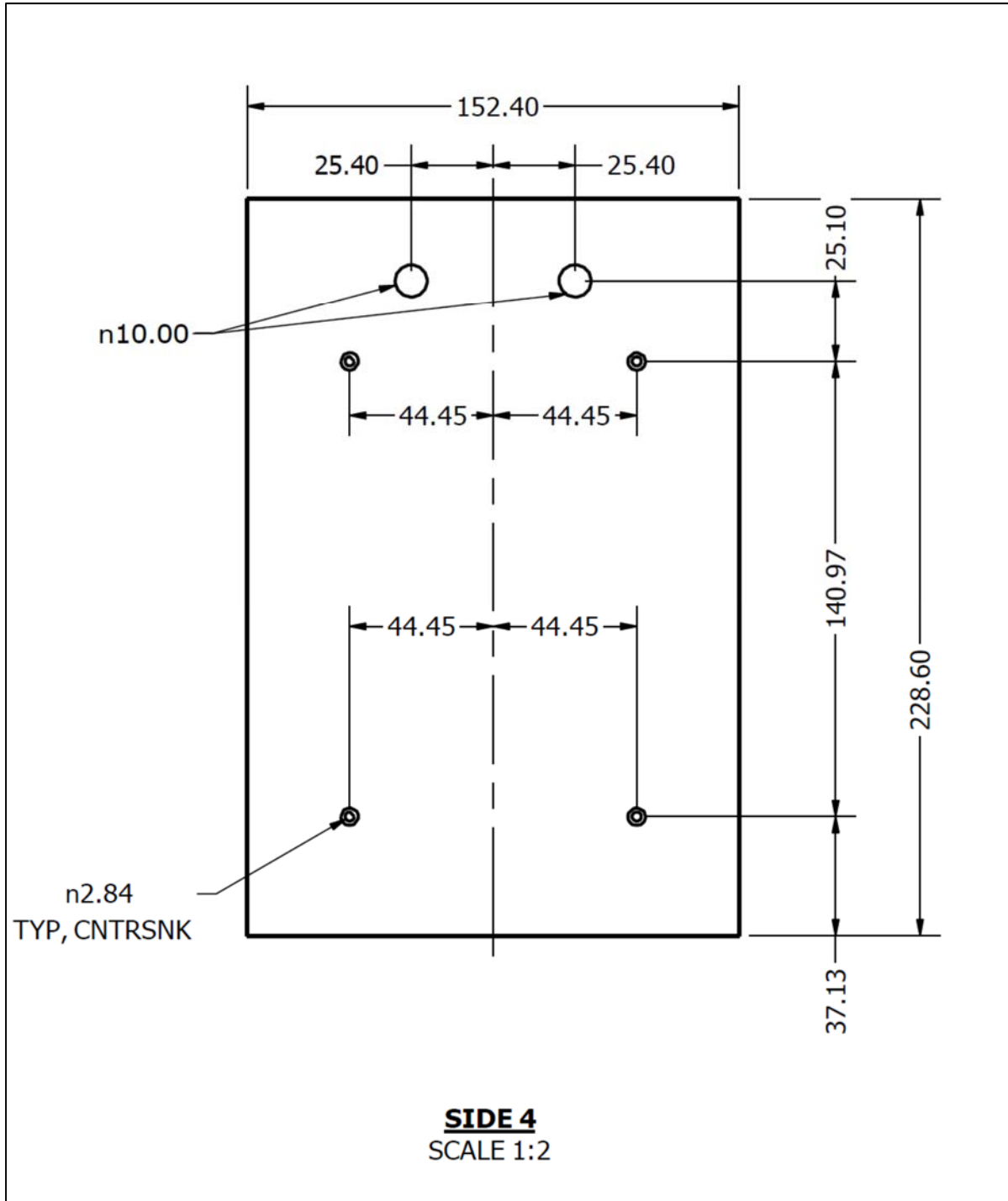


Fig. 8(e) Design of side # 4 of the payload  
All dimensions are in mm.

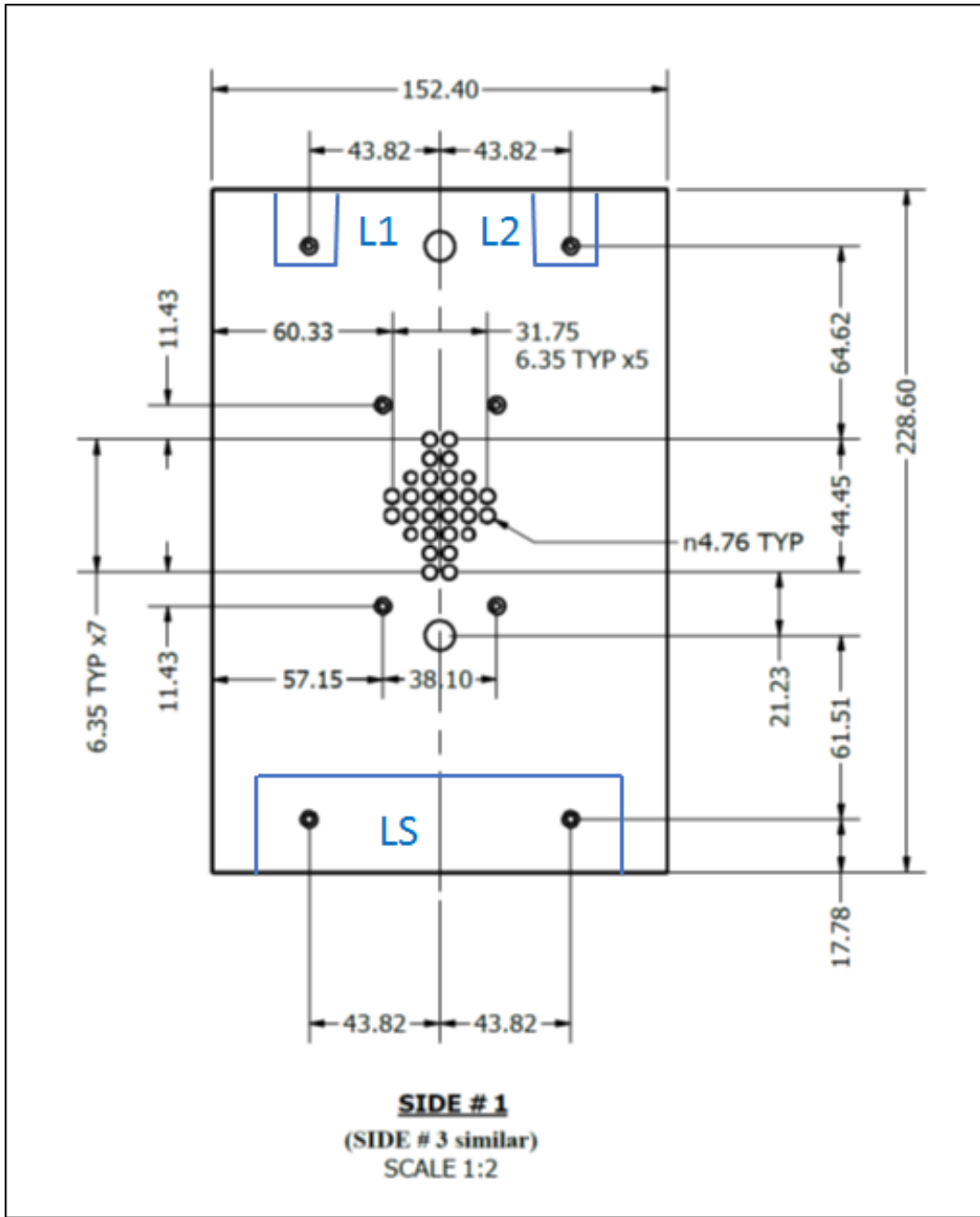


Fig. 8(f) Design of sides # 1 and 3 of the payload.  
All dimensions are in mm.

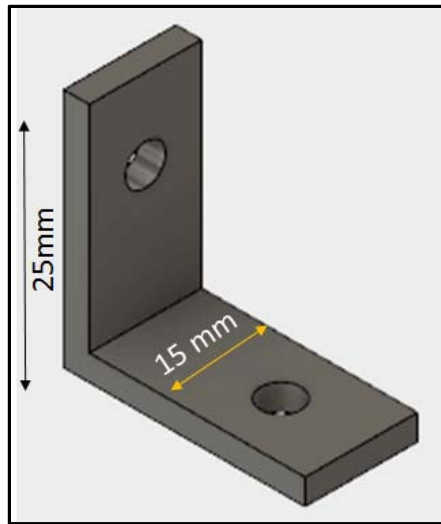


Fig. 8 (g) Schematic diagram of L- Bracket.  
**L1** and **L2** are L-Brackets for mounting the top lid on the payload body

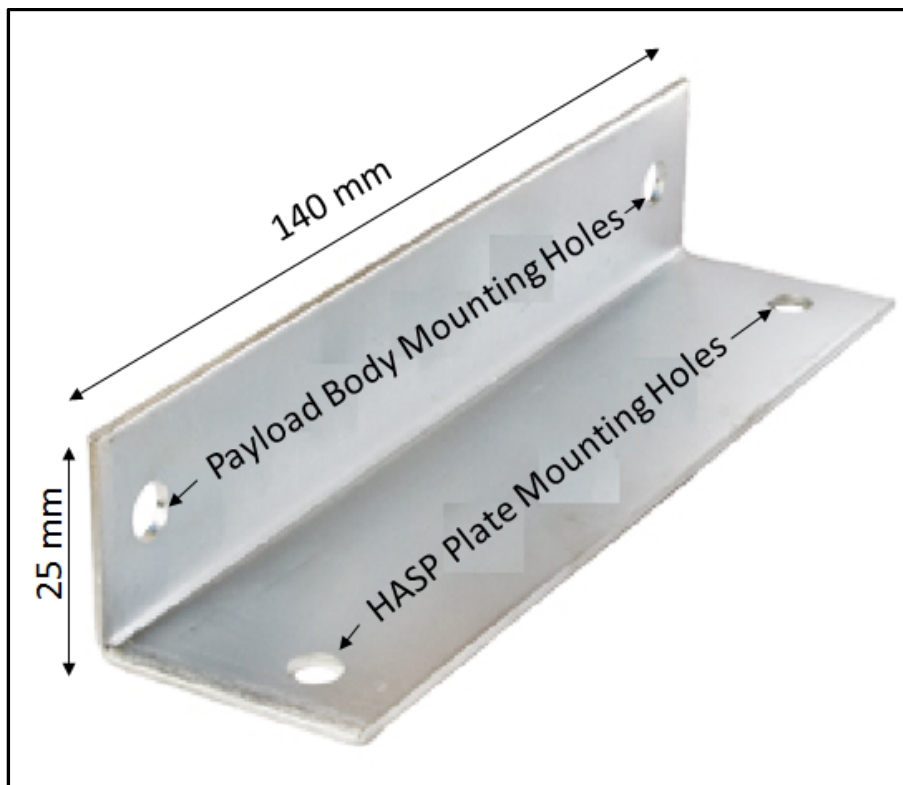


Fig. 8 (h) Schematic diagram of L-Strip (**LS**) for mounting the HASP plate with payload body

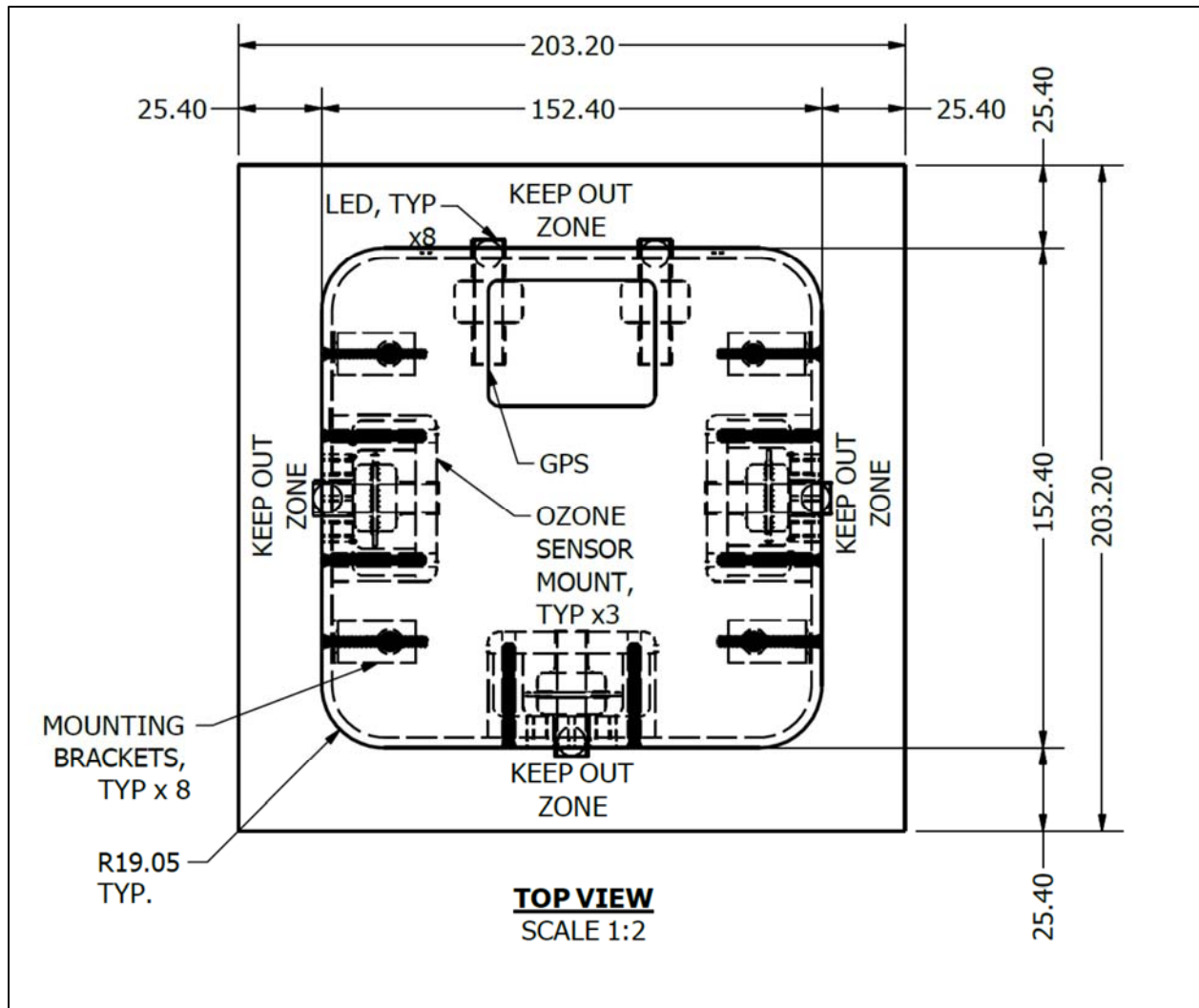


Fig. 8 (i) Design of top view of the payload. All dimensions are in mm.



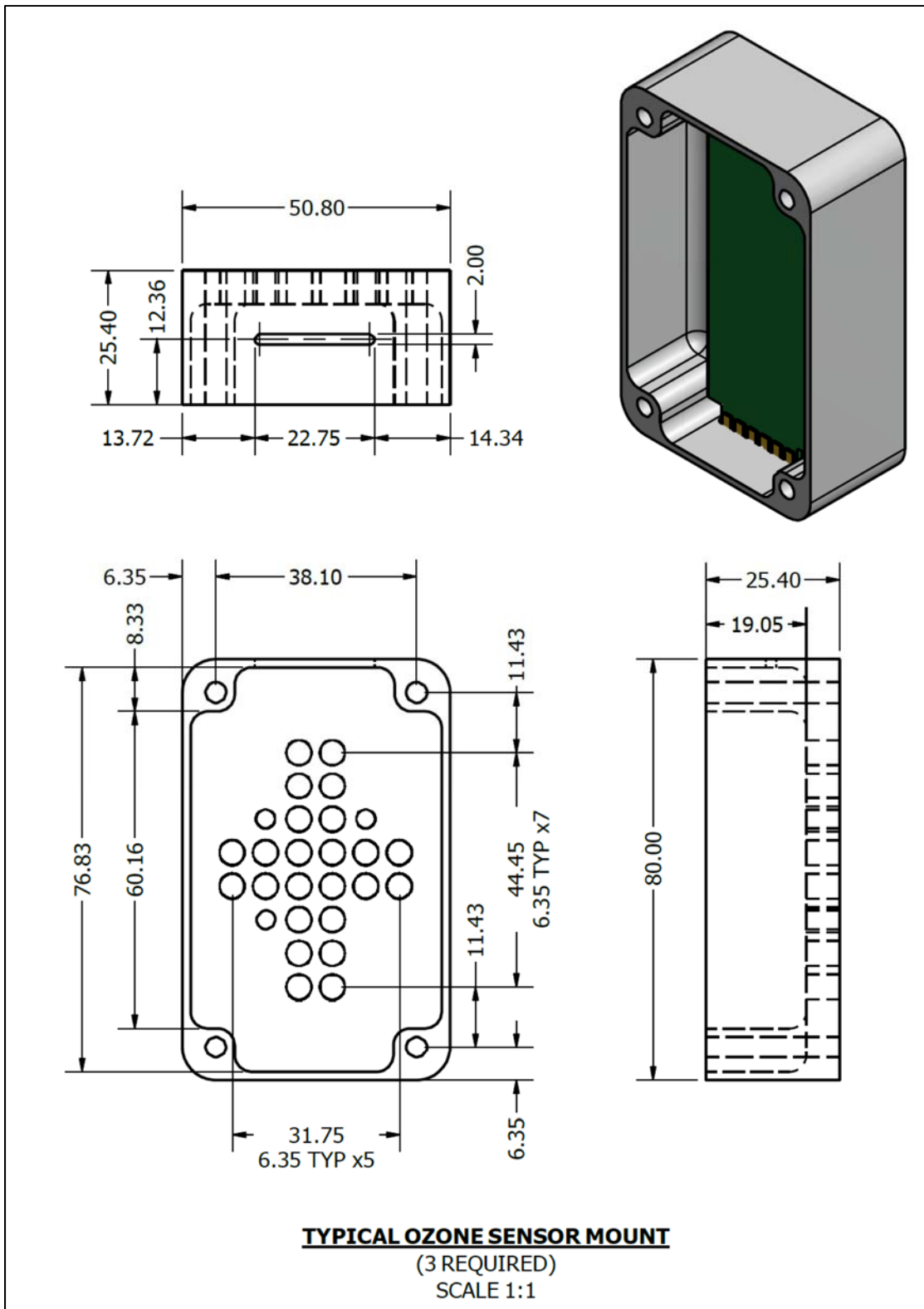


Fig. 8 (j) Design of top view of the payload. All dimensions are in mm.

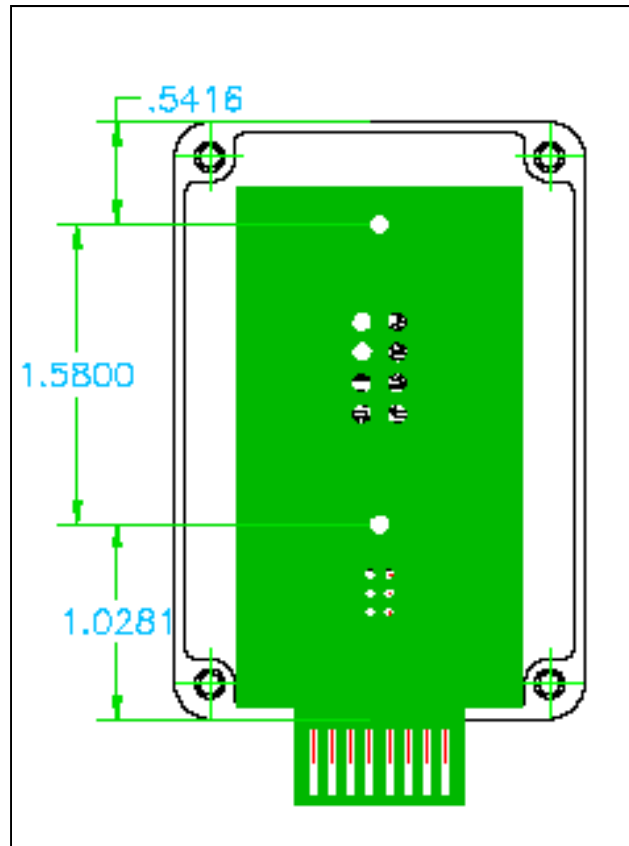


Fig.8 (k) Design for standoff to mount sensor PCB in the box

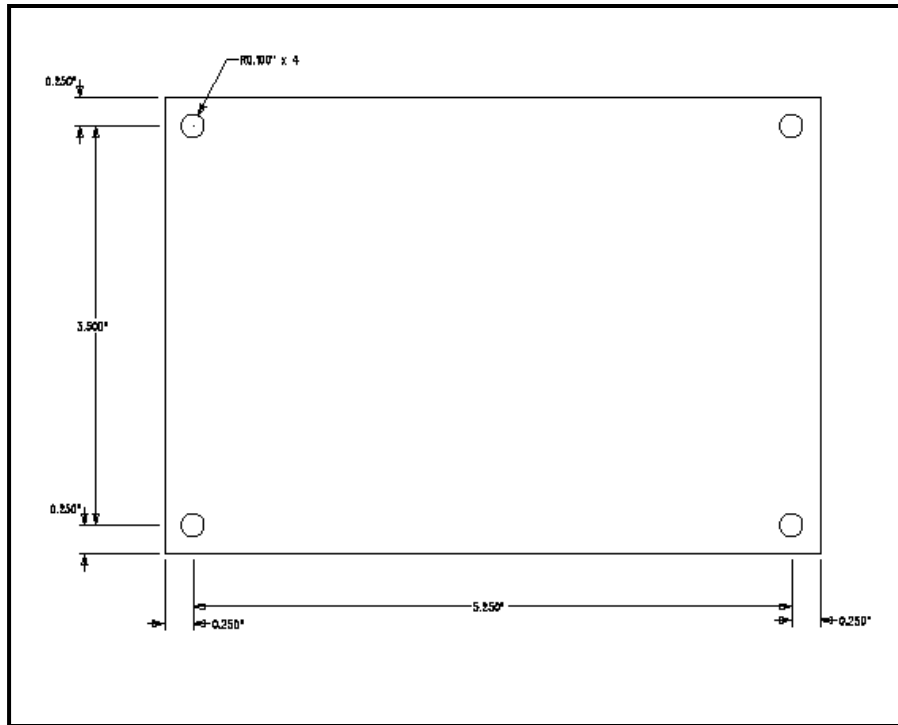


Fig. 8 (l) Design for hole of the microcontroller PCB



Fig.8 (m) Fabrication of payload body by Chris (UNF).



Fig.8 (n) Chris operated the high vacuum systems for the fabrication of thin film gas sensors.



Fig. 8 (o) Testing of software of the payload by Ken, Jesse and Chris.

Table-1 shows the parts were procured for the payload body from supplier [www.onlinemetals.com](http://www.onlinemetals.com).

Table-1 Metal parts for the payload body

<b>Name</b>	<b>Size</b>	<b>Purpose</b>
Aluminum Extruded Square Tube Part #6063-T52	height 9" w x d: 6" x 6" wall thickness: 0.125"	Payload body
Aluminum Sheet Part#3003-H14	6" X 6" Thickness: 1/8"	Top lid

Table-2 shows weight budget of various parts of the payload. The estimated total mass of payload including its base plate was 2.72 kg, which was less than the limit of 3.00 kg + 0.50 kg mass of base plate (total 3.5 kg)

Table-2. The estimated weight budget of the payload

<b>Item:</b>	<b>Dimension</b>	<b>Mass (g)</b>
8 Ozone sensors box #1 (including fan, heater, box)	3 x 2 x 1 inch	200.0±2.0
8 Ozone sensors box #2 (including fan, heater, box)	3 x 2 x 1 inch	200.0±2.0
8 Ozone sensors box#3 (including fan, heater, box)	3 x 2 x 1 inch	200.0±2.0
Microcontroller PCB with mounted components	4 x 6 inch	300.0±1.0
Payload body, top plate and thermal blanket	9 x 6 x 6 inch	1100±10.0 g
Few Cables, 1 GPS, 2 LEDs, 3 Photodiodes, nuts and bolts		160±5.0 g
HASP mounting plate	7.9 x 7.9 inch	560±3.0 g
<b>Total estimated mass of the payload and HASP plate</b>		<b>2720±25.0 g</b>

The outer surface of payload body was covered by the thermal blanket made of silver color aluminized heat barrier having adhesive backed (Part No. 1828) (Make: [www.PegasusAutoRacing.com](http://www.PegasusAutoRacing.com)) for the improvement of thermal stability. The high reflective surface of the material is capable of withstanding radiant temperatures in excess of 1000°C. Fig. 9 shows the typical plots of % reflectance at different wavelength of light from the silver, gold, copper and aluminum surfaces. Silver color surface higher reflectance over wide range of wavelength of light compare to gold, copper and aluminum surfaces..

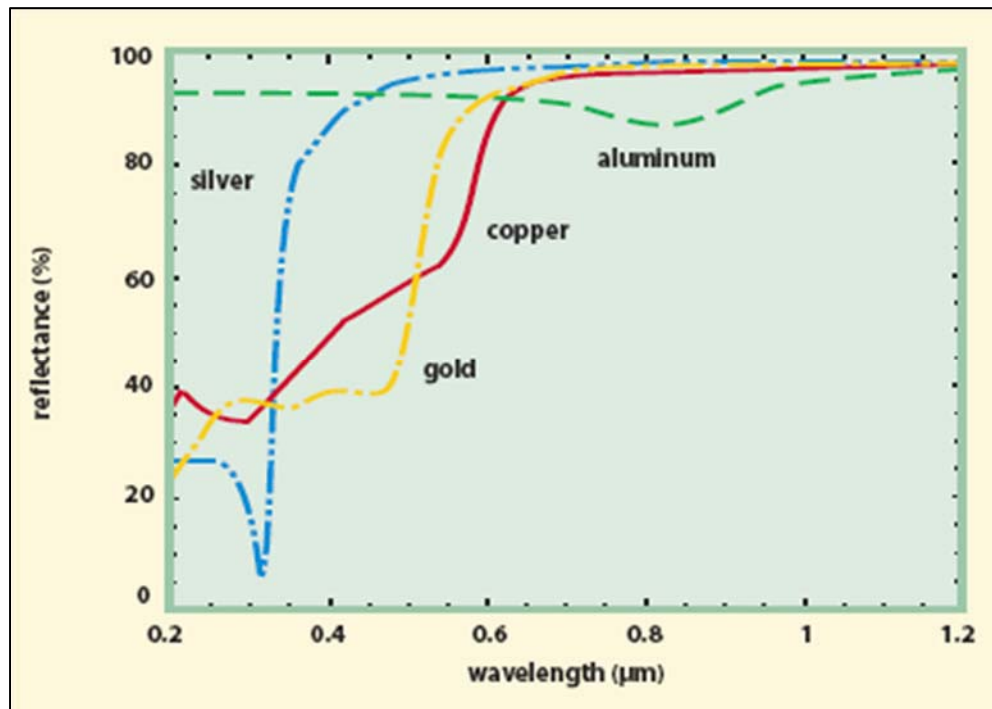


Fig.9. Variation of reflectance with wavelength of light from different color of surfaces.  
 Courtesy: <http://www.photonics.com/EDU/Handbook.aspx?AID=25501>

## 6. Electronic Cirucits

The block diagram of circuit is shown in fig. 10 (a), while several sections of circuits are shown in fig. 10 (b) to (h). Two identical microcontroller PCBs were fabricated. The picture of PCB is shown in fig.10 (i). Two identical PCBs were fabricated. One PCB was used for the payload, while for other PCB was used to stimulate software and backup. The original design was made earlier by Jonathan Wade.

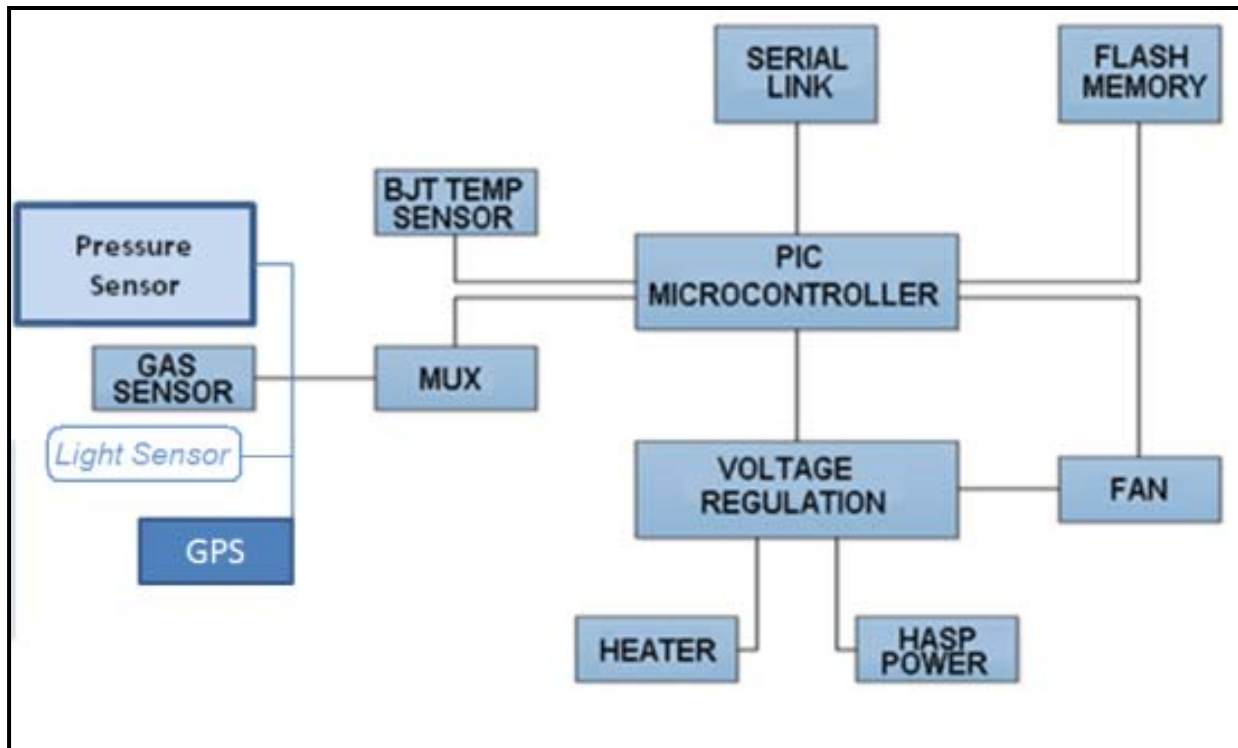


Fig. 10(a) Block diagram of payload circuit

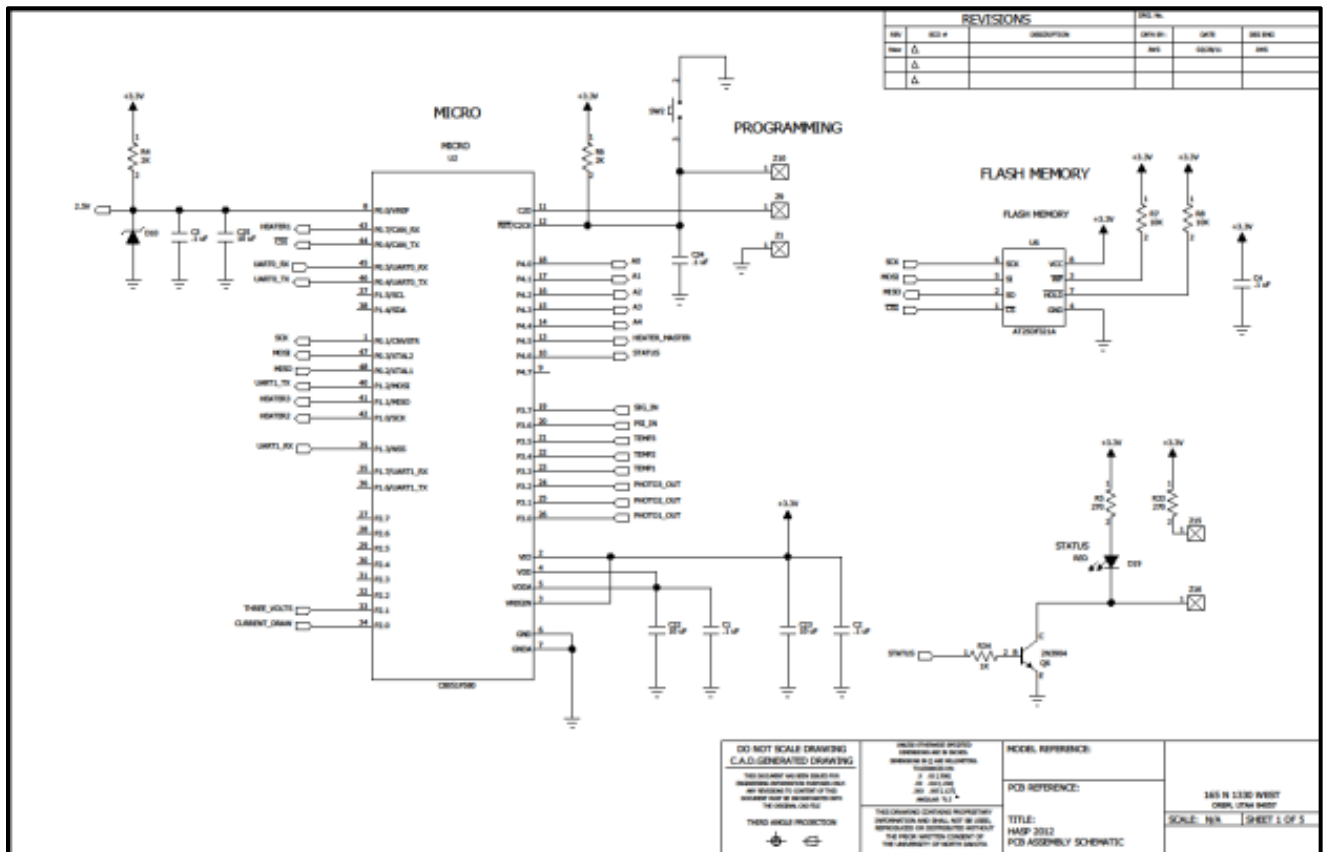


Fig. 10 (b) Circuit for microcontroller and flash memory





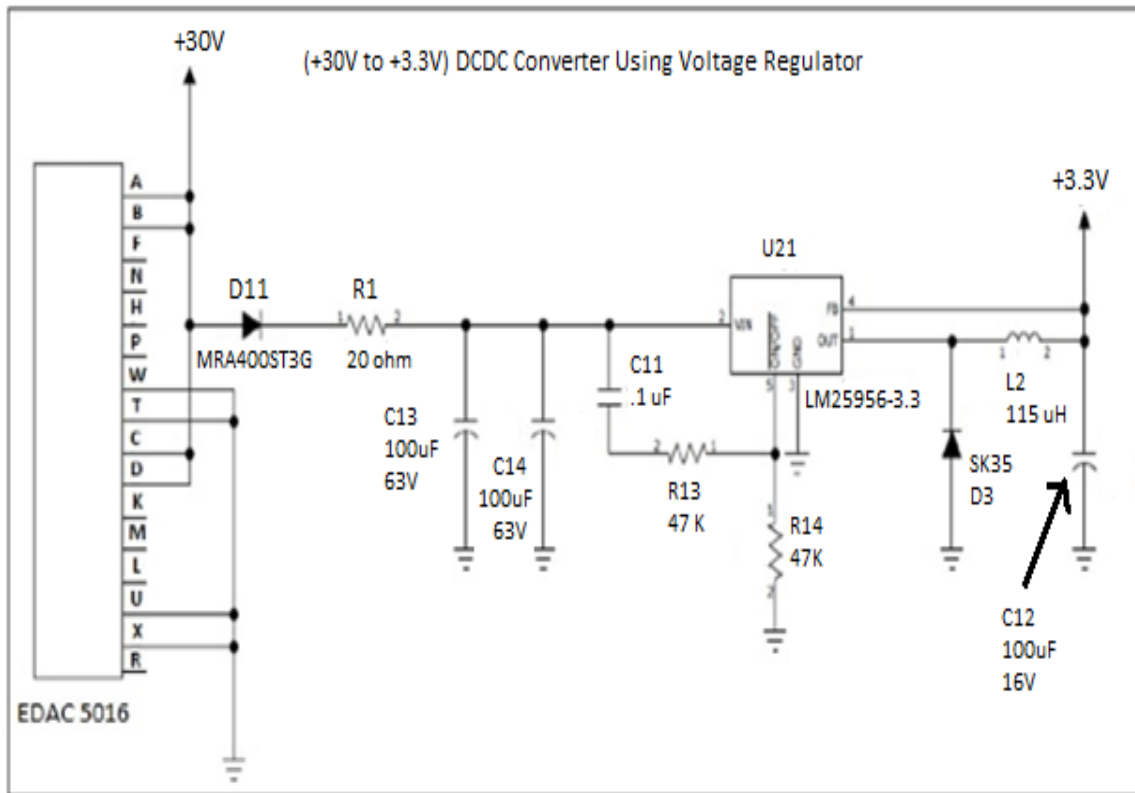


Fig. 10 (e) Voltage regulation circuit

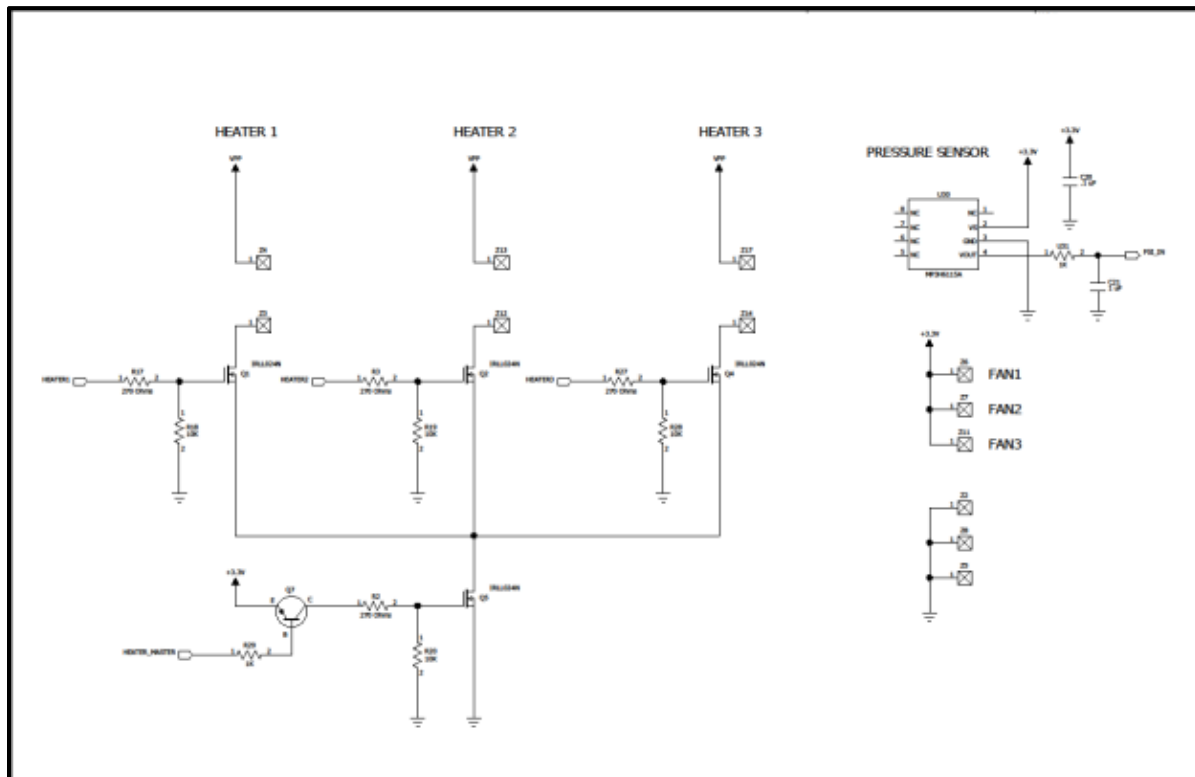


Fig. 10 (f) Circuit for three heaters, three fans and pressure sensor

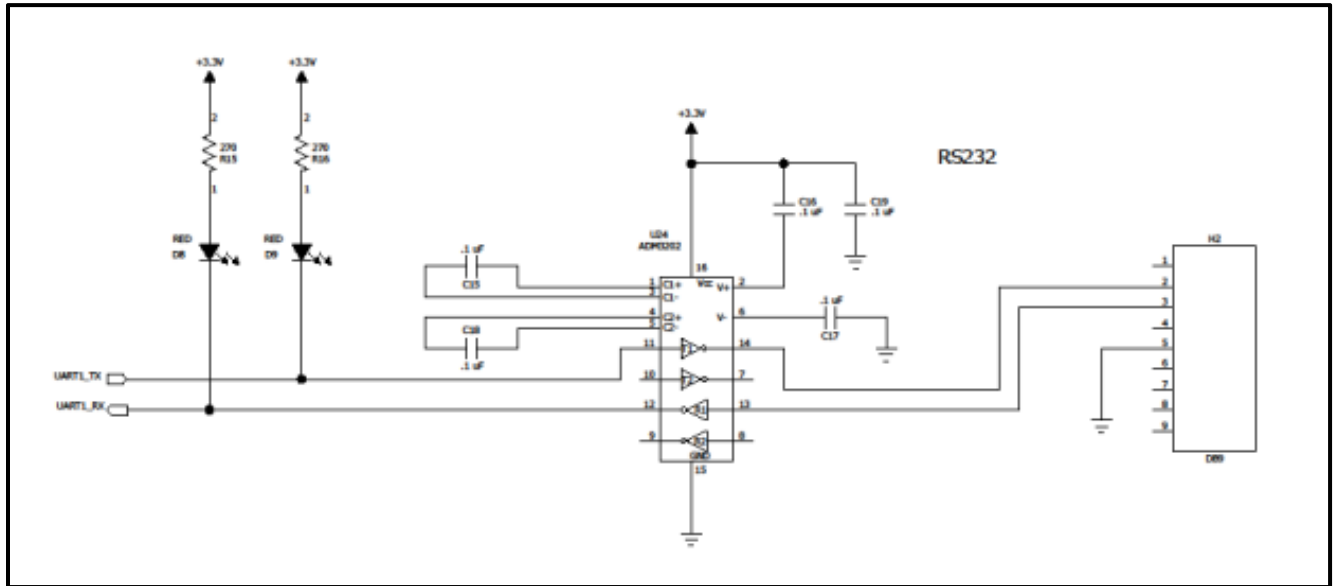


Fig.10 (g) Circuit for RS232

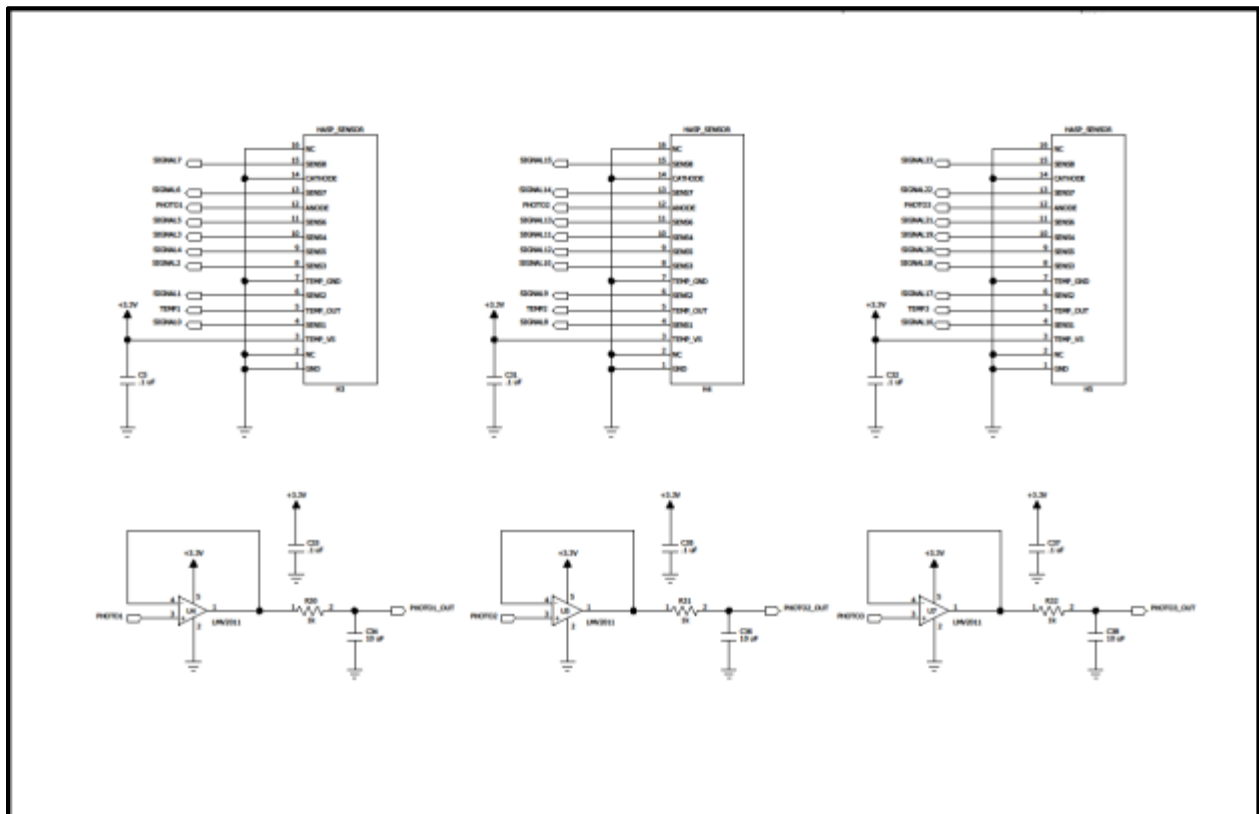


Fig.10 (h) Circuit for three ozone sensors boxes and three photo (light) sensors

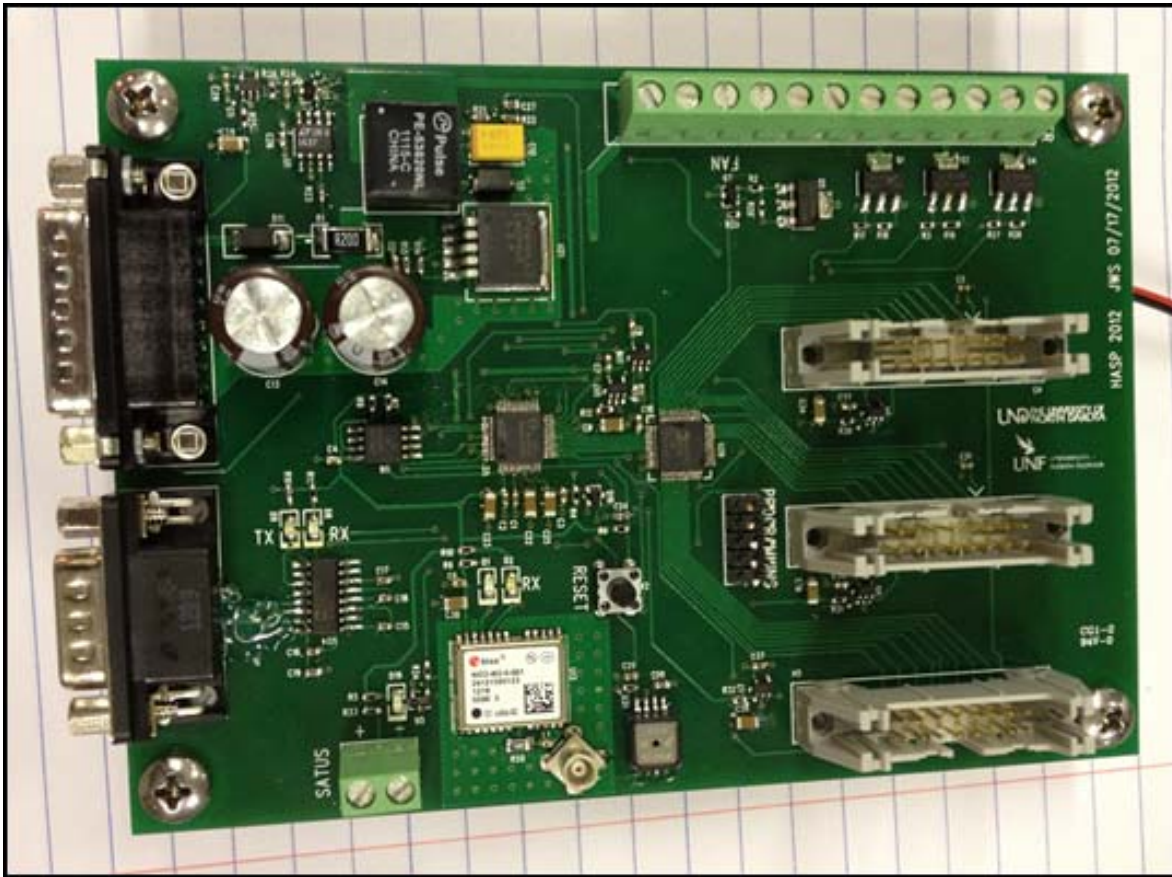


Fig. 10 (i) Picture of microcontroller PCBs

## 7. Integration of Payload and Thermal Vacuum Test

The ozone sensors payload was fabricated and tested at Sensors lab, University of North Florida. Dr. Nirmal Patel (Faculty), Jesse Lard, Ken Emanuel, and Chris Farkas from UNF were participated the HASP integration workshop at the NASA-CSBF, Palestine, TX during July 31 to August 5, 2016. Fig. 11 (a) shows the picture of the UNF student at CSBF, Palestine, TX. The payload was initially tested by Mr. Doug Granger and Mr. Doug Smith and then by Mr. Michael Stewart and DR. Greg Guzik. Fig.11 (b) shows all four sides of the payload, while fig. 11 (c) shows weighing of the payload using the digital balance.



Fig.11 (a) UNF student's team at CSBF, Palestine, TX



Fig. 11 (b) All four sides of the payload

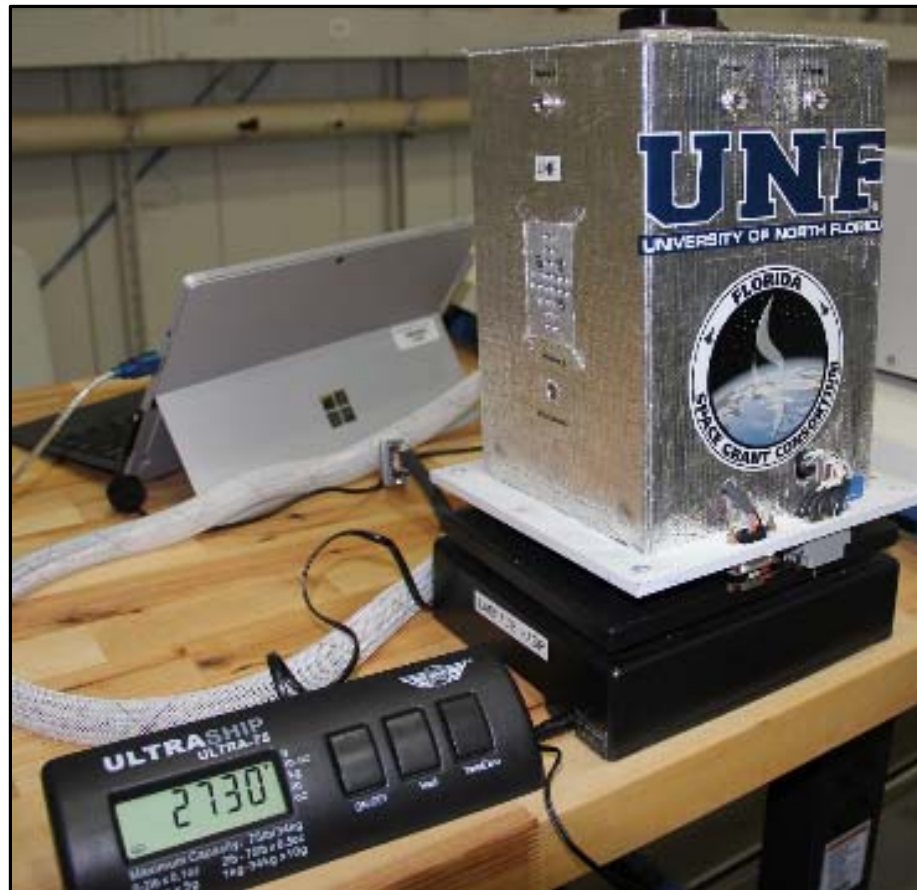


Fig.11 (c) weighing of the payload

Fig.11 (c) shows weighing of the payload using the digital balance. The total mass of payload including its HASP base plate was 2.730 kg, which was less than the limit of 3.00 kg mass of the payload + 0.50 kg mass of the HASP base plate (total 3.5 kg).

The current draw at 30 VDC was measured about  $152 \pm 3$  mA nominal,  $425 \pm 5$  mA maximum and  $31 \pm 3$  mA minimum. The current limit was tested for determination of value of a safety fuse. Fig. 12 (a) shows testing of current by Daugh ( HASP-LSU) and then tested by Dr. Guzik (Fig. 12(b)).



Fig.12 (a) shows Dough is testing of maximum current drawn by the payload.



Fig.12 (b) shows Dr. Guzik with UNF payload during testing procedure.

The payload was tested in the BEMCO chamber, which is shown in Fig. 13(a) for high temperature, low temperature, high pressure, and low pressure. Fig. 3(b and c) shows the

picture of UNF team members during the thermal vacuum test and fig 3(d) shows a picture of group of HASP 2016 participants in front of the thermal vacuum test taken before the thermal vacuum test.



Fig. 13 (a) BEMCO thermal vacuum test chamber



Fig. 13 (b) UNF team-Chris, Nirmal, Ken and Jesse (from Left to right)



Fig. 13 (c) UNF team during thermal vacuum test.



Fig.13 (d) HASP2016 participants



During the thermal vacuum test, all sensors data, pressure transducer, UV light sensors, temperature on sensors, heaters, GPS, data communication and uplink commands were tested and verified several times. The payload was certified for the HASP 2016 balloon flight after successful completion of the thermal vacuum test.

Fig.14 shows the variation of voltage with time during thermal vacuum test. The voltage level was nearly constant during test period. It was found that the average voltage level was 3316 mV with standard deviation of 73 mV.

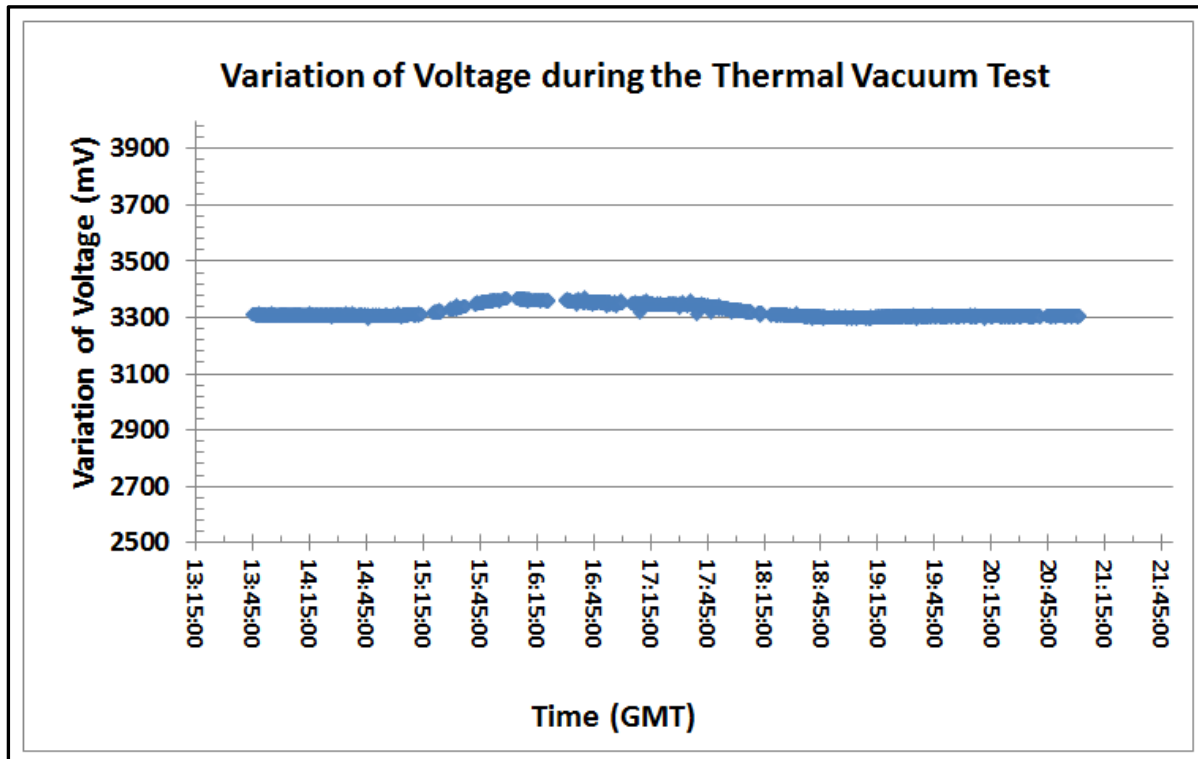


Fig.14 Variation of voltage applied to the payload with time

The current drawn by the payload during the thermal vacuum test is shown in fig. 15 (a). Payload draw (i)  $31 \pm 3$  mA when all three heaters were off, (ii) about  $140 \pm 5$  mA when heater #1 was on, (ii) about  $250 \pm 5$  mA when heaters # 1 and 2 were on, and (iv) about  $350 \pm 5$  mA when all the three heaters #1, 2, and 3 were on. Total time duration for all three heaters on is very small compared to one or two heaters on. It was found during earlier flights that all heaters were only turned on when the flight traveled through the troposphere. It was also observed that all heaters were mostly turned off during the float in the stratosphere. Fig. 15(b) shows the variation of temperature on microcontroller of the payload with time. It shows that the temperature has small variation which is within the tolerance range of the microcontroller of the payload and good thermal stability.

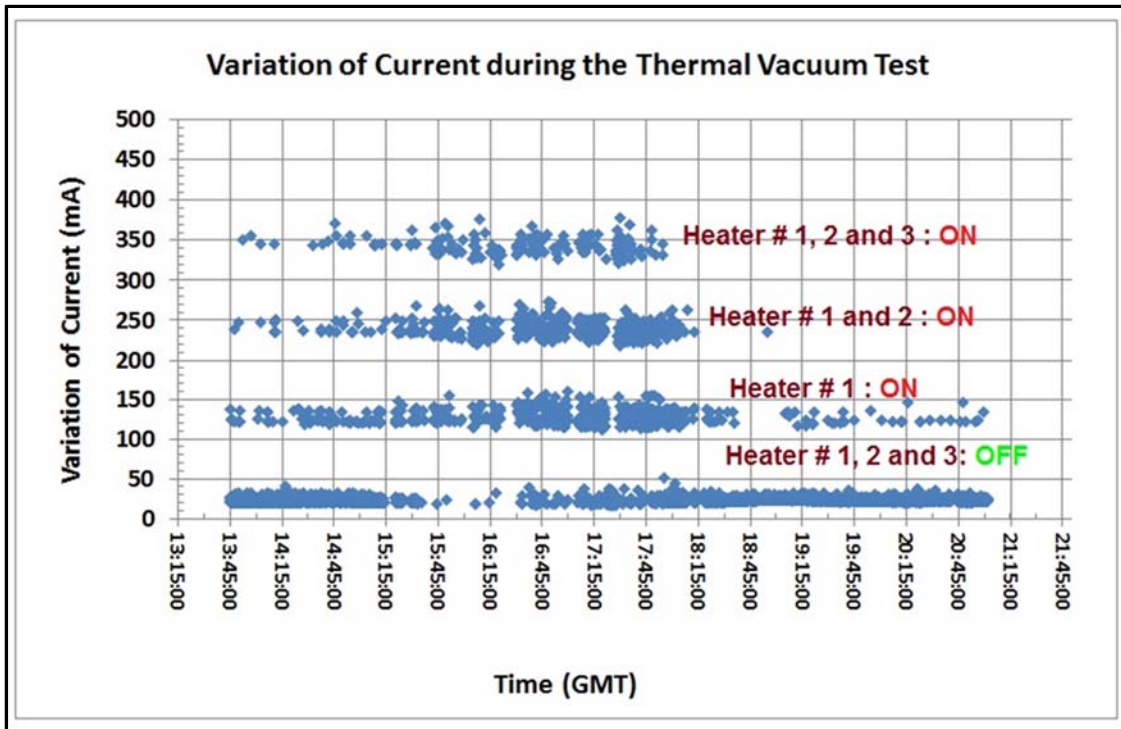


Fig.15(a) Variation of current consumed by the payload with time.

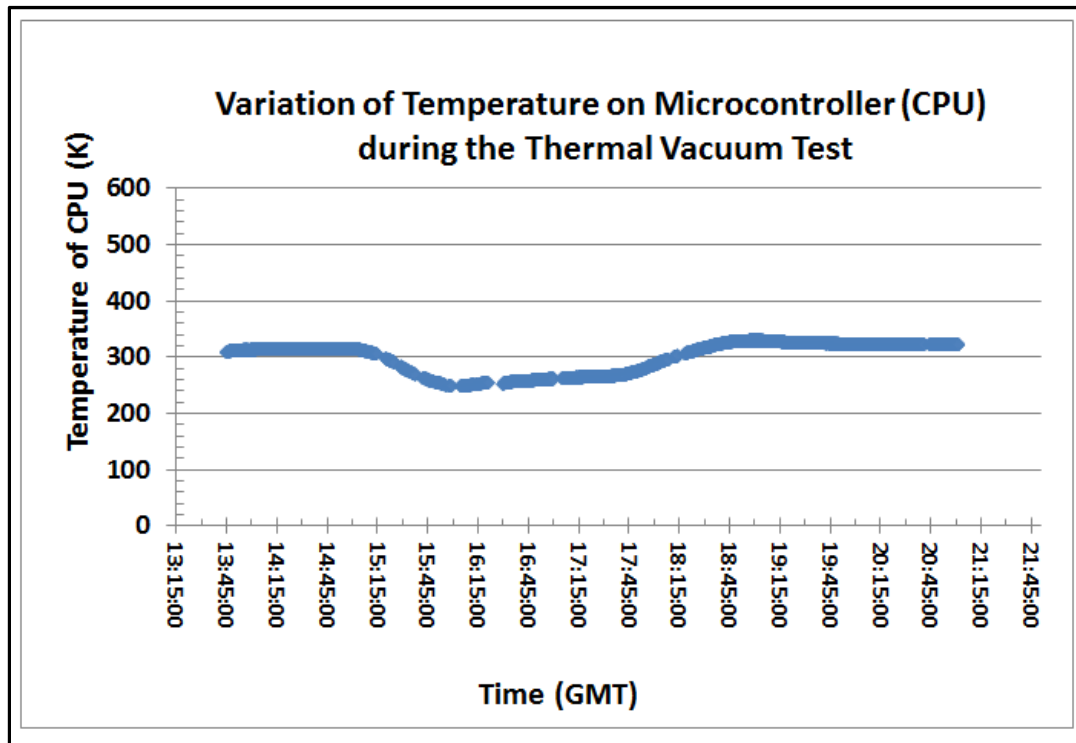


Fig.15 (b) Variation of of temperature on CPU with time.

The variation of pressure measured by the payload during the thermal vacuum test is shown in the fig. 16(a). Our pressure transducer did not measure the pressure below 100 mbar due to the technical limitation and hence saturated. The measured pressure data were nearly matched with the data measured by the HASP pressure transducer, which is shown in the fig. 16(b).

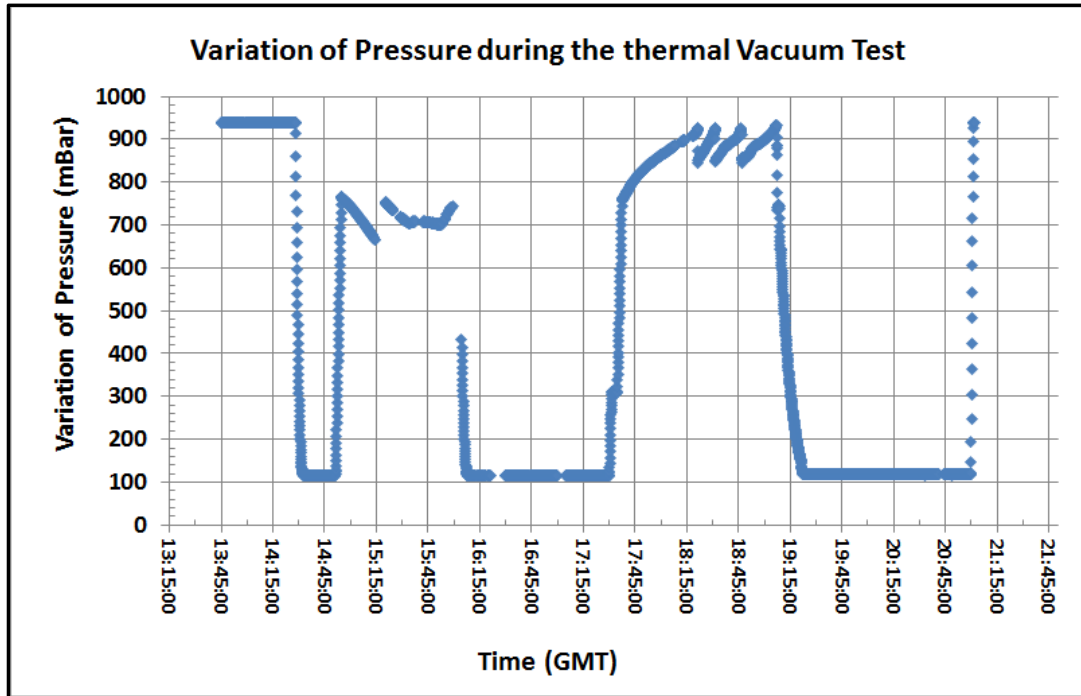


Fig.16 (a) Variation of pressure in the thermal vacuum chamber with time measured by the pressure transducer of UNF payload

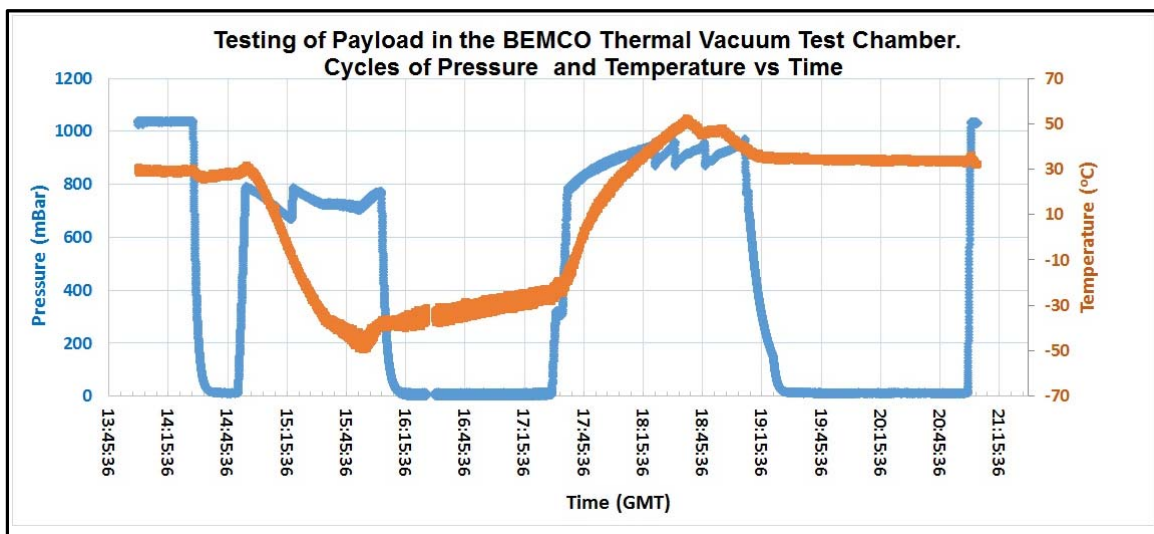


Fig.16 (b) Variation of pressure and temperature in the chamber with time measured by HASP (Data courtesy: Mr. Doug Granger, HASP- LSU).

The resistance of 8 sensors in box #1, 2 and 3 was measured during the thermal vacuum test and are shown in the fig.17 (a), (b) and (c), respectively. It was observed that the resistance of all sensors was nearly constant during the test. It was also found that the resistance was slowly decreasing with time after 18:45 GMT. The ambient temperature in the chamber was set to increase at 18:45 GMT for about 2:15 hours. Due to the semiconducting properties of the sensor materials, it was expected that its electrical resistance should decrease with increasing of ambient temperature. However, that variation was reasonably small.

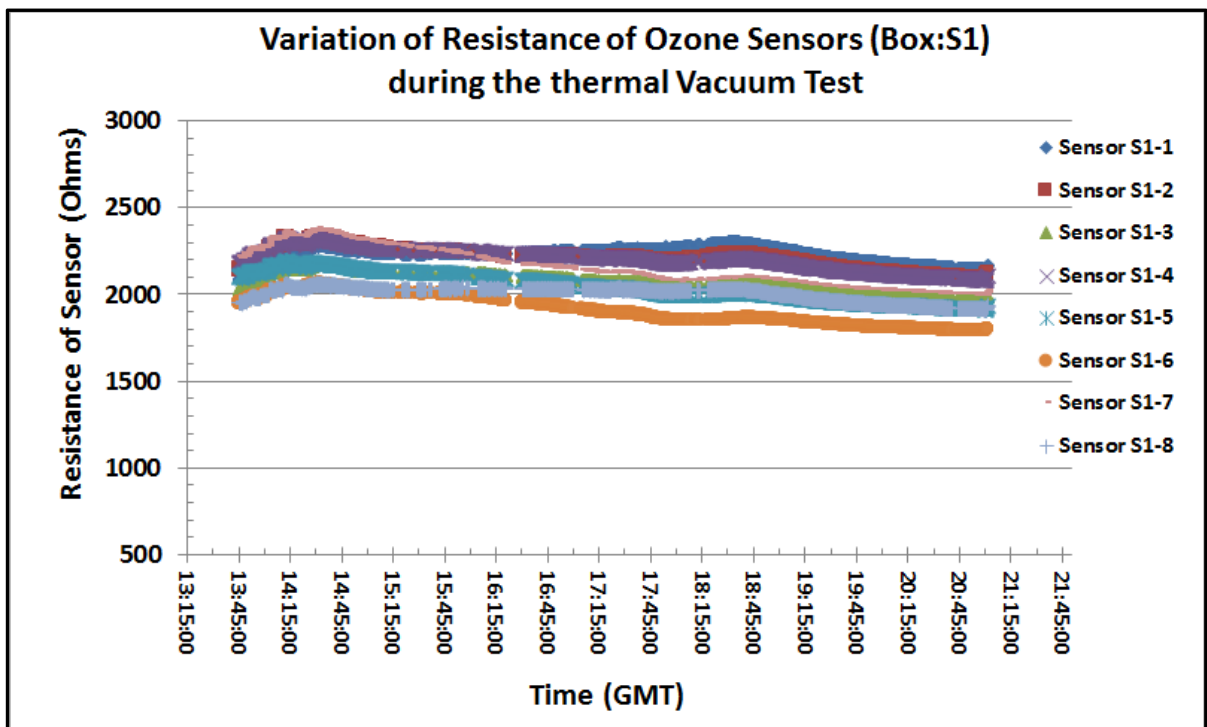


Fig.17 (a) Variation of resistance of gas sensors of sensors box #S1 with time during the thermal vacuum test

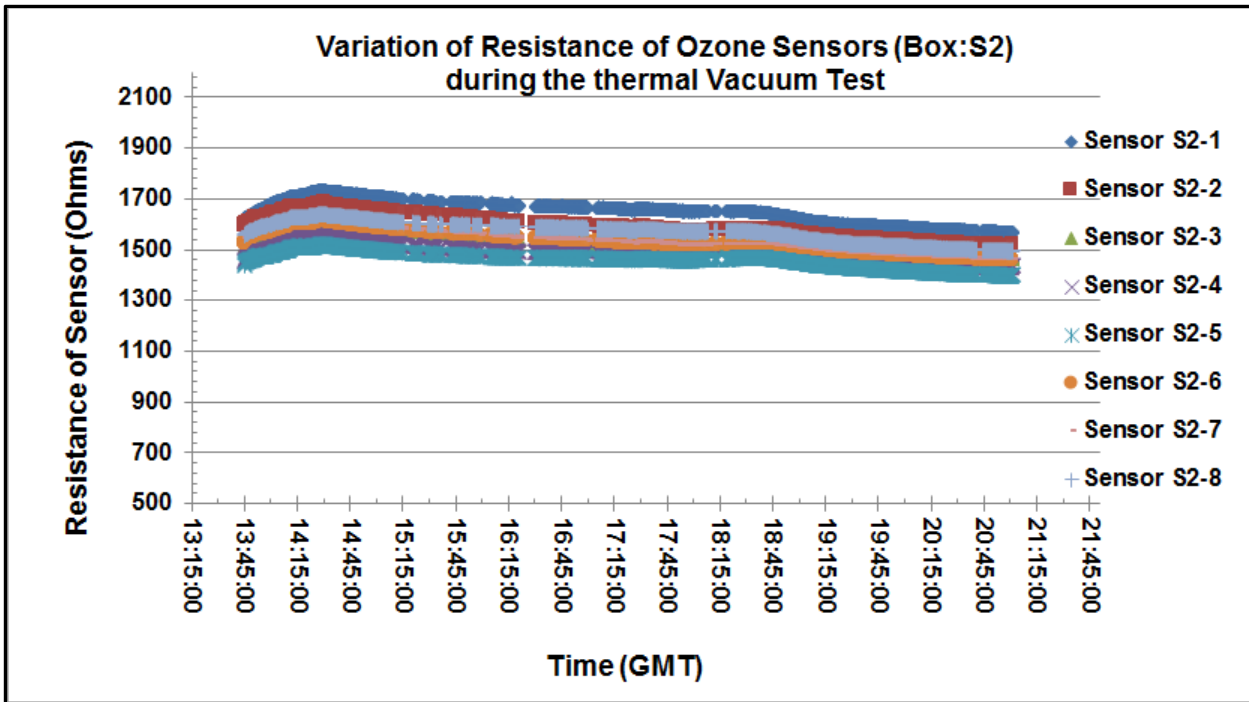


Fig.17 (b) Variation of resistance of gas sensors of sensors box #S2 with time during the thermal vacuum test

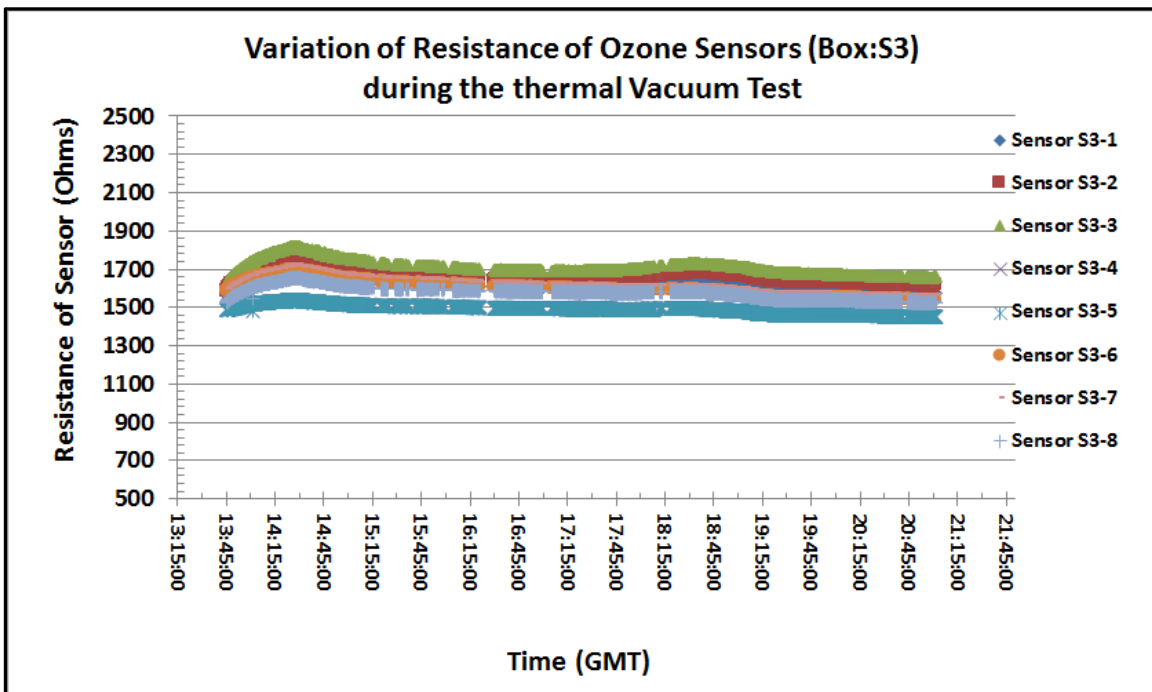


Fig.17 (c) Variation of resistance of gas sensors of sensors box #S3 with time during the thermal vacuum test

It was found that the sensors resistance was quite stable during the low temperature test cycle. A heater mounted on the back side of the sensors array was controlled by the on-off controller and maintained the temperature of sensors array constant during the low temperature test cycle.

Fig.18 shows the variation of temperature of all three sensors arrays with time. It shows all three arrays remain at the constant temperature during the test. A small spike of decrease in temperature was observed around 17:20 to 17:35 GMT due to intentionally turning off heaters and then on for testing of the uplink command.

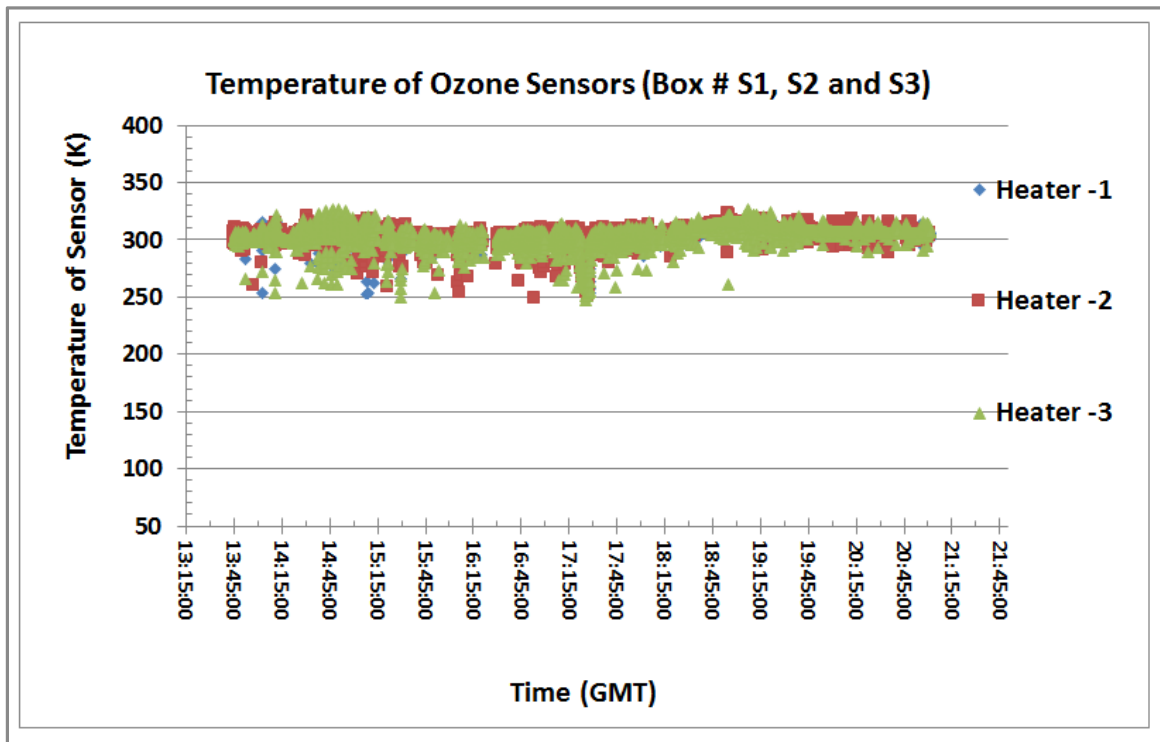


Fig.18 Variation of temperature of gas sensors of sensors box #S1, S2 and S3 with time during the thermal vacuum test

Fig. 19 shows the response of photo diode sensors mounted on sensors boxes with time. It was observed that all three photodiode sensors were in working condition. The variation of phot voltage with time was due to stray light in the chamber, turning on and off the light generated by the incandescent bulbs as well as radiation heaters in the test chamber.

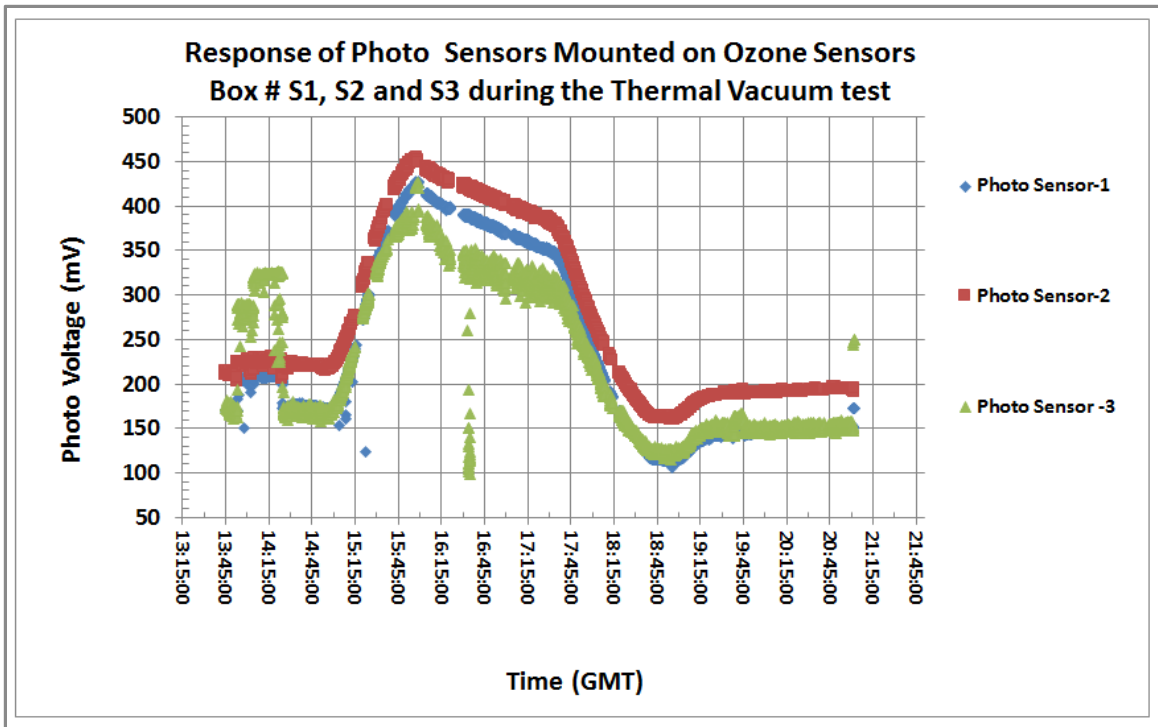


Fig.19 Response of photo sensors mounted on Sensors box #S1, S2 and S3 with time during the thermal vacuum test

During the thermal vacuum test, we have successfully tested five uplink commands. These commands were mainly for rest system, switching the payload GPS to HASP GPS, switching HASP GPS to the payload GPS, switching OFF heater and switching ON heater switch. Fig.20(a) shows how our data were changed in the EXCEL worksheet due to execution of the uplink commands.

HASP2016 Thermal Vacuum Test # 1, August 3, 2016									
Testing of Uplink Commands									
<b>Turn Master Heater Switch OFF</b>									
Command: HEAT_ON Hex Code: 7535									
GPS Stamp	Time (UNIX/GMT)	Time (CST)	Time (GMT)	VOLT(mV)	CURRENT(mA)	PRESSURE (mBar)	Heater Status		
HASP2016 UBLOX	172125	12:21:25 PM	17:21:25	265	3346	236	116	110	
HASP2016 UBLOX	172130	12:21:30 PM	17:21:30	265	3346	126	116	10	
HASP2016 UBLOX	172135	12:21:35 PM	17:21:35	264	3346	327	116	111	
HASP2016 UBLOX	172140	12:21:40 PM	17:21:40	265	3346	22	116	1111	
HASP2016 UBLOX	172145	12:21:45 PM	17:21:45	264	3346	19	116	1111	
<b>Turn Master Heater Switch ON (Default)</b>									
Command: HEAT_OFF Hex Code:7636									
HASP2016 UBLOX	172735	12:27:35 PM	17:27:35	265	3347	25	116	1111	
HASP2016 UBLOX	172740	12:27:40 PM	17:27:40	264	3347	17	116	1111	
HASP2016 UBLOX	172745	12:27:45 PM	17:27:45	265	3347	332	116	111	
HASP2016 UBLOX	172750	12:27:50 PM	17:27:50	265	3347	337	116	111	
<b>"Reset System" shown by "Hello" in the data string</b>									
Command: RESET Hex Code: 7131									
GPS Stamp	Time (UNIX/GMT)	Time (CST)	Time (GMT)	S1-4 (Ohm)	S1-5 (Ohm)	S1-6 (Ohm)	S1-7 (Ohm)	S1-8 (Ohm)	
HASP2016 UBLOX	175350	12:53:50 PM	17:53:50	2179	1999	1853	2088	2019	
HASP2016 UBLOX	175355	12:53:55 PM	17:53:55	2184	1997	1853	2085	2019	
HASP2016 UBLOX	175400	12:54:00 PM	17:54:00	2179	2002	HELLO			
HASP2016 UBLOX	175410	12:54:10 PM	17:54:10	2189	2004	1857	2088	2019	
<b>Changing our payload GPS (HASP2016 UBLOX) to HASP GPS (HASP2016)</b>									
Command: HASP_STREAM Hex Code: 7A3A									
GPS Stamp	Time (UNIX/GMT)	Time (CST)	Time (GMT)						
HASP2016 UBLOX	180815	1:08:15 PM	13:08:15						
HASP2016 UBLOX	180820	1:08:20 PM	13:08:20						
HASP2016 UBLOX	180825	1:08:25 PM	13:08:25						
HASP2016	1470247707	1:08:27 PM	13:08:27						
HASP2016	1470247712	1:08:32 PM	13:08:32						
<b>Changing HASP GPS (HASP2016) to our payload GPS (HASP2016 UBLOX) (Default)</b>									
Command: UBLOX_STREAM Hex Code: 7939									
GPS Stamp	Time (UNIX/GMT)	Time (CST)	Time (GMT)						
HASP2016	1470247897	1:11:37 PM	13:11:37						
HASP2016	1470247902	1:11:42 PM	13:11:42						
HASP2016	1470247907	1:11:47 PM	13:11:47						
HASP2016 UBLOX	181155	1:11:55 PM	13:11:55						

Fig.20 (a). Testing of uplink commands during the thermal vacuum test



Our GPS has also measured the altitude during the thermal vacuum test. The measured values of altitude with time is shown in the Fig.20 (b). It shows that the plot is nearly constant and having average value of  $140 \pm 5$  m. The magnitude of values may not be correct as it was measured inside the chamber but nearly constant, which indicates our GPS was working well. In addition, these data were nearly matched with the HASP GPS.

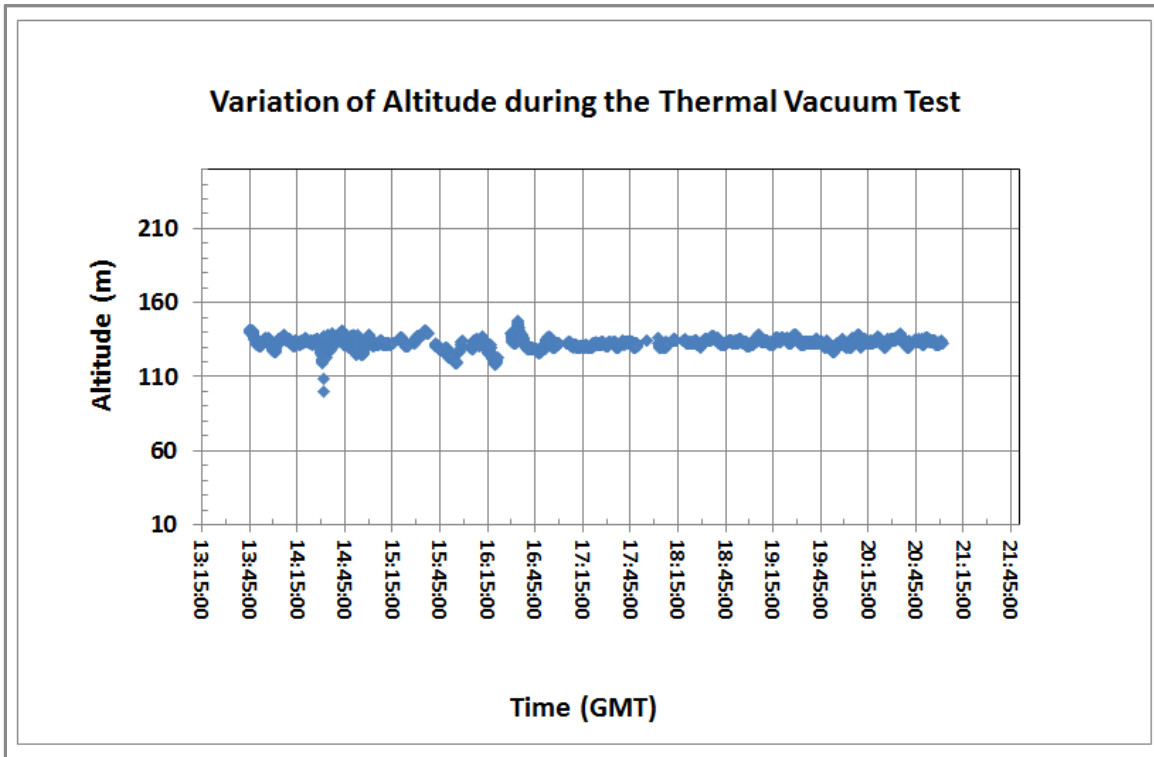


Fig. 20(b) Measured altitude with time during the thermal vacuum test.

After successful completion of the thermal vacuum test, the payload was disintegrated from the HASP platform. It was packed in the shipping box and then transported to the CSBF, Fort Sumner, NM.

## 8. Launching of Payload

The payload was again mounted on the HASP platform and performed the power ON and data communication tests at the CSBF, Fort Sumner. Fig. 21 (a) to (i) shows the pictures of testing of all payloads, hang test, launch preparation, inflating of balloon and launching of balloon at the CSBF, Palestine, TX.



Fig. 21(a) Testing of payload at CSBF, Palestine, NM



Fig. 21(b) Hang Test of payload at CSBF, Palestine, NM

(Courtesy: Doug Granger, HASP-LSU)



Fig. 21(c) Launch preparation and attaching the parachute with the HASP.



Fig.

Fig.21(d) Inflating the balloon with helium gas.

(Courtesy: Doug Granger, HASP-LSU)



Fig. 21 (g) HASP Balloon



Fig. 21(f) HASP on “BIG BILL” vehicle. Rainbow was observed in the sky due to cloud and rain.

(Courtesy: Doug Granger, HASP-LSU)



Fig.21 (g) Final touch of launching



Fig. 21 (h) Launching of balloon  
(Courtesy: Doug Granger, HASP-LSU)

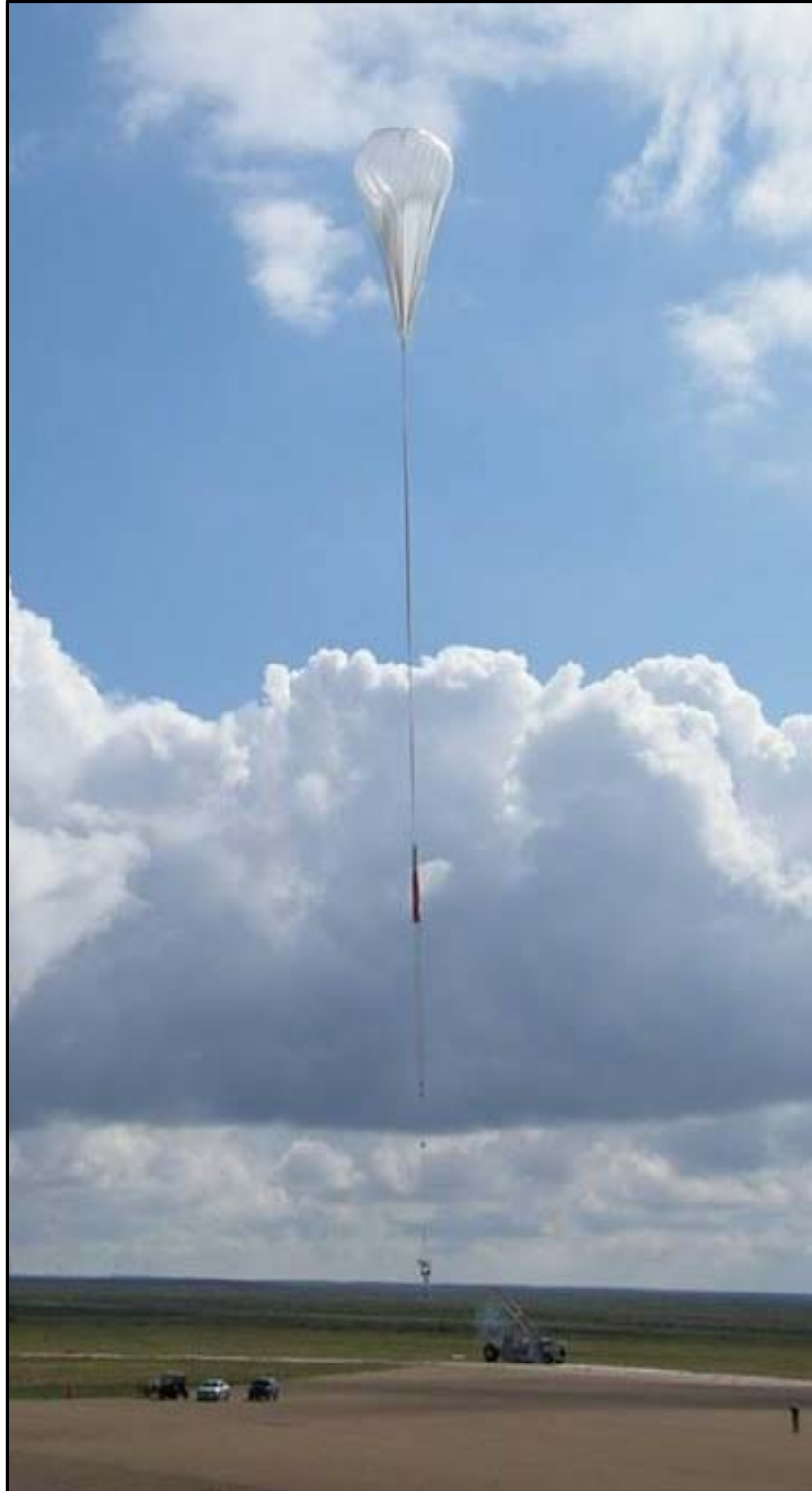


Fig. 21(i) Lift up of HASP.

(Courtesy: Doug Granger, HASP-LSU)

HASP2016 flight was successfully launched into the stratosphere at an altitude of about 120,000 feet from the NASA- CSBF, Fort Sumner, NM on Thursday, September 1, 2016 at 12:08 EST.

Fig. 22 (a) shows the HASP 2016 balloon flight system information,

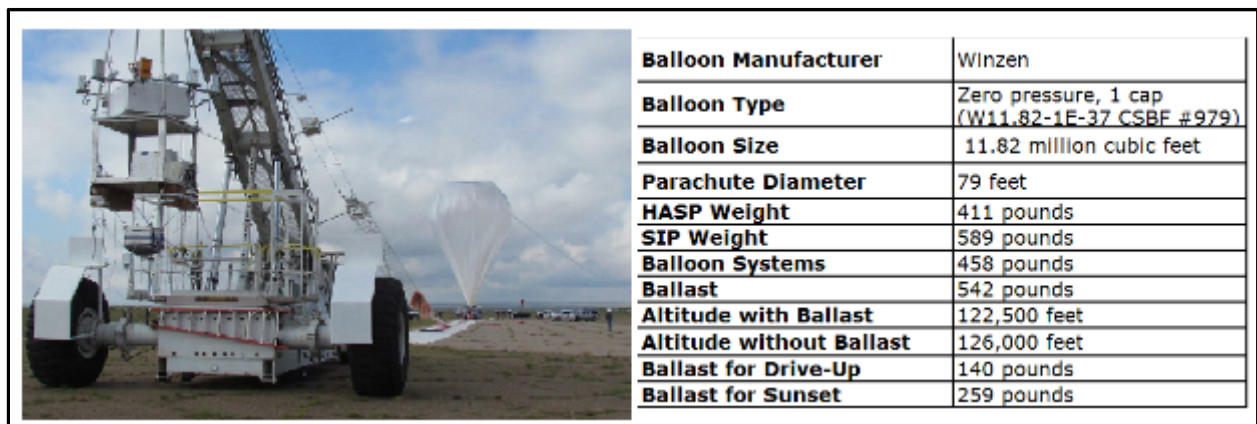


Fig. 22 (a) Flight system information (Courtesy: <http://laspace.lsu.edu/hasp/Flightinfo.php>)

Fig. 22 (b) shows the flight path of the balloon on the Google map.

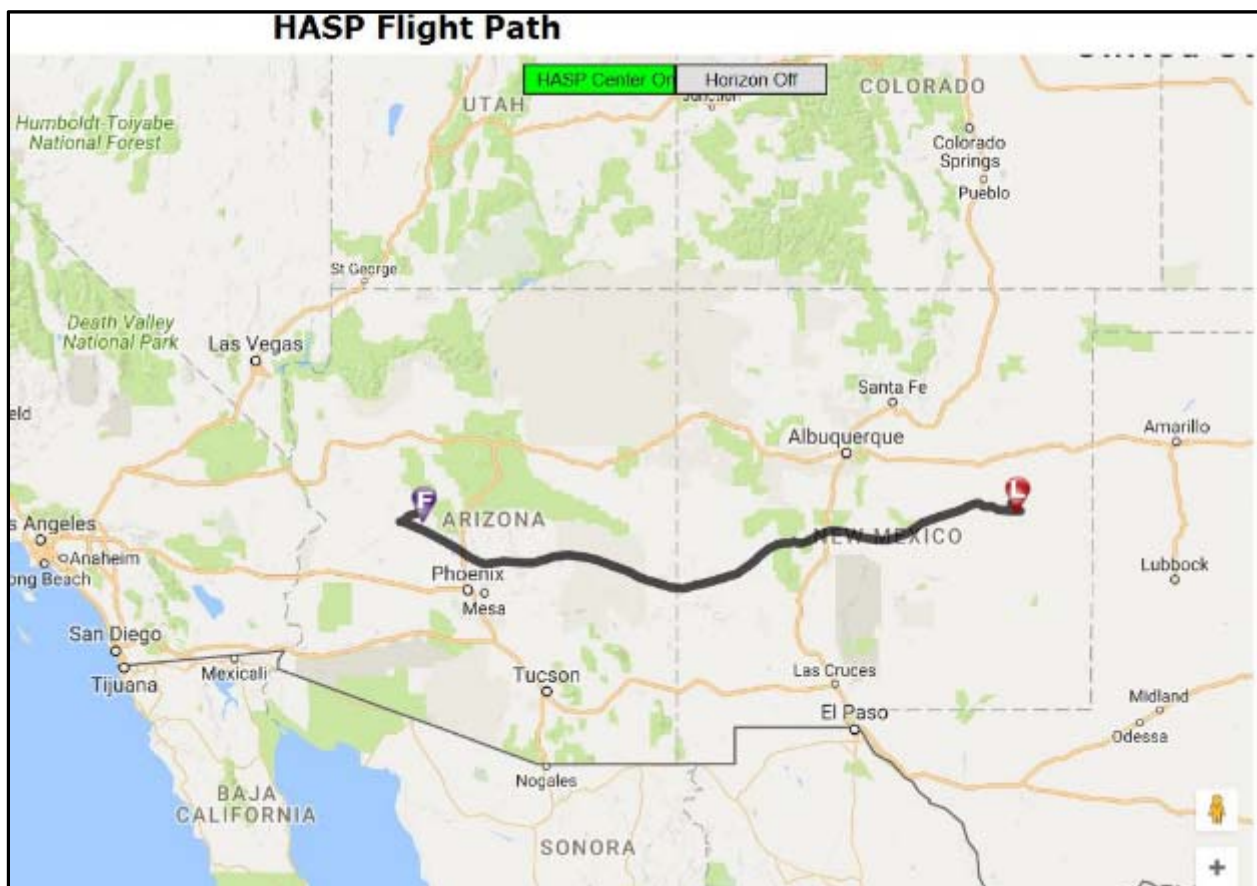


Fig.22 (b) Flight path of the balloon flight on the Google map

The HASP balloon flight was terminated and then impacted near Grand View, AZ on September 2, 2016. Fig. 23 (a) to (c) shows the pictures of impact of HASP on the ground after termination. The parachute, HASP and vehicles of recovery team are shown in the pictures. We are thankful to Doug Granger for sharing the pictures.



Fig. 23 (a) Impact of HASP on the ground.





Fig. 23 (b) Impact of the parachute on the ground and recovery team member.



Fig. 23 (c) shows UNF payload was narrowly escaped from the direct hit on the ground,

## 9. Results and Discussions:

### 9.1 How ozone profile measured in the Starosphere?

Fig. 24 shows various steps for the detection of ozone by the sensors payload during the flight.

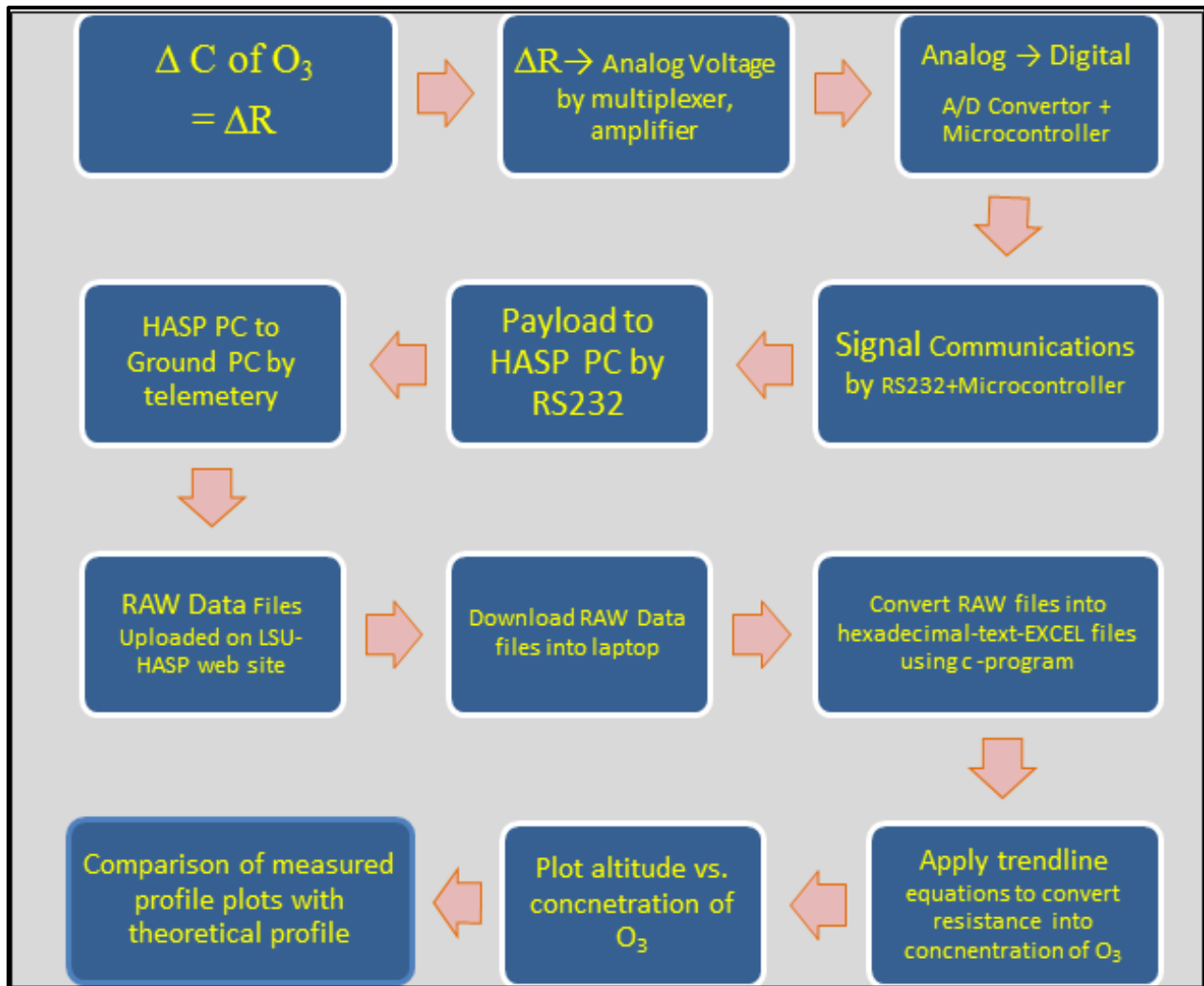


Fig.24 Steps for the detection of ozone by the payload

During the flight, UND-UNF sensors payload measured the ozone profile. The payload sent data files of 25 KB every 18 minutes during the flight time through the NASA-HASP computer and was uploaded on the HASP website. We downloaded all the RAW data files, and converted RAW files into one EXCEL file using the software program. It was found that the sensors, hardware and software worked very smoothly. During the flight, uplink commands for rest, switching the HASP GPS to UBLOX GPS, heater ON and heater OFF were successfully tested.

## 9.2 Balloon Flight Profile and Response of Pressure Sensor

Fig. 25 shows the HASP 2016 balloon flight profile. The altitude profile was measured by our payload GPS. Our UBLOX GPS worked very well during the flight. We did not need to switch to HASP GPS. The average altitude was around 37015 m during the float.

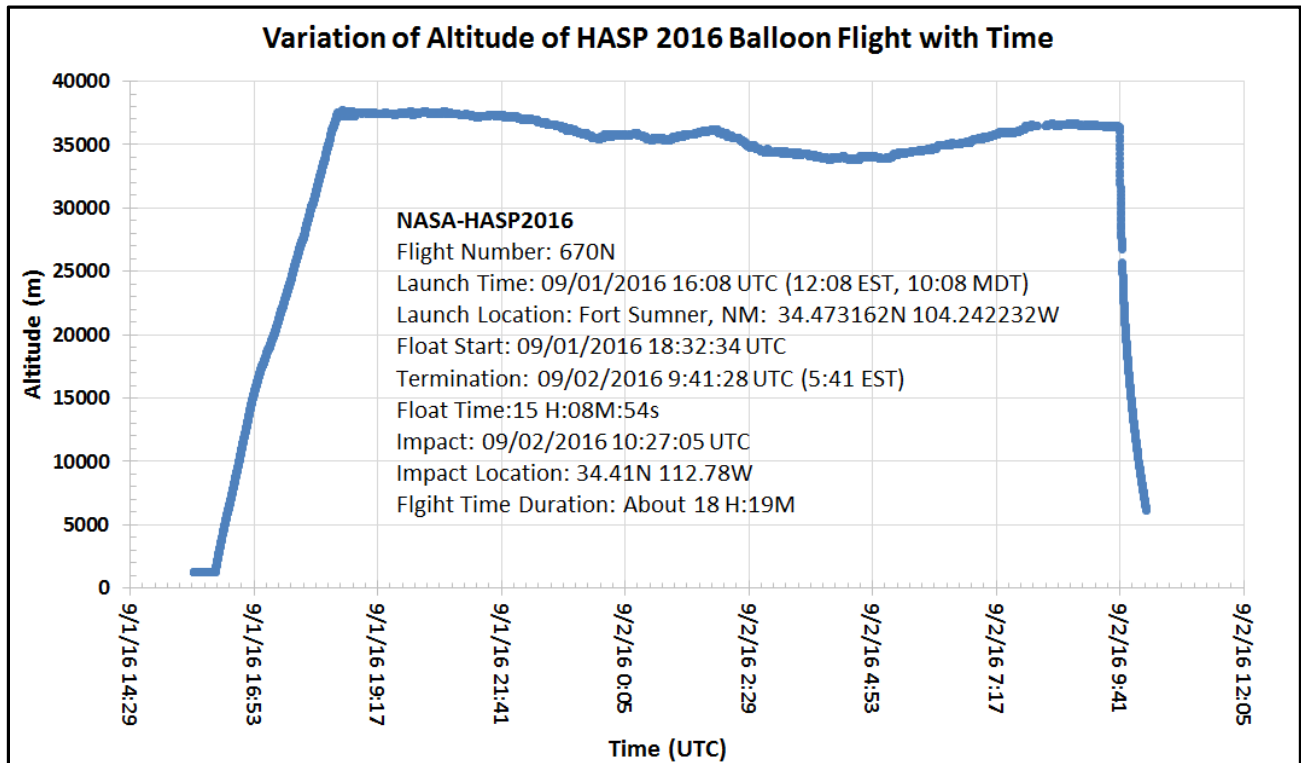


Fig.25 HASP2016 flight profile

Fig.26 (a) shows the variation of pressure with the altitude during the flight. Pressure was measured by a pressure sensor mounted on the PCB of the payload. It was found that the pressure was decreased with increase of the altitude up about 17 km and then nearly saturate with increase of altitude up to the float. The saturation of pressure around 100 mbar was due to the technical limitation of our pressure sensor. We were not able to change it this year but will replace this pressure sensor with one having lower mbar range in the next balloon flight.

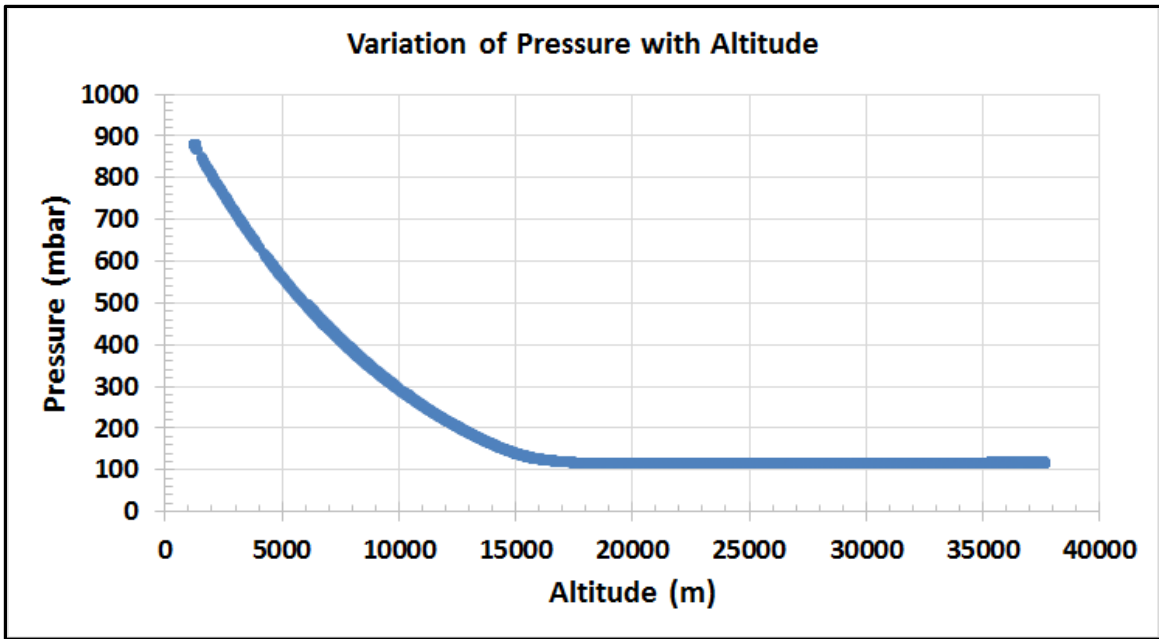


Fig.26 (a) Variation of pressure with altitude

Fig. 26 (b) shows the variation of pressure measured by the payload with the flight time (UTC). It shows change of pressure with time during ascending and termination of the flight.

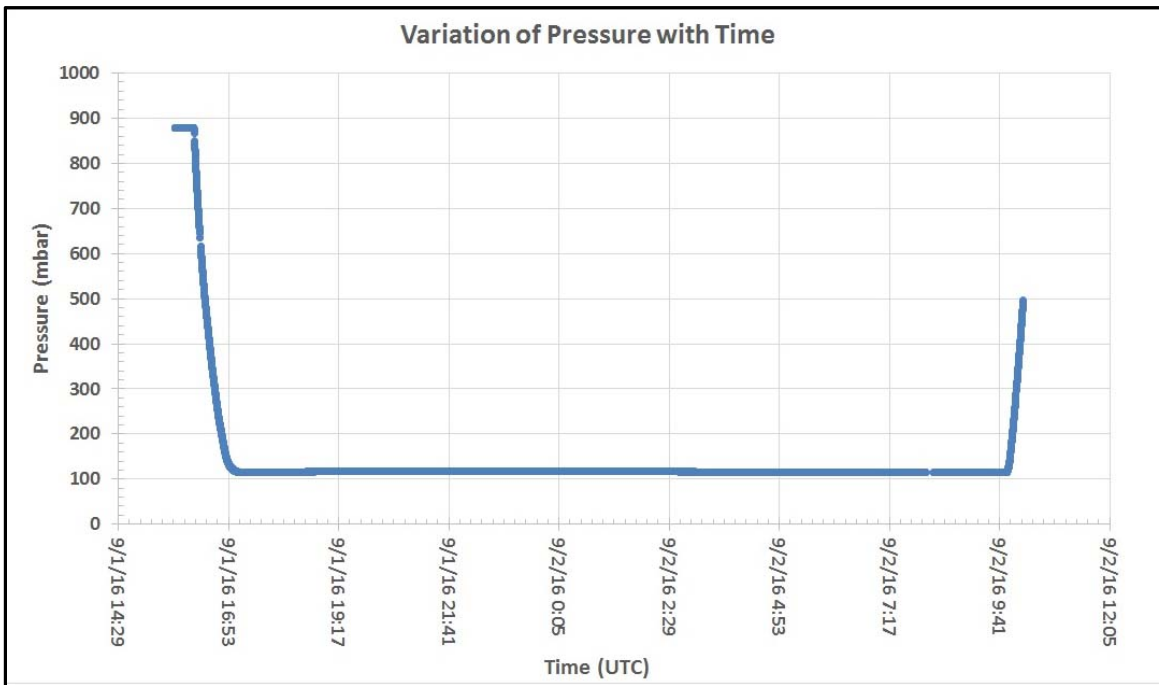


Fig.26 (b) Variation of pressure with time (UTC).

### 9.3 Power budget during the flight

Fig.27 shows the voltage applied to the payload during the flight. It was found that applied average voltage remain nearly constant about 3320 mV.

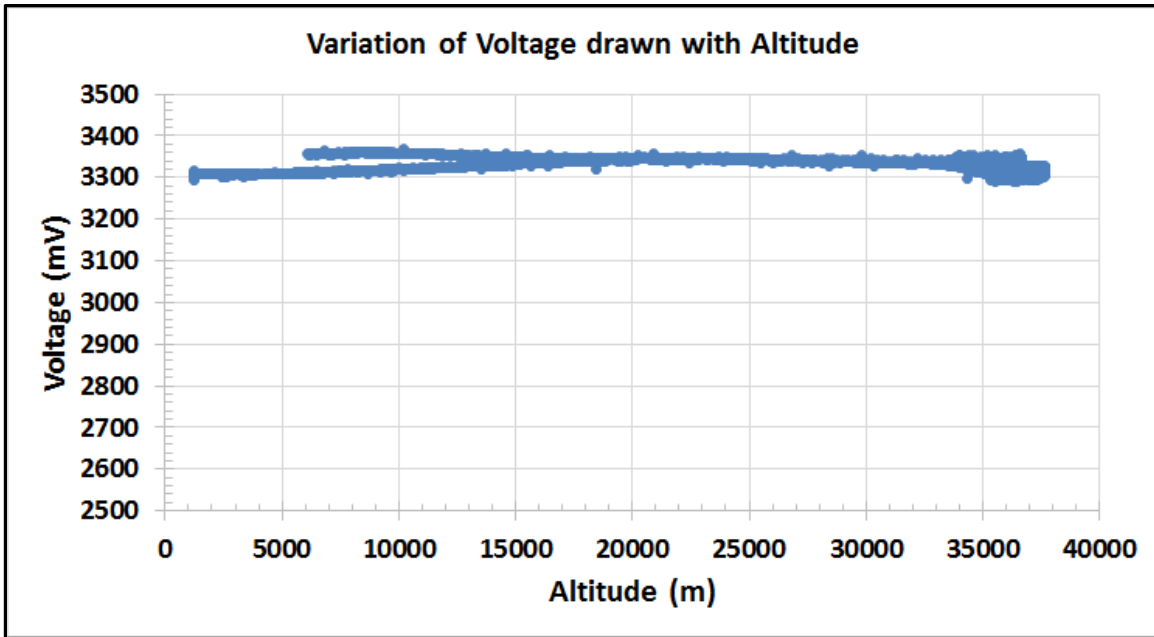


Fig.27 Voltage applied to the payload during the flight.

The current drawn by the payload during the flight is shown in fig. 28.

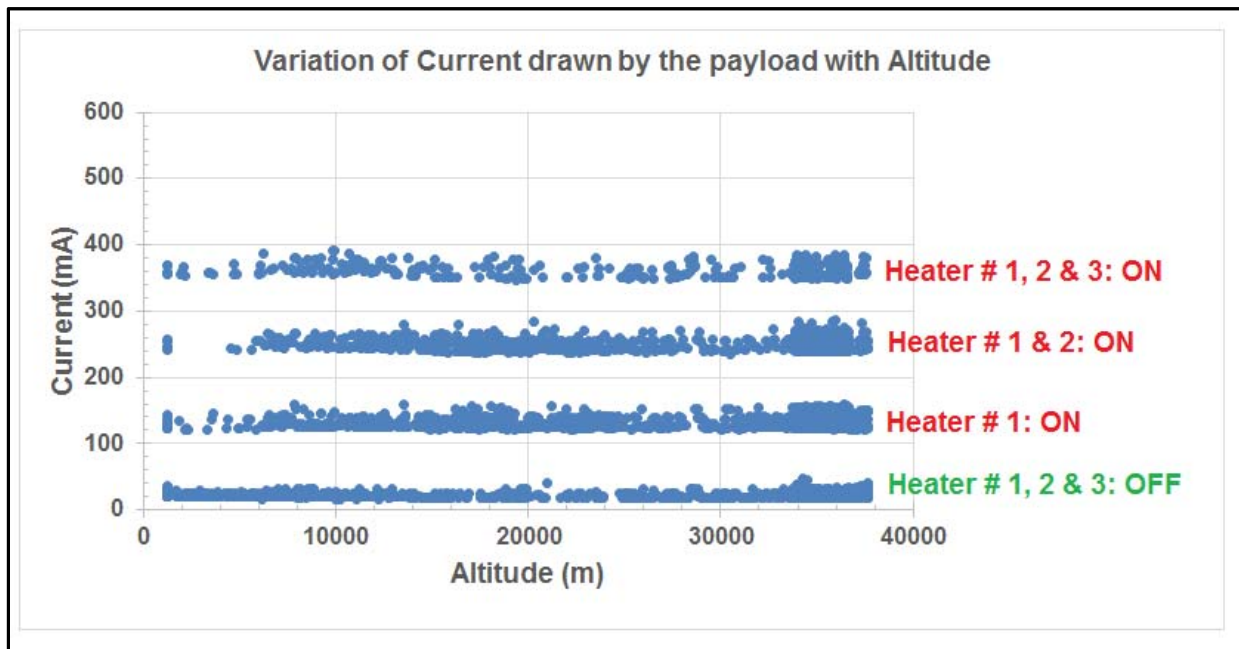


Fig.28 Current drawn by the payload during the flight

The current drawn by the payload during the flight was

- (i) About  $30 \pm 5$  mA when all three heaters were off,
- (ii) About  $140 \pm 10$  mA when Heater #1 ON,
- (iii) About  $250 \pm 10$  mA when Heater # 1 and 2 ON and
- (iv) About  $360 \pm 20$  mA when all three heaters were ON.

The power budget was maintained under the upper limit of HASP requirement during the flight.

#### 9.4 Thermal stability of the payload

The variation of temperature of ozone sensors box #1, 2 and 3 with altitude during the flight is shown in fig.29 (a) to (c), respectively. The temperature of sensors was controlled in the range of  $302 \pm 5.7$  K using an On-Off controller, a polyimide flexible heater (MINCO make) and a temperature sensor (TMP 36). Temperature of sensors was well controlled during the most of time of the flight.

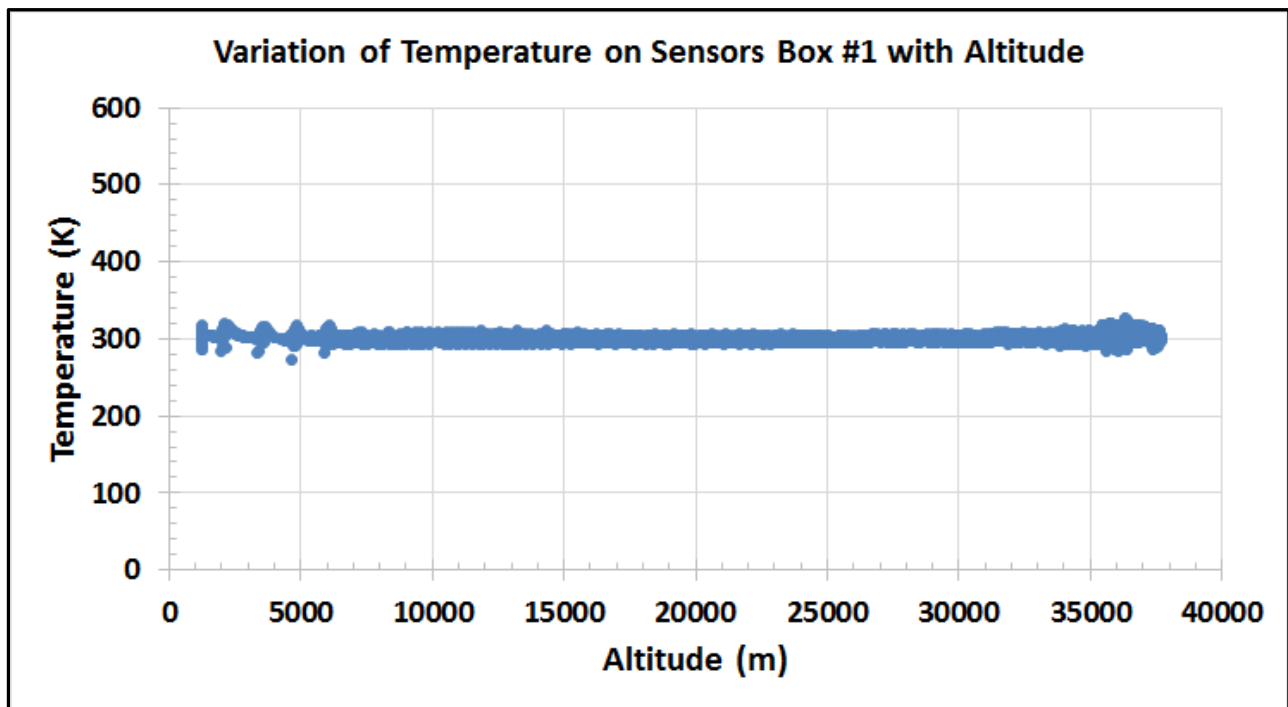


Fig.29 (a) Variation of temperature of ozone sensors in box#1 with altitude

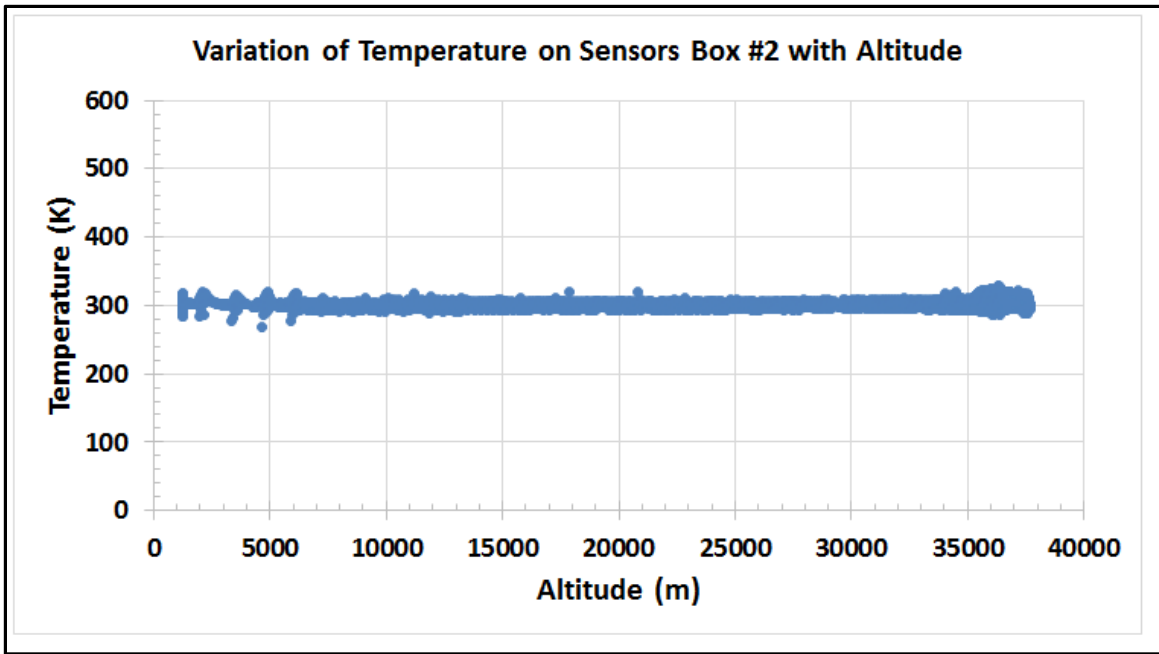


Fig.29 (b) Variation of temperature of ozone sensors in box#2 with altitude

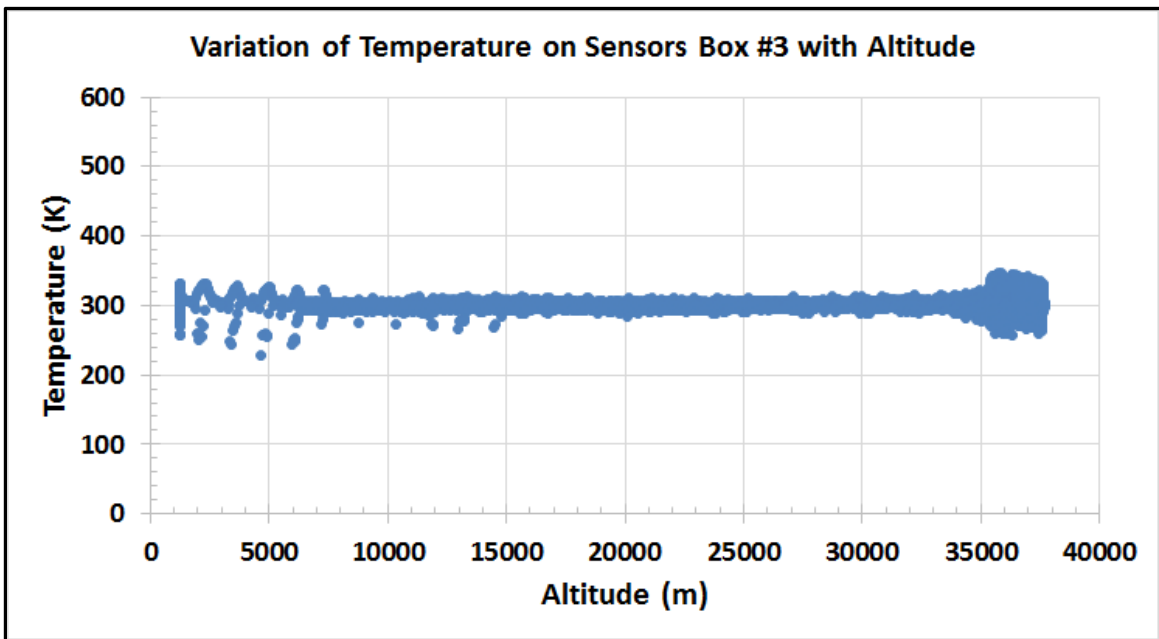


Fig.29 (c) Variation of temperature of ozone sensors in box#3 with altitude

Table-3 shows the measured average temperature, standard deviation and one sigma standard error of temperature of sensor box#1, 2 and 3.

Sensors Box #	1	2	3
Average Temperature (K)	303.9	304.2	305.9
Standard Deviation (K)	6.3	6.7	10.4
Standard Error (K)	0.05	0.06	0.09

Table 3. Average temperature and standard deviation of temperature of sensors array 1, 2 and 3 during the flight.

Variation of temperature of ozone sensors in box#1, 2 and 3 with time (UTC) is shown in the fig. 30(a), (b) and (c), respectively. All three plots shows the reasonable stability of temperature of ozone sensors in the box # 1, 2 and 3. It was observed that temperature of sensors in box #3 got more variation during float, particular at night time.

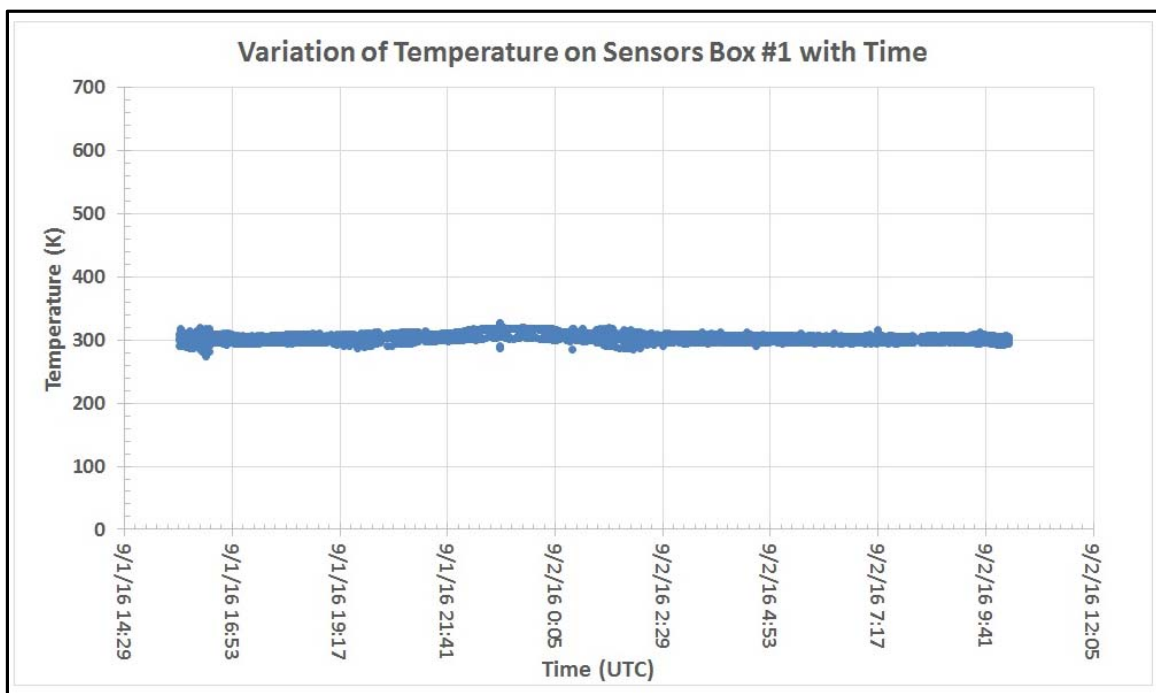


Fig.30 (a) Variation of temperature of ozone sensors in box#1 with time (UTC)



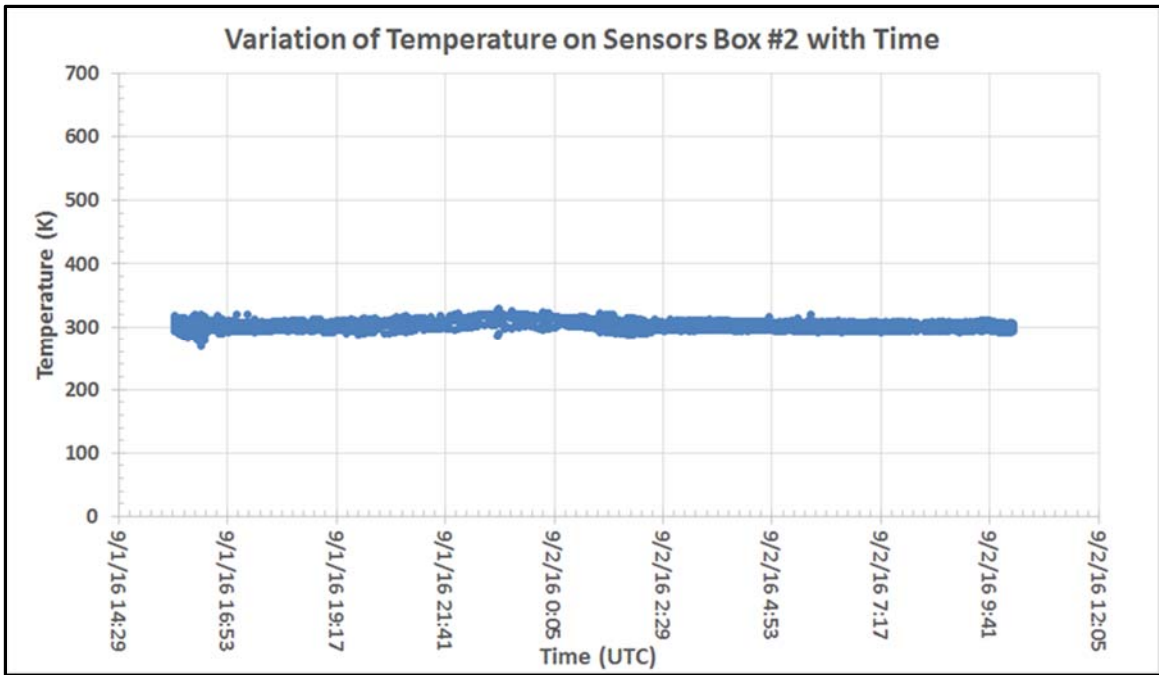


Fig.30 (b) Variation of temperature of ozone sensors in box#2 with time (UTC)

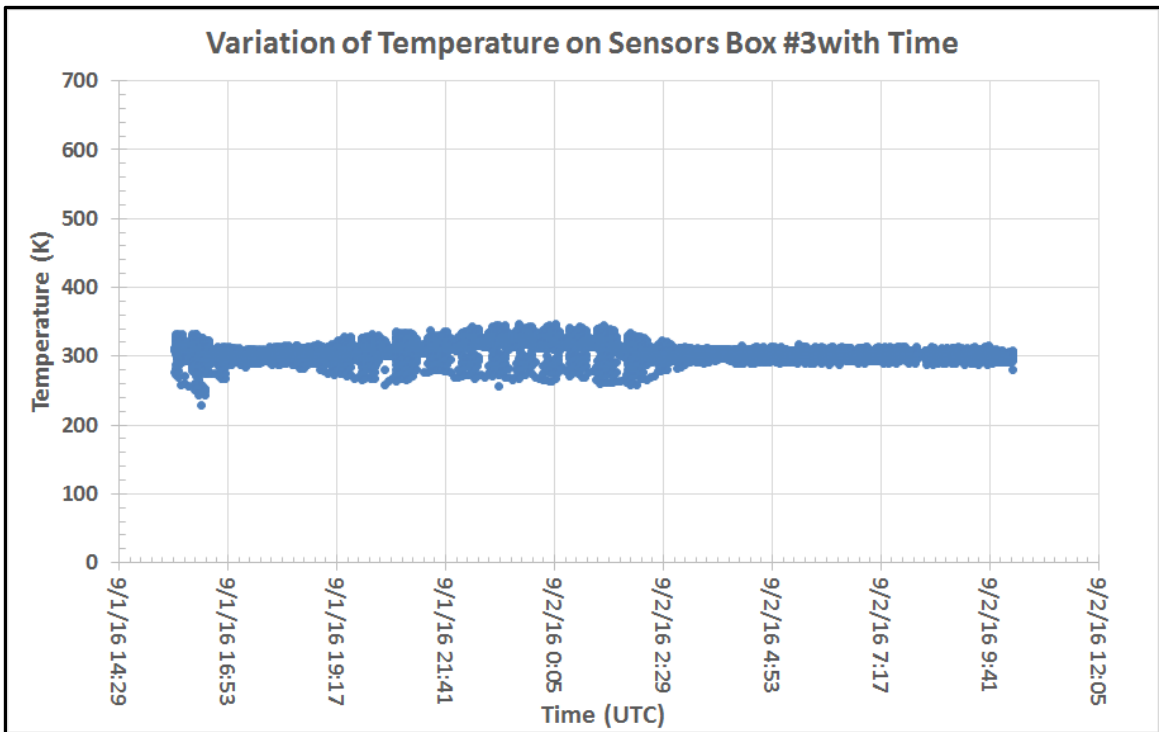


Fig.30 (c) Variation of temperature of ozone sensors in box#3 with time (UTC)

The variation of temperature on central processing unit (CPU) of a microprocessor chip was also measured with altitude and is shown in fig.31. The average temperature  $\pm$  standard deviation was about  $295 \pm 24$  K. The variation in temperature was observed during due to change of day to night as well as change in altitude too. In addition, the temperature of CPU was reasonably stable within standard deviation. Thus, the thermal stability of our payload is proved and good.

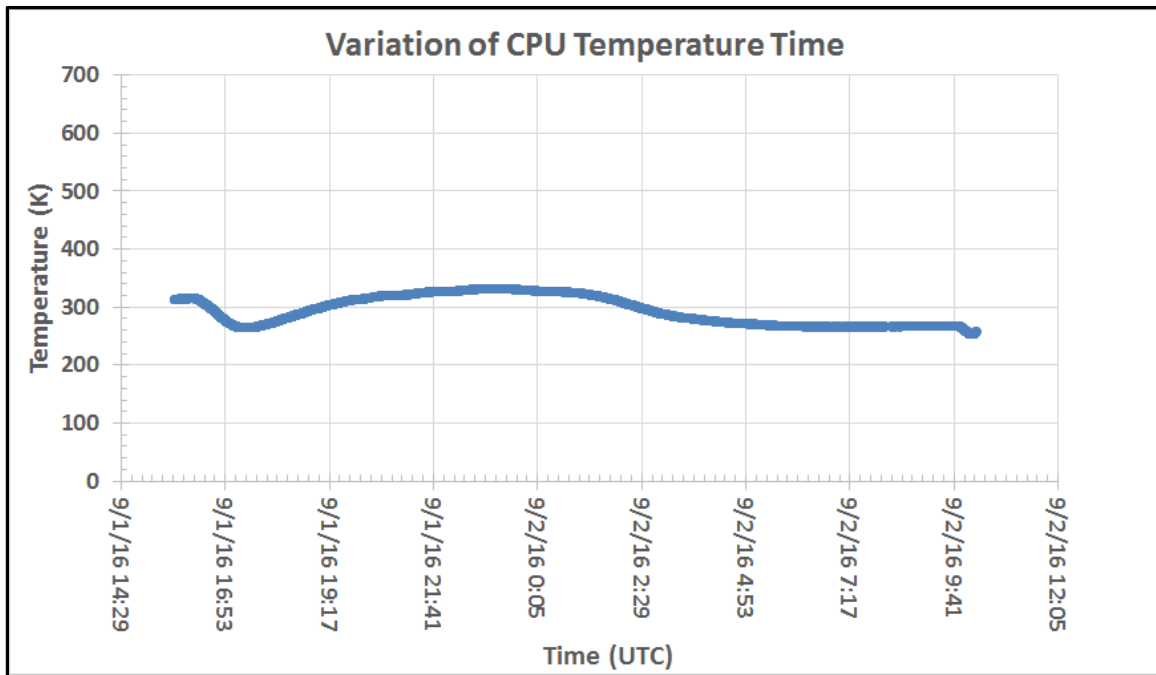


Fig.31 shows variation of temperature on CPU with altitude.

## 9.5 Measurements of photovoltage profile during the flight

The variation of photovoltage generated by the photo diodes mounted on sensor box #1, 2 and 3 during the flight is shown in fig 32 (a), (b) and (c), respectively. It was observed that measured photovoltage was larger in the altitude range from 15,000 to 25,000 m. The larger photovoltage confirmed the presence of ultra violet Sun light. In the presence of that UV light oxygen converted into ozone gas. It was also observed a secondary small peak after termination of the flight. The larger photovoltage confirmed the presence of ultra violet Sun light. In the presence of that UV light oxygen converted into ozone gas.

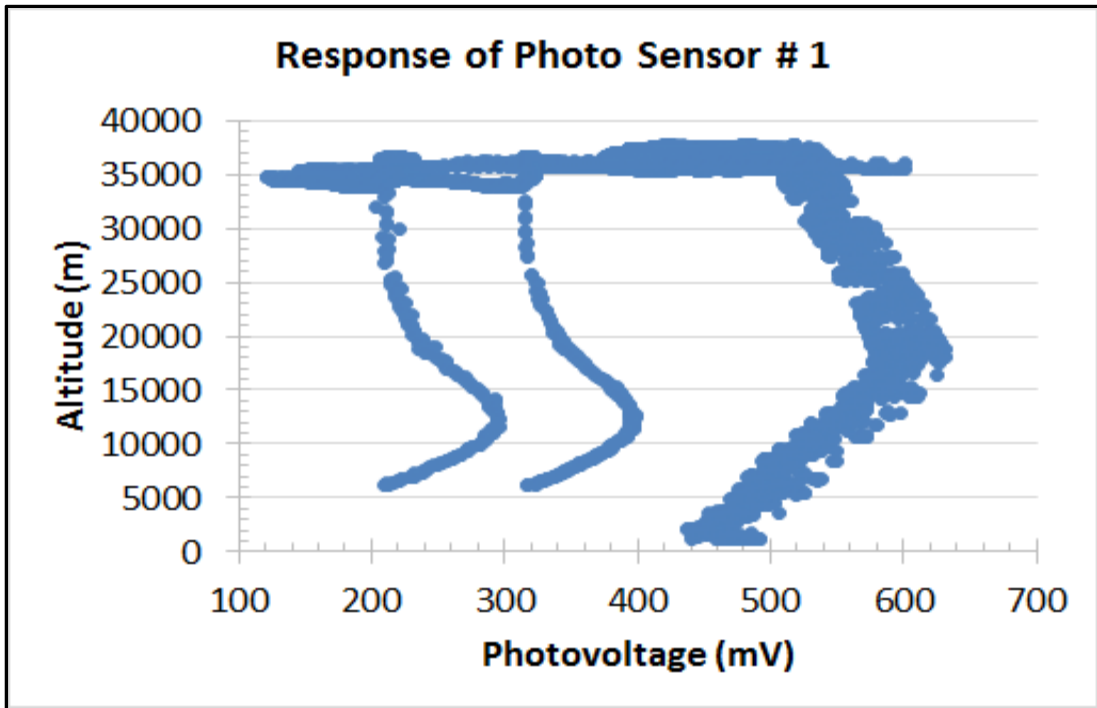


Fig.32 (a) Variation of photovoltage on sensor box#1 (S1)

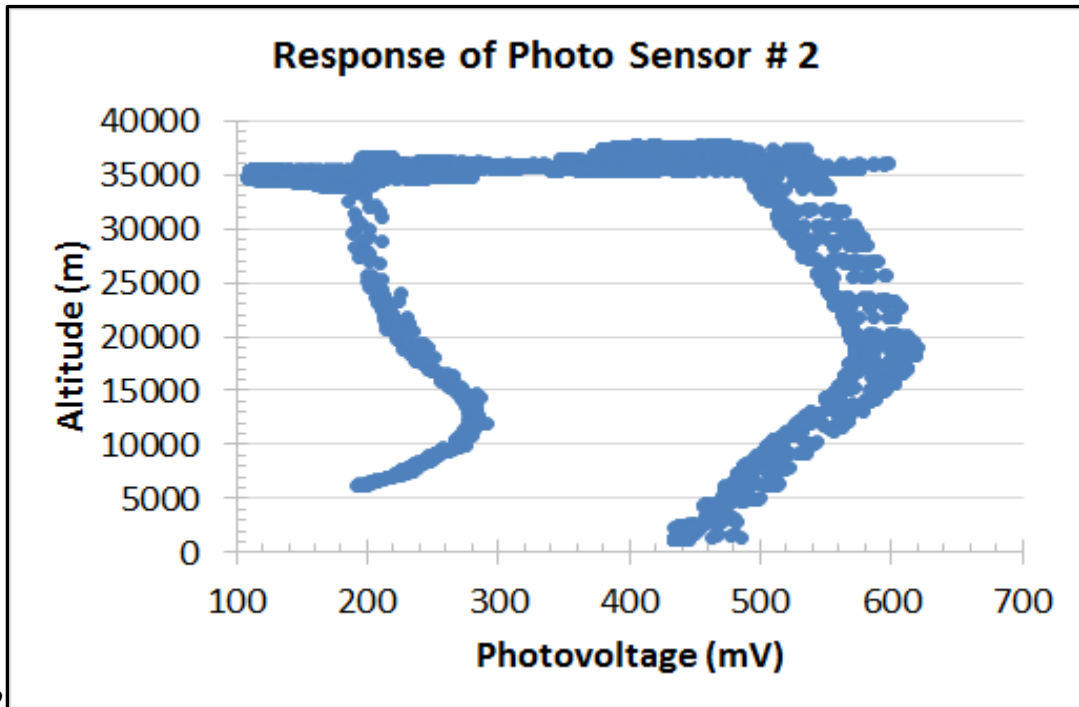


Fig.32 (b) Variation of photovoltage on sensor box#2 (S2)

32

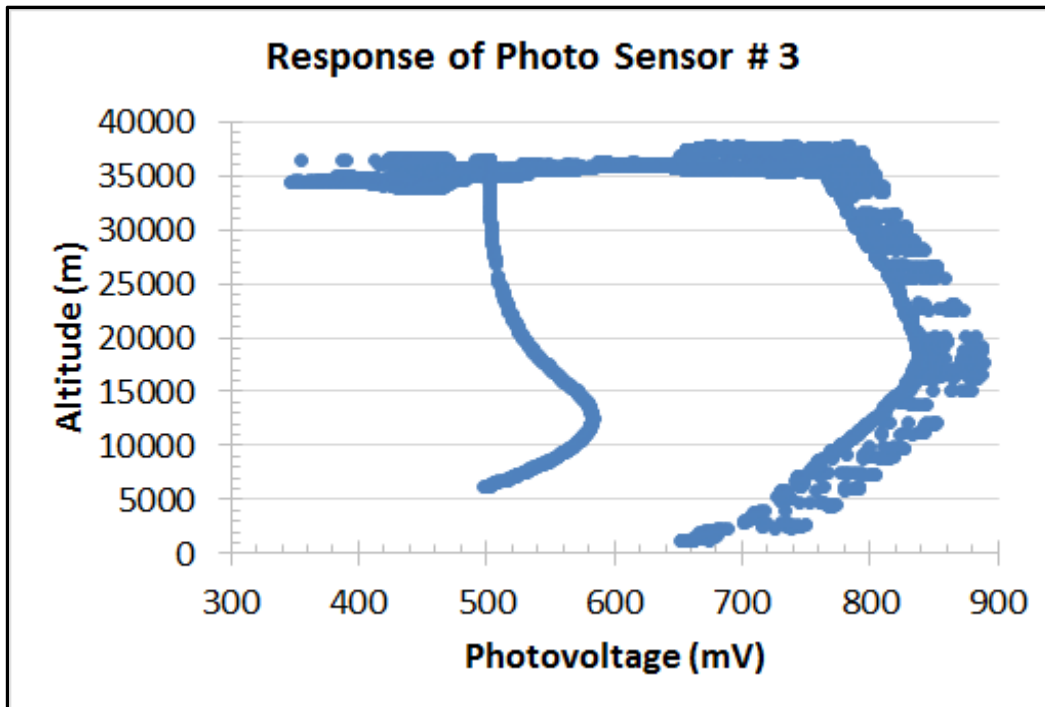


Fig.32 (c) Variation of photovoltage on sensor box#3 (S3)

The variation of photovoltage generated by the photo diodes mounted on sensor box #1, 2 and 3 with the flight time (UTC) is shown in fig 33 (a), (b) and (c), respectively. Four major zones are shown in Fig. 33 as (i) ascending during day, (ii) float during day, (iii) float during night and (iv) termination. The photovoltage voltage was maximum and shown a peak in the middle of stratosphere. The photovoltage has several spikes during float in day time due to the balloon flight was traveling towards east direction. The photovoltage was decreased and stable during float in the night time. The small peak of photovoltage was observed during after termination of flight and descend journey of flight towards the Earth surface. All three photo sensors have nearly similar response. Photo sensor #3 has large magnitude of photovoltage due to higher sensitivity of compare to that of other two photo sensors # 1 and 2. Photo sensors #3 was new GaP (FGAP71) UV photodiode was purchased from [http://www.thorlabs.com/newgrouppage9.cfm?objectgroup\\_id=285&pn=FGAP71](http://www.thorlabs.com/newgrouppage9.cfm?objectgroup_id=285&pn=FGAP71).

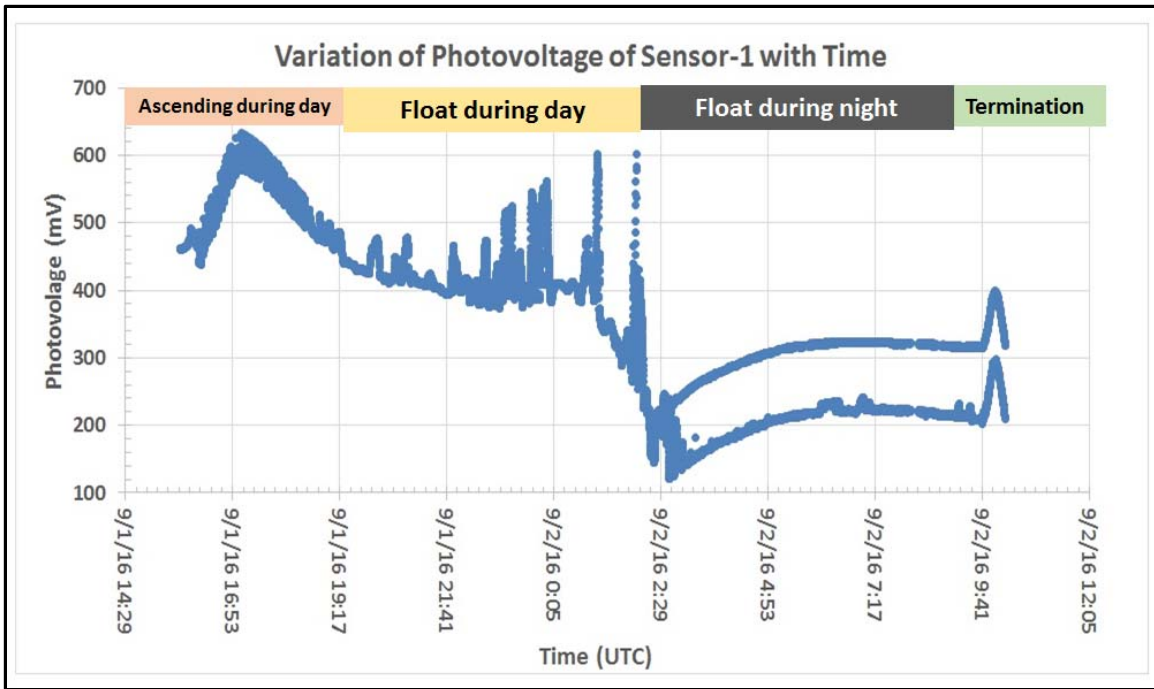


Fig.33 (a) Variation of photovoltage on sensor box#1 with time

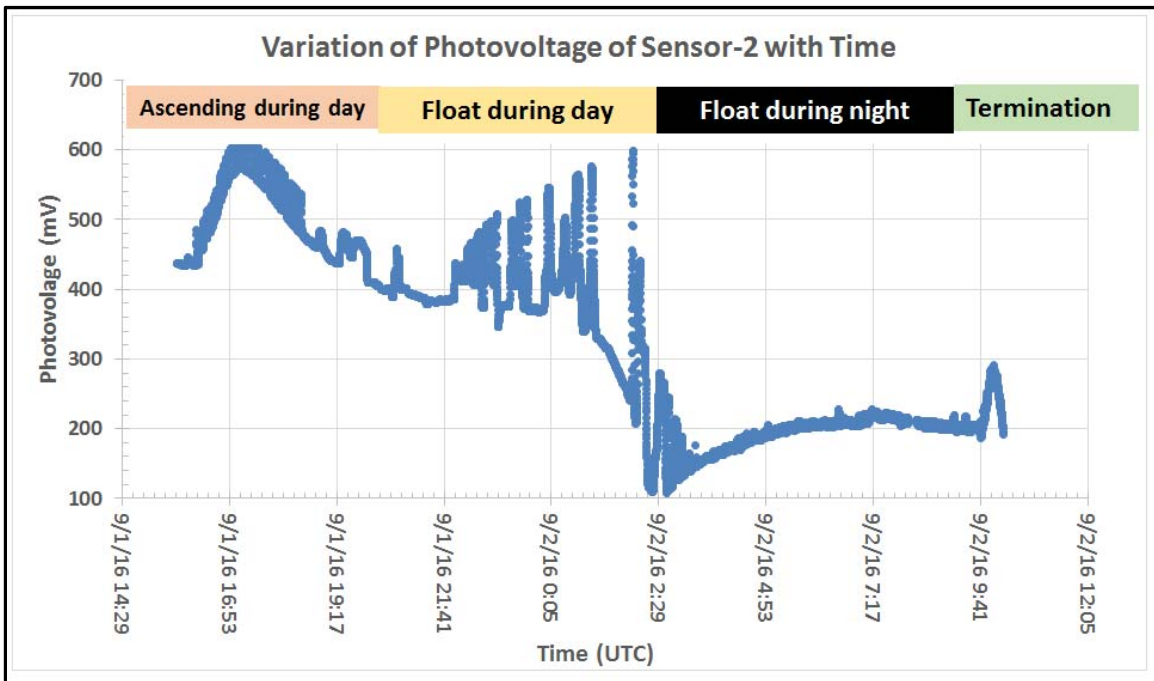


Fig.33 (b) Variation of photovoltage on sensor box#2 with time

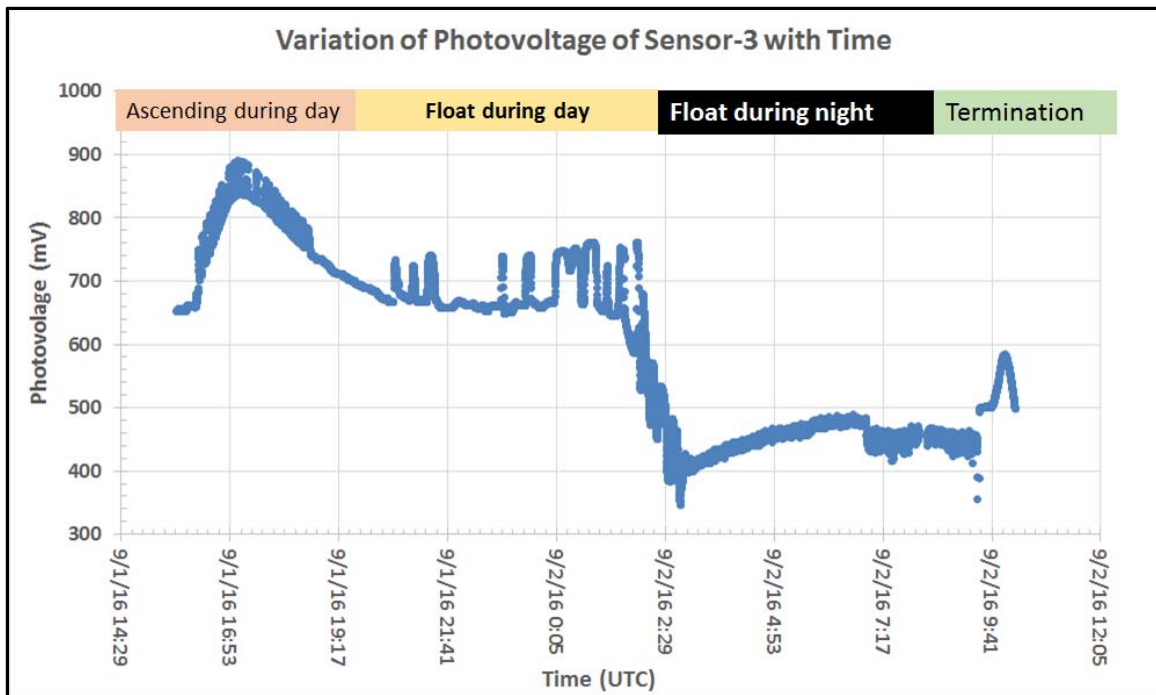


Fig.33 (c) Variation of photovoltage on sensor box#3 with time

## 9.6 Discussion of Response of Gas Sensor Profile

Sensor # S1-4 was randomly picked for the discussion of response of ozone sensor with the entire range of altitude of balloon. Sensors of Box-1 (S1) were made of improved version of nanocrystalline ITO thin films compare to our previous balloon flights. These sensors have better selectivity and sensitivity with ozone gas. Fig. 34 show the response of ozone sensor # S1-4 of **Box#1** (#S1) in terms of variation of measured resistance of sensor #S1-4 with altitude (Fig. 34 (a) and variation of measured concentration of ozone by sensor #S1-4 (Fig. 34(b)) during the entire flight. Note that the calibration algorithm for each layer such as Atmosphere, Troposphere and Stratosphere were applied to determine the concentration of ozone in the entire range of altitude

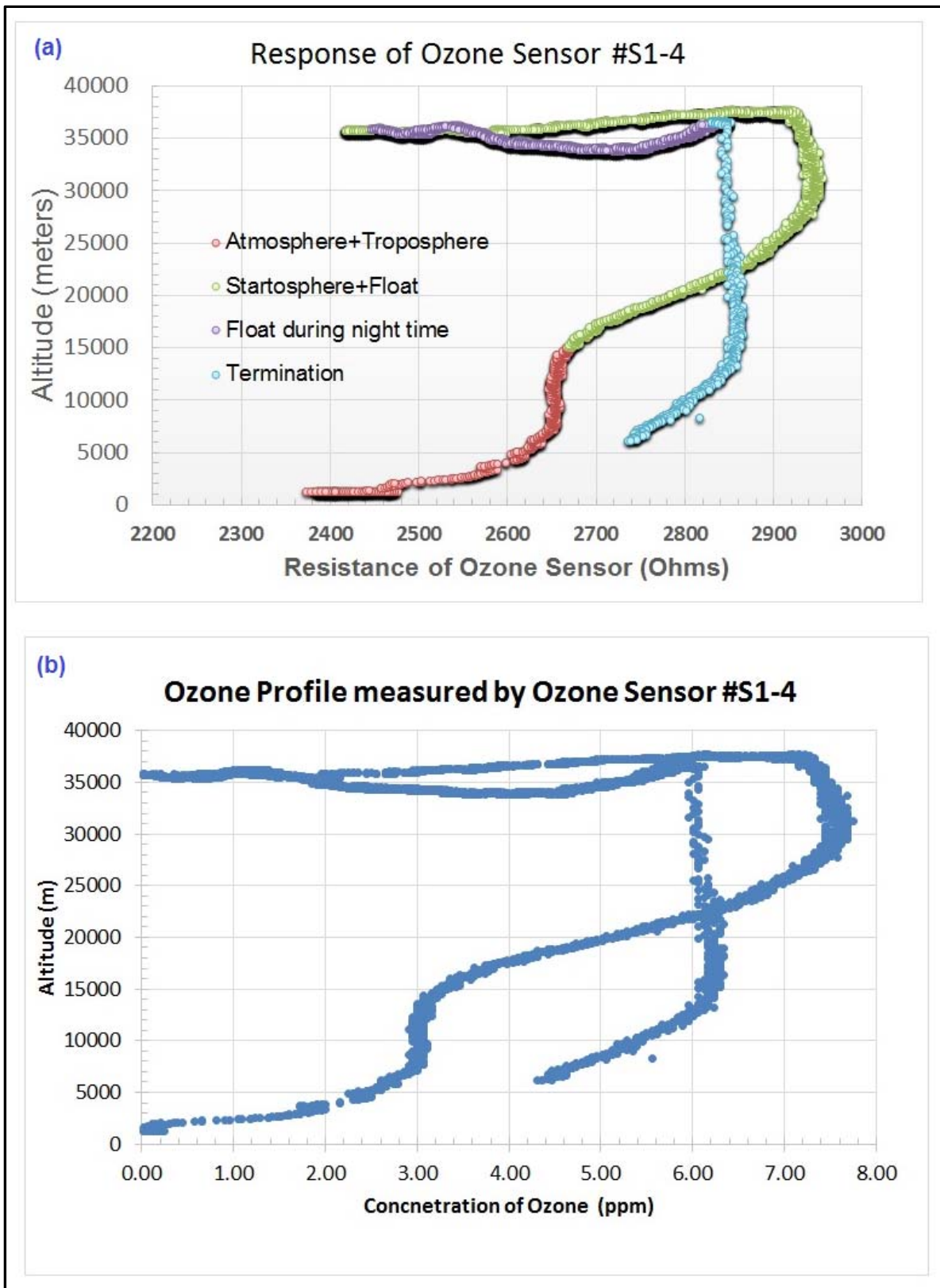


Fig. 34 (a) and (b) Response of ozone sensor of **Box#1** (#S1) with the entire range of altitude

Small peak of ozone (red color part in fig. 34 (a)) was observed during ascending of balloon flight at the altitude below 15000 m. This range of altitude is in the troposphere. This small ozone peak is known as the bad ozone, which is mainly due to the generation of smog in the early morning due to pollution by the automobile vehicles and industries. Note that there was no effect of cold temperature on sensor because the temperature of gas sensors was controlled and maintained to about 293 to 308 K. The amount of anthropogenic ozone in this zone is very low compared to that of good ozone in the stratosphere. There may be possibility of some error in applying trend line equation to the data in the troposphere due to interference of pollutant gases.

The bigger peak of ozone is observed at altitude above 25000 m to 37000 (green color part in fig. 34(a)). This is due to the ozone in the stratosphere. This ozone is known as good ozone. In the presence of ultra violet light from Sun, oxygen converted into ozone gas. The concentration of ozone is higher in the middle of stratosphere in the presence of ultra violet light. Ozone is oxidizing gas and its concentration depends on amount of available Sun light. Upon adsorption of charge accepting molecules at the vacancy sites from ozone oxidizing gas, the electrons are effectively depleted from the conduction band of n-type Indium Tin Oxide (ITO) semiconductor sensor. Thus, this leads to an increase in the electrical resistance of n-type ITO gas sensor. At the maximum float of balloon, the concentration of ozone should be constant, but it may vary due to mixing ratio and availability of ultra violet rays from the sunlight during day time. The concentration of ozone decreased slowly (purple color part in fig.34 (a)) during float at the night time. After termination of balloon, the payload again entered into the middle of stratosphere, the resistance of sensor should again increase and then decrease. Therefore, a small peak was observed after termination of the balloon flight (blue color part in the fig.34 (a)). All eight sensors (S1#1 to S1#8) of box-1 have nearly same nature of ozone peak in the stratosphere.

Fig. 35 (a) show the variation of resistance of ozone sensor # S1-4 of **Box#1** (#S1-1) with time (UTC) and Fig. 35(b) shows the variation of measured concentration of ozone by sensor with time (UTC) during the entire flight.



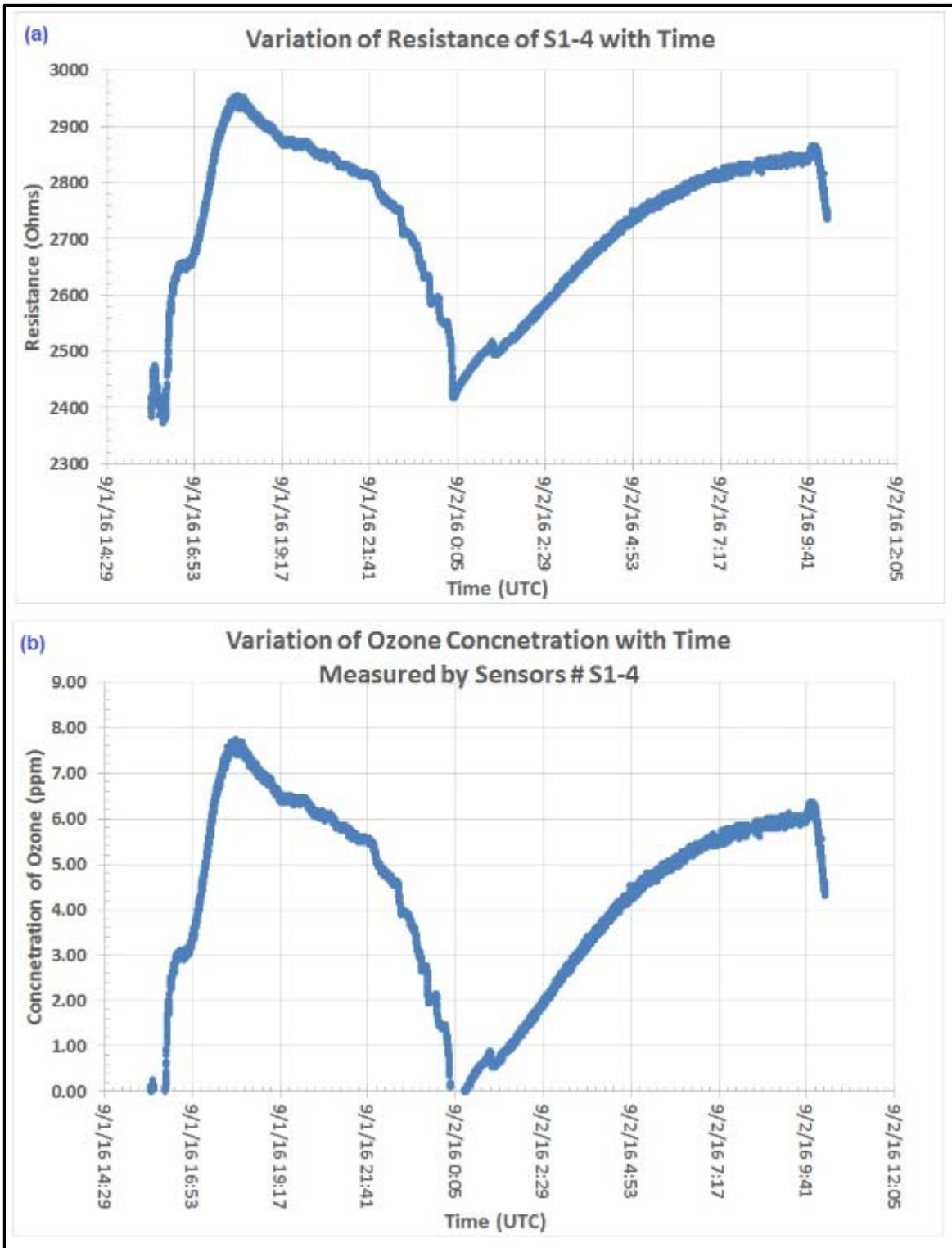


Fig. 35 (a) Variation of resistance of ozone sensor #S1-4 with time (UTC) and Fig.35 (b) variation of measured concentration of ozone by sensors S1-4 with time (UTC).

Response of sensors of box-2 was also similar to box-1 as shown in Figs.36 (a) and (b) and Figs.37 (a) and (b). Sensors of Box-2 were made of nanocomposite of ZnO + ITO thin films. Both sensors boxes #1 and 2 have good selectivity of ozone gas in the stratosphere compare to that other pollutant gases in the atmosphere and troposphere.

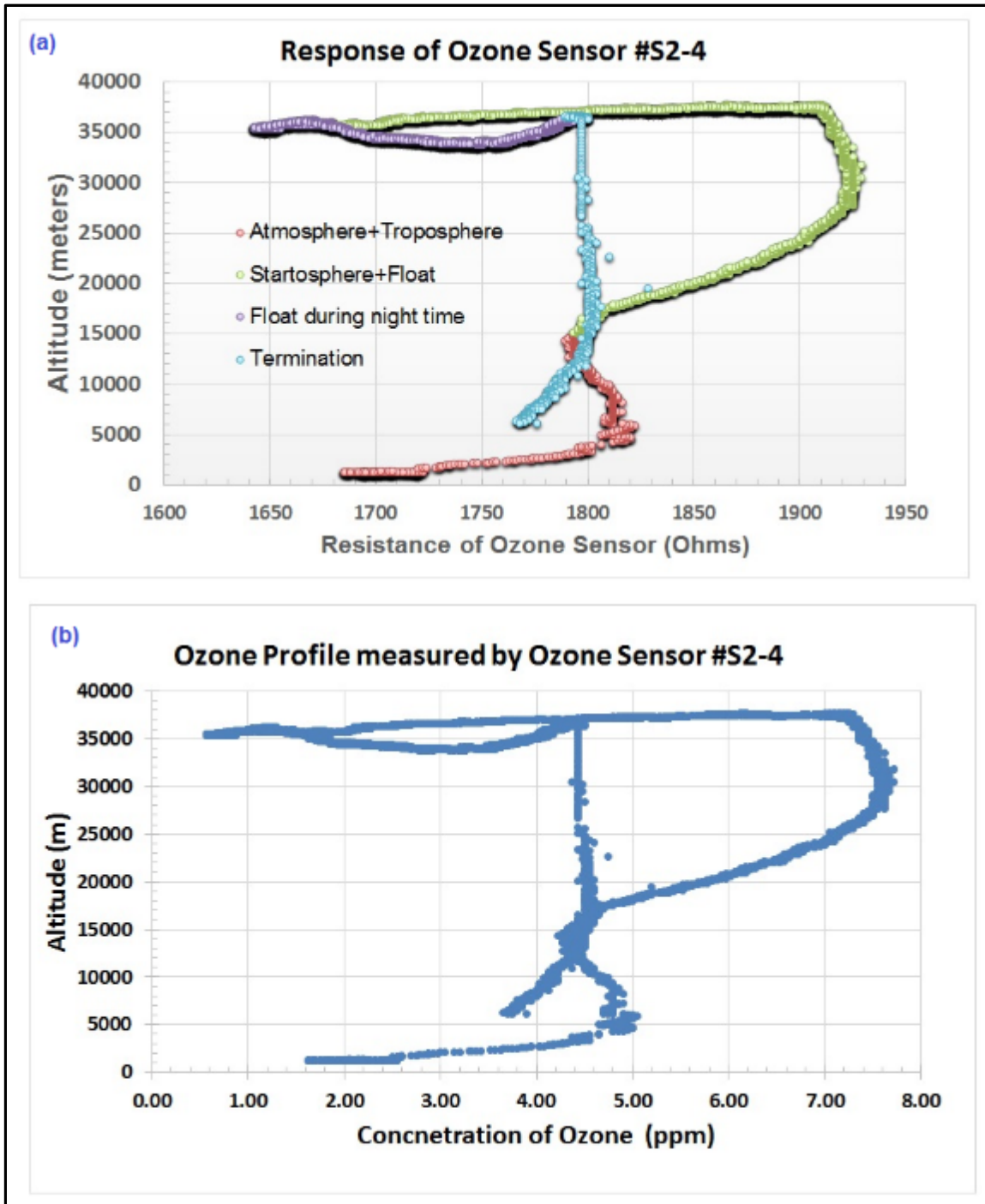


Fig. 36 (a) and (b) Response of ozone sensor of **Box#2** (#S2) with the entire range of altitude

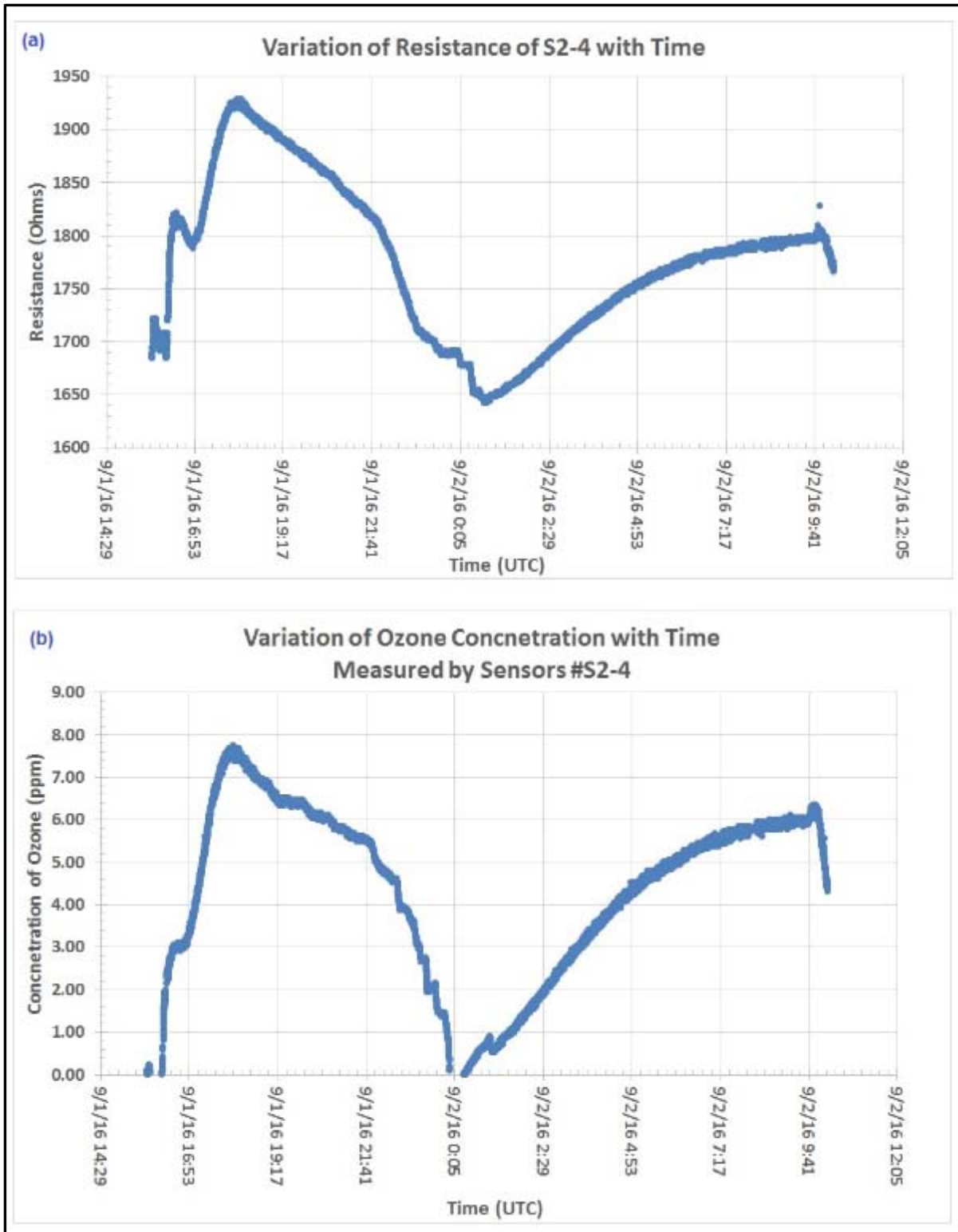


Fig. 37 (a) Variation of resistance of ozone sensor #S2-4 with time (UTC) and Fig.37 (b) variation of measured concentration of ozone by sensors S2-4 with time (UTC).

Sensors box-3 was made of ITO+SnO<sub>2</sub> nanocrystalline thin film. These sensors are n-type semiconductor. We have made new composite for Sensors box #3 in order to enhance smog peak in the troposphere due to the pollutant gases and also to detect ozone gas in stratosphere. We are still on trial and error stage for our objective of sensors box #S3. All 8 sensors (S3-1 to S3-8) have shown the similar nature of response.

## **9.7 Response of ozone sensors during the flight**

Response of all eight ozone sensors of box #1 (S1) with the entire range of flight altitude are shown in fig.38 (a) , while response of ozone sensors in the stratosphere are shown in Fig. 38 (b).

Response of all eight ozone sensors of box #2 (S2) with the entire range of flight altitude are shown in fig.38 (c) , while response of ozone sensors in the stratosphere are shown in Fig. 38 (d).

Response of all eight ozone sensors of box #3 (S3) with the entire range of flight altitude are shown in fig.38 (e) , while response of ozone sensors in the stratosphere are shown in Fig. 38 (f).

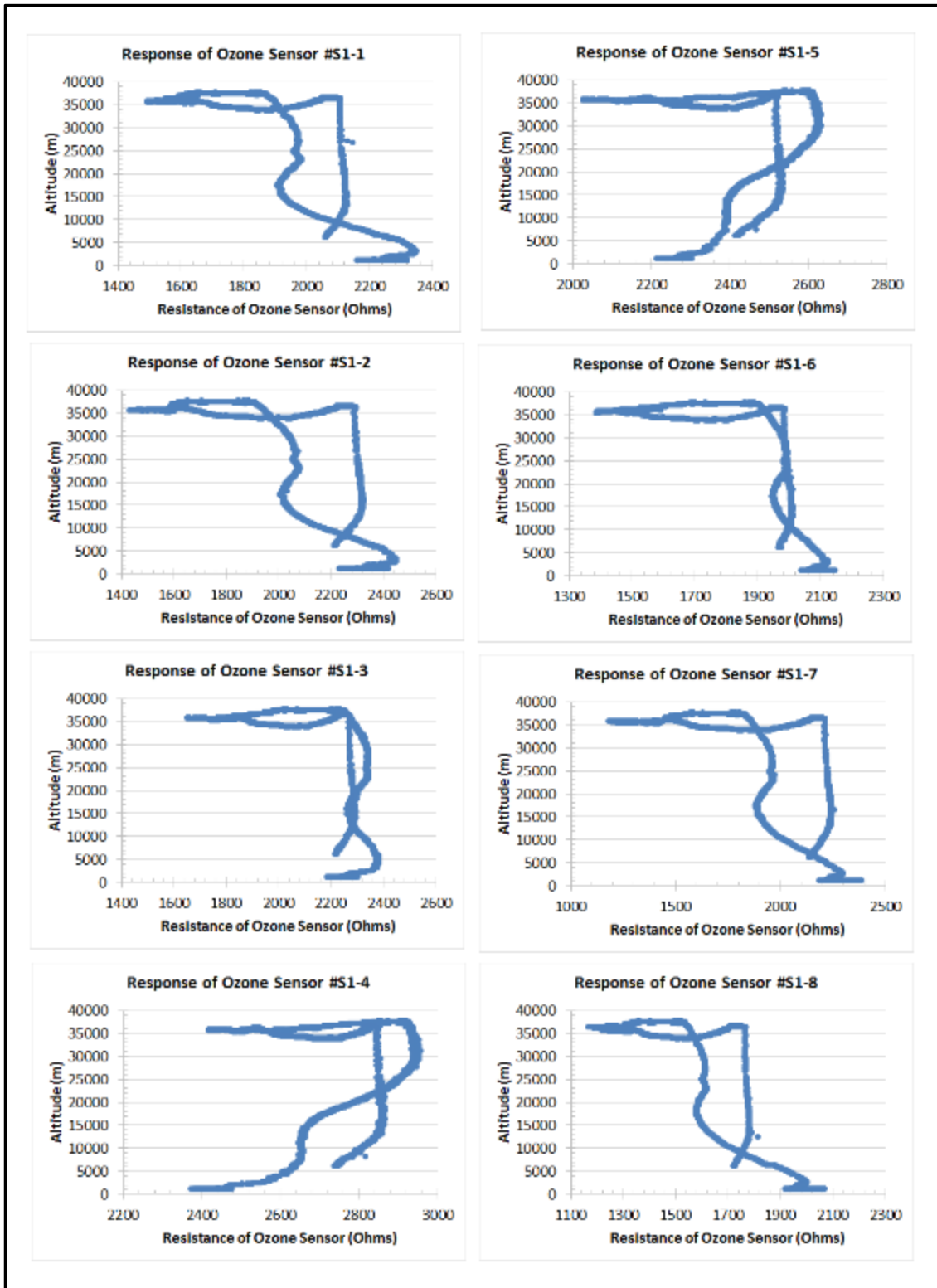


Fig.38 (a) Response of all ozone sensors of box #1 (S1) with the entire range of flight altitude.

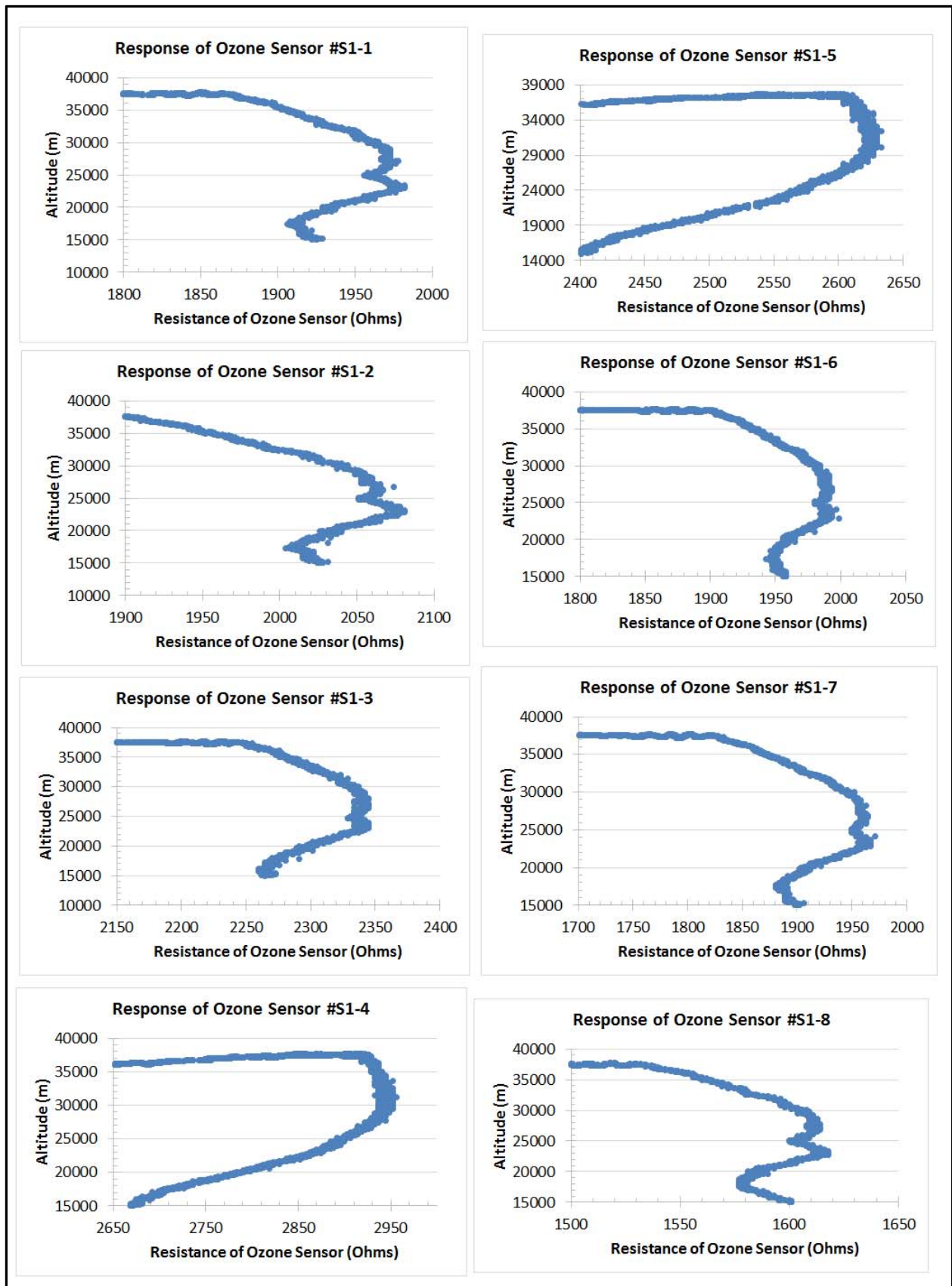


Fig.38 (b) Response of all ozone sensors of box #1 (S1) in the stratosphere altitude range

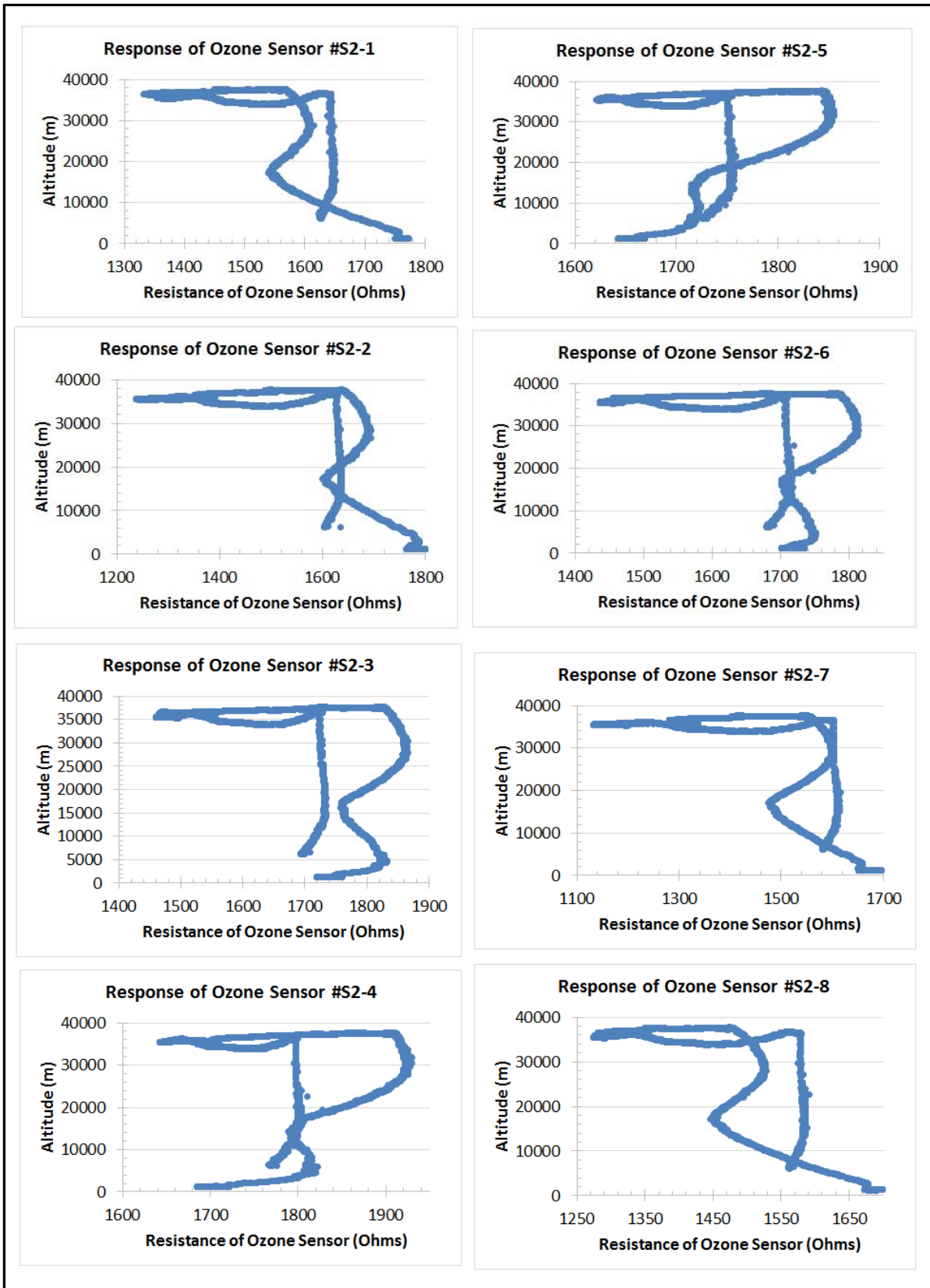


Fig.38 (c) Response of all ozone sensors of box #2 (S2) with the entire range of flight altitude.

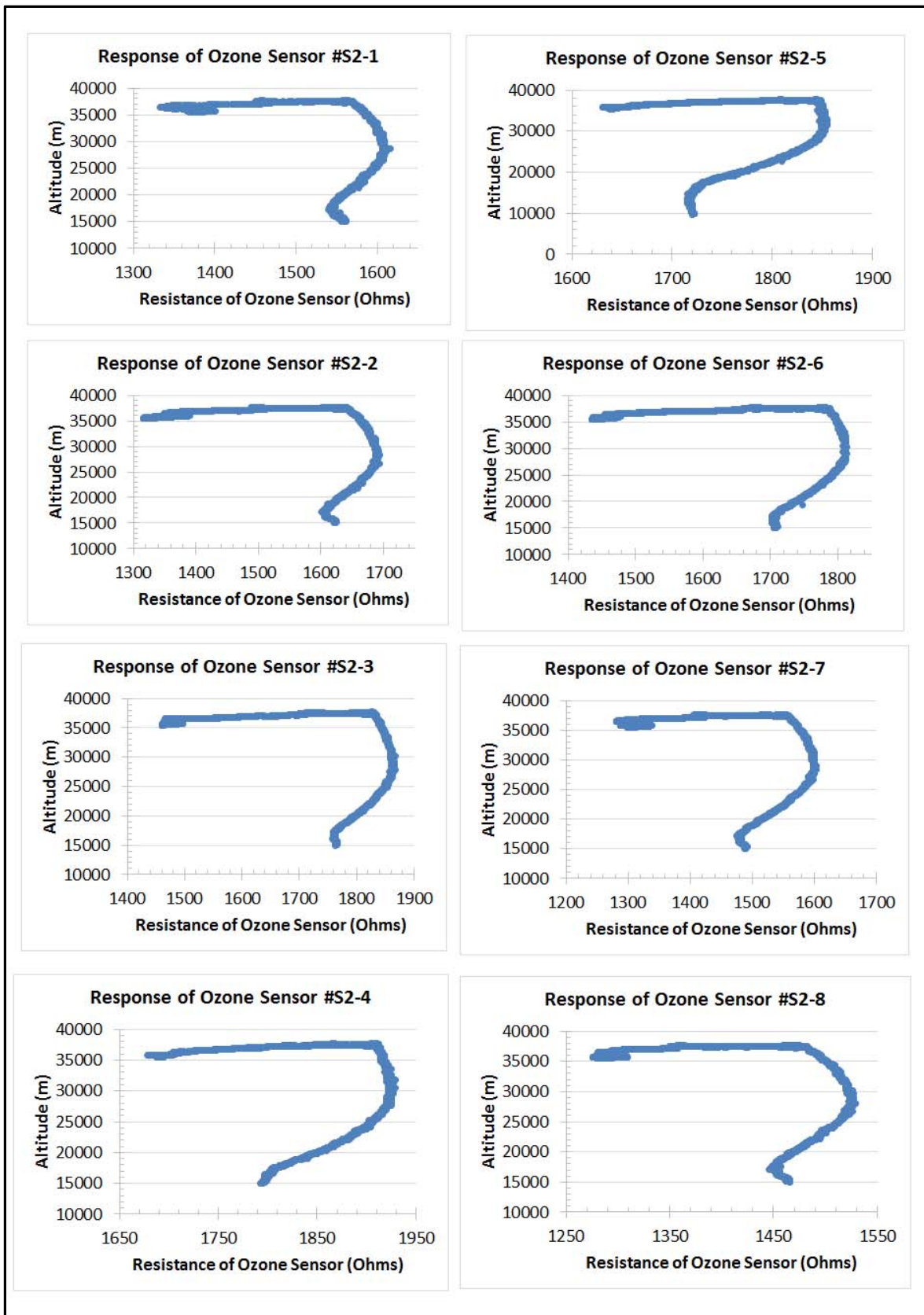


Fig.38 (d) Response of all ozone sensors of box #2 (S2) in the stratosphere altitude range



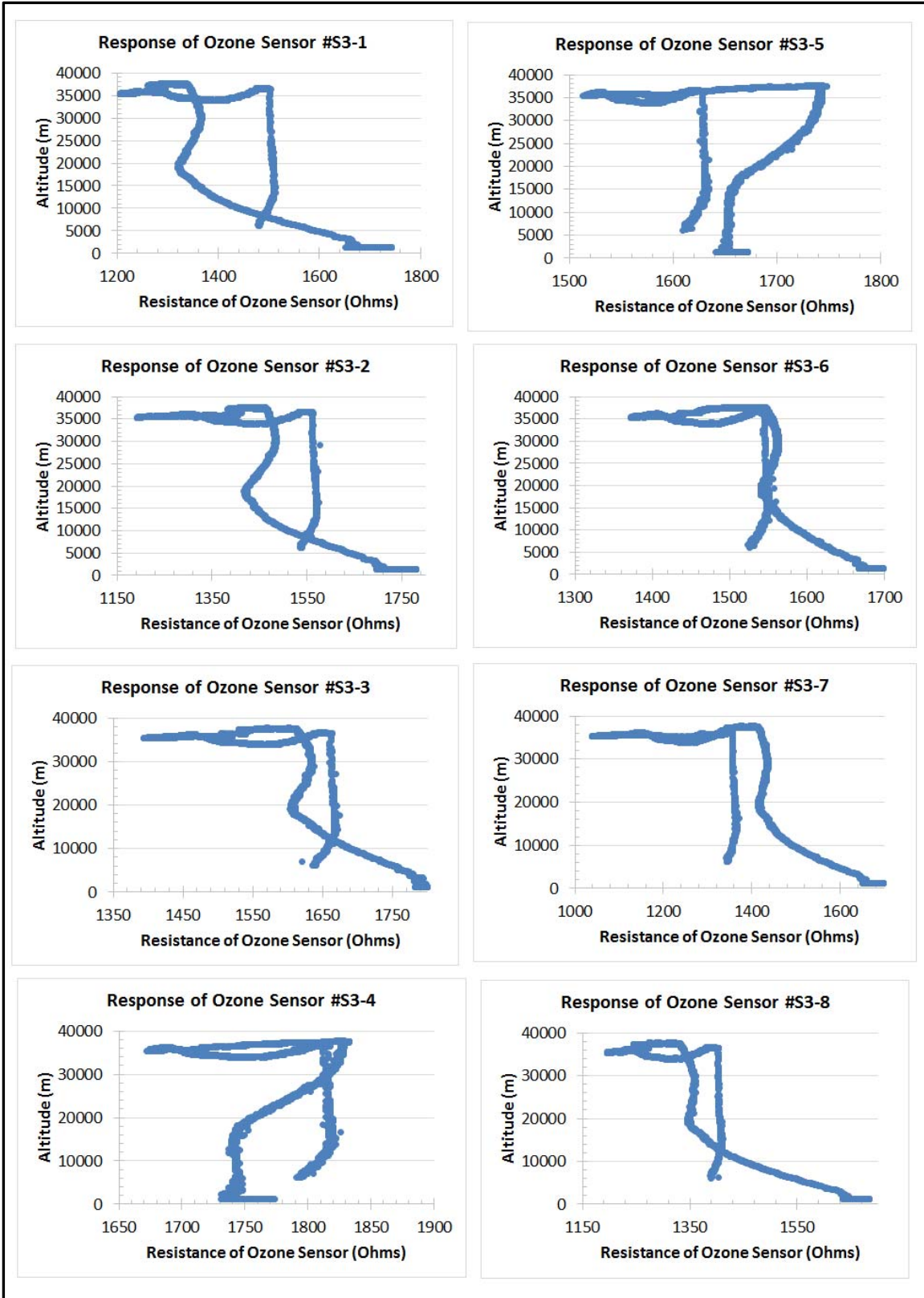


Fig.38 (e) Response of all ozone sensors of box #3 (S3) with the entire range of flight altitude.

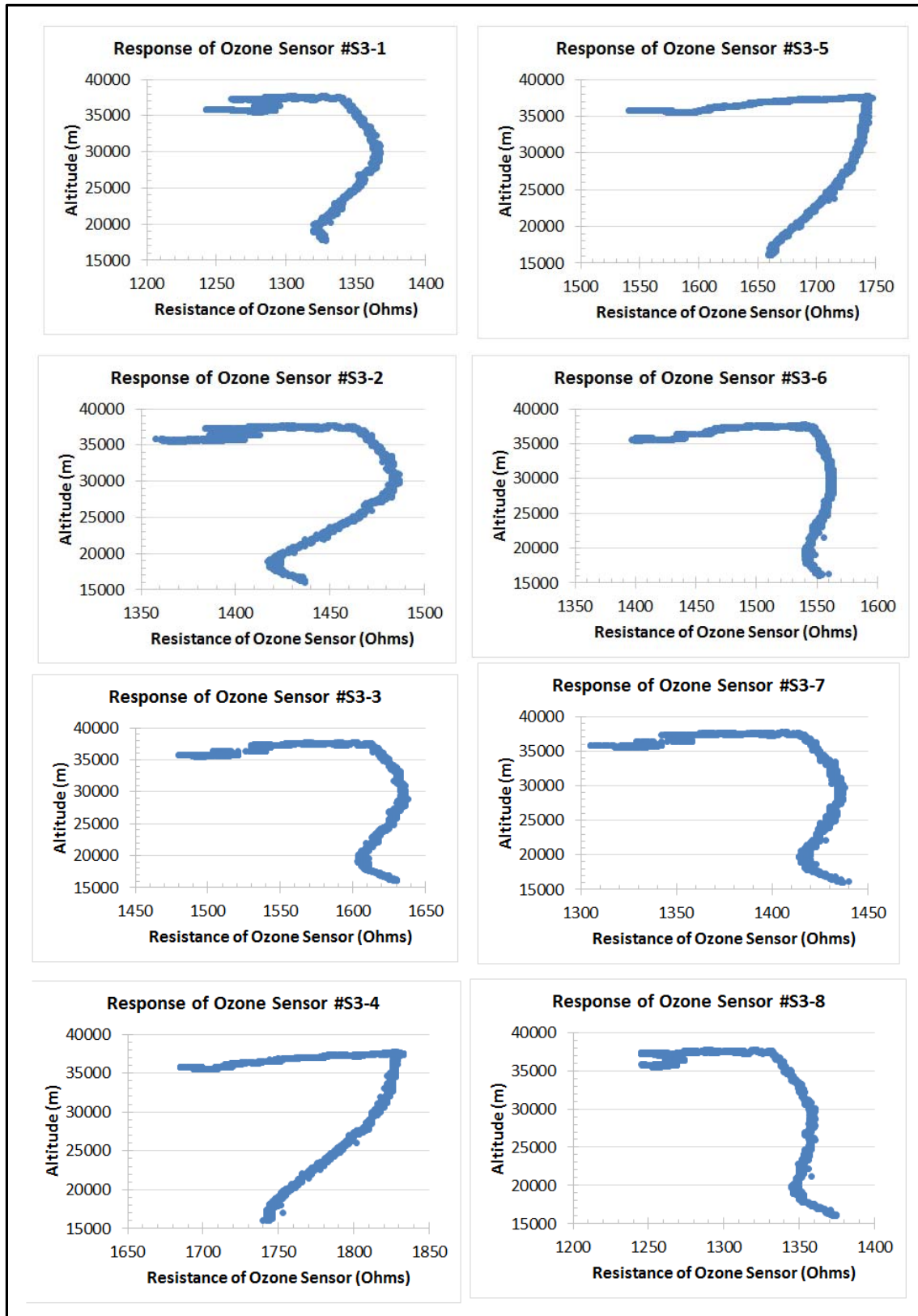


Fig.38 (f) Response of all ozone sensors of box #3 (S3) in the stratosphere altitude range

All sensors of the three boxes have shown the ozone peak in the stratosphere.

## 9.8 Measurements of ozone profile in the stratosphere and comparison with the theoretical profile

We focused mainly to measure the ozone profile in the stratosphere.

Using calibration plots shown in fig. 7(a), (b), and (c), the trend line equation of plot of each sensor was applied to convert the resistance values of the sensors into concentration of ozone gas in ppm.

Note that the calibration was made in the low pressure, which can be applied mainly to stratosphere range. It may not be good for atmosphere data. The ozone concentration measured from 0 to 10.0 ppm may have slight different value of slope and y intercept due to experimental error due to the variation of sensors thickness and leakage in the chamber.

The trend line equation of the calibration plot is given as:

$$y \text{ (sensor resistance, ohms )} = [m \text{ (slope). } x \text{ (concentration of ozone, ppm)}] + b \text{ (y intercept)}$$

$$\text{The concentration of ozone gas can be determined by: } x = (y - b)/m$$

The trendline equations for each sensors were listed in the following table-4.

Table-4 Trend line equations determined from the calibration plots shown in fig.7 (a), (b) and (c) of sensor box # S1, S2 and S3.

Sensor Box # S1				Sensor Box # S2				Sensor Box # S3			
Sensor Number	Slope (m)	y intercept (b)	Coreleation Coefficient (R <sup>2</sup> )	Sensor Number	Slope (m)	y intercept (b)	Coreleation Coefficient (R <sup>2</sup> )	Sensor Number	Slope (m)	y intercept (b)	Coreleation Coefficient (R <sup>2</sup> )
S1-1	25.04	1799.7	0.99998	S2-1	13.52	1510.1	0.9999	S3-1	15.02	1254.8	0.9999
S1-2	25.07	1899.8	0.9999	S2-2	17.98	1560.1	0.9999	S3-2	14.01	1380.0	0.9999
S1-3	19.24	2200.0	0.9999	S2-3	17.99	1730.1	0.9998	S3-3	14.82	1520.0	0.9998
S1-4	26.54	2750.0	1	S2-4	18.34	1790.1	0.9999	S3-4	15.10	1640.1	0.9999
S1-5	24.50	2450.2	0.9999	S2-5	17.99	1720.2	0.9999	S3-5	15.10	1630.1	0.9999
S1-6	18.01	1860.1	0.9998	S2-6	17.99	1675.1	0.9999	S3-6	13.70	1460.1	0.9999
S1-7	18.02	1829.8	0.9999	S2-7	18.11	1459.9	0.9999	S3-7	13.98	1330.3	0.9999
S1-8	15.02	1499.8	0.9999	S2-8	17.21	1400.0	0.9999	S3-8	13.85	1256.0	0.9998

With these equation parameters, we obtained the following the ozone profile plots shown in fig.39 (a), (b) and (c):

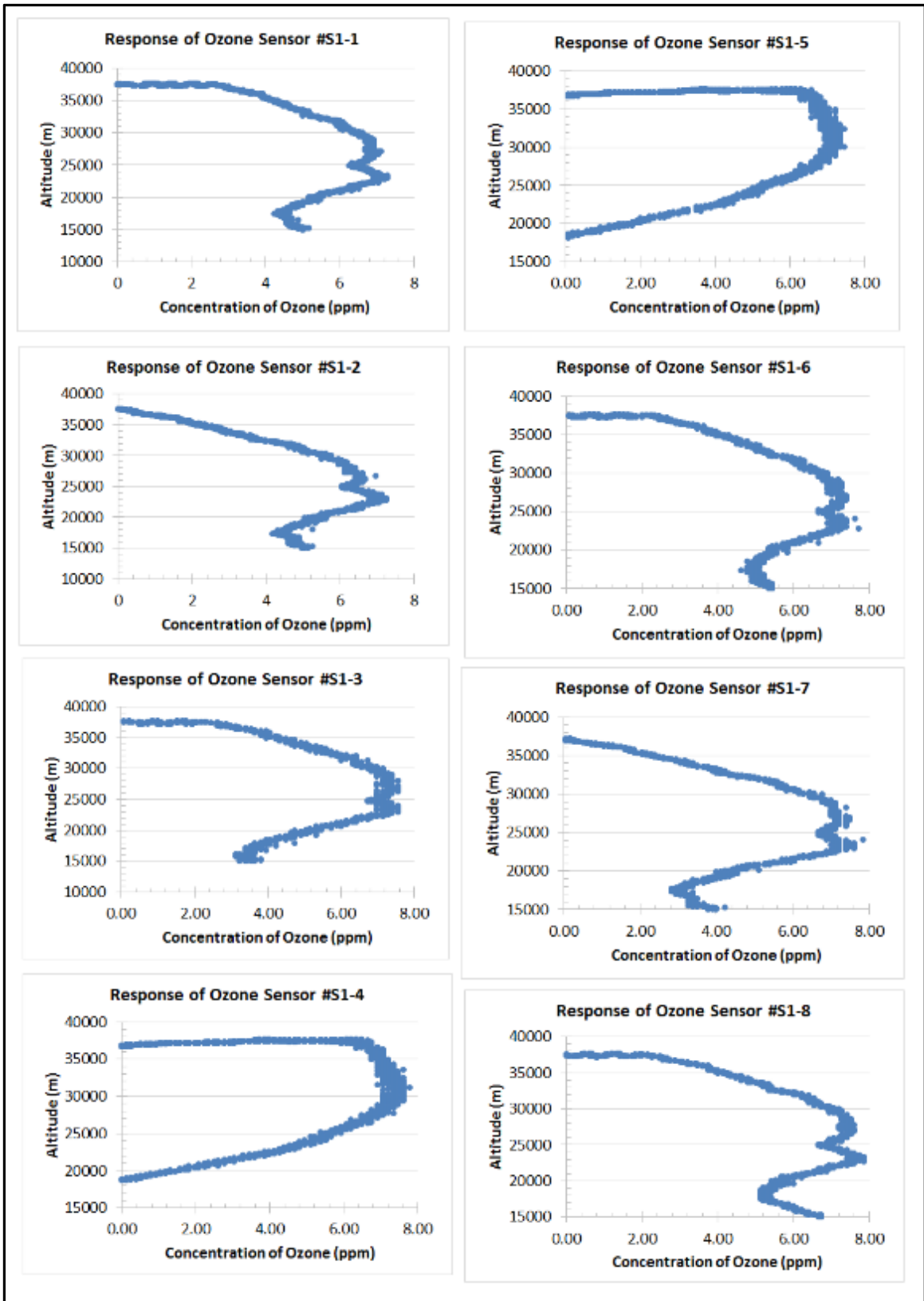


Fig. 39 (a) Ozone profile measured by sensors # S1-1 to S1-8.

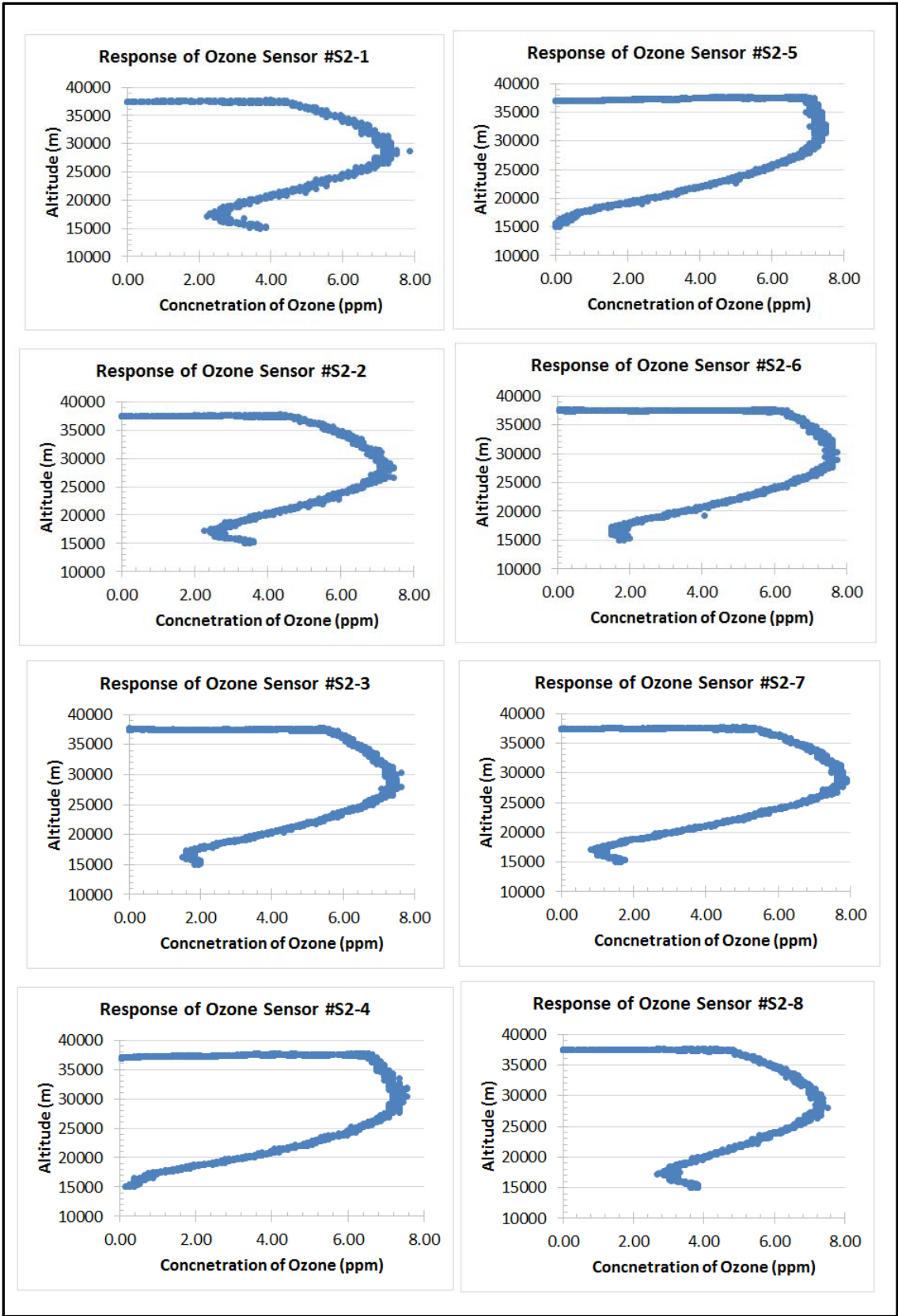


Fig. 39 (a) Ozone profile measured by sensors # S2-1 to S2-8.

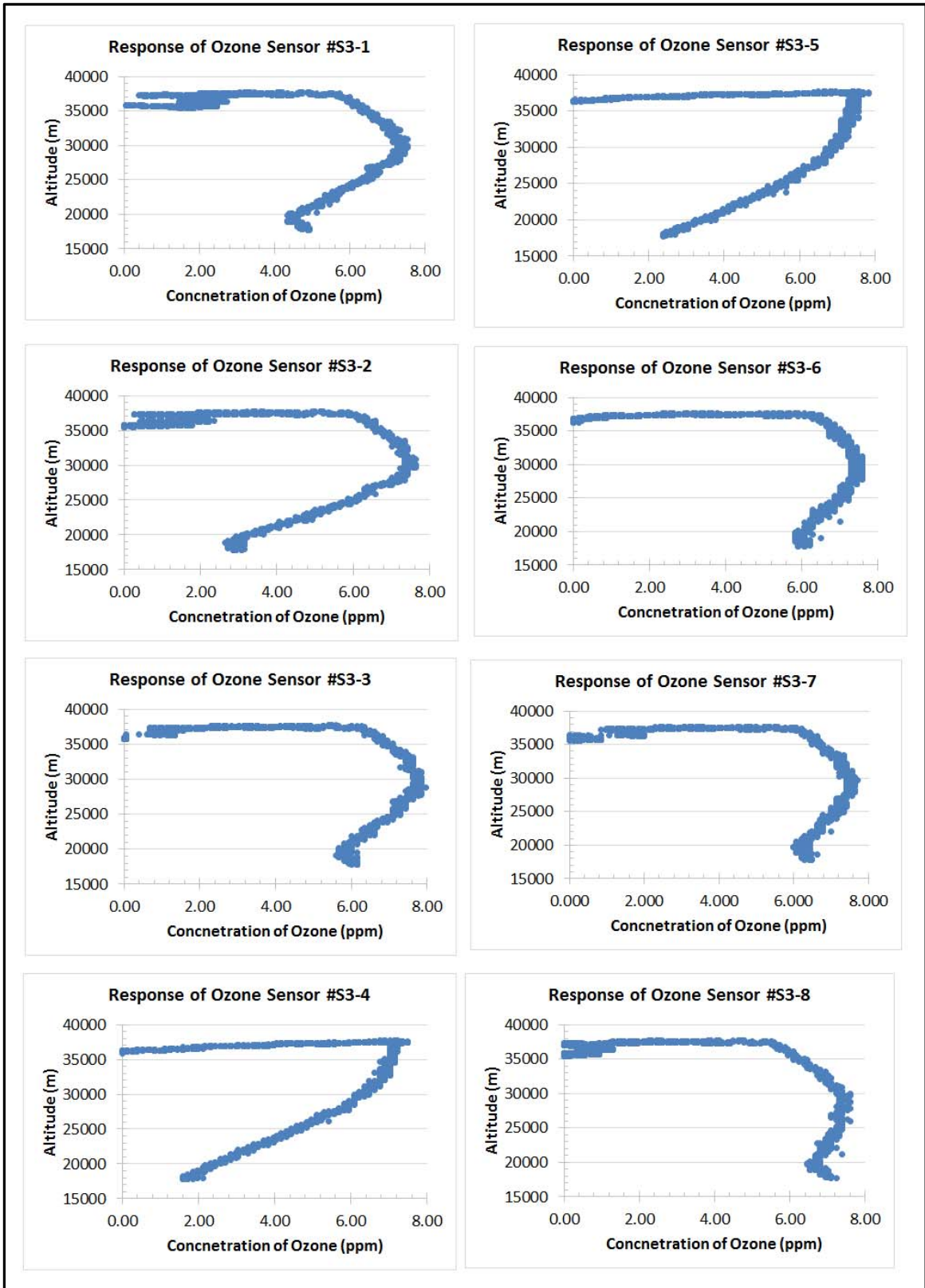


Fig. 39 (a) Ozone profile measured by sensors # S3-1 to S3-8.

The nature of ozone profiles measured by ozone sensors box #1 ,2 and 3 are nearly matched with the theoretically profile measured and quoted by various research groups, which are shown in Fig. 40(a) to (d) for the comparison purpose. The measured value of maximum concentration of ozone was observed about 7.8 ppm, which is very close to the expected values. Compare to previous year, the maximum value of ozone concentration is about 0.2 to 0.3 ppm less. This may be due to the fact that the thunder storm was build up and rain in NM region during August 30 to September 2, 2016. We will find out some theoretical calculation method to generate theoretical data for comparison.

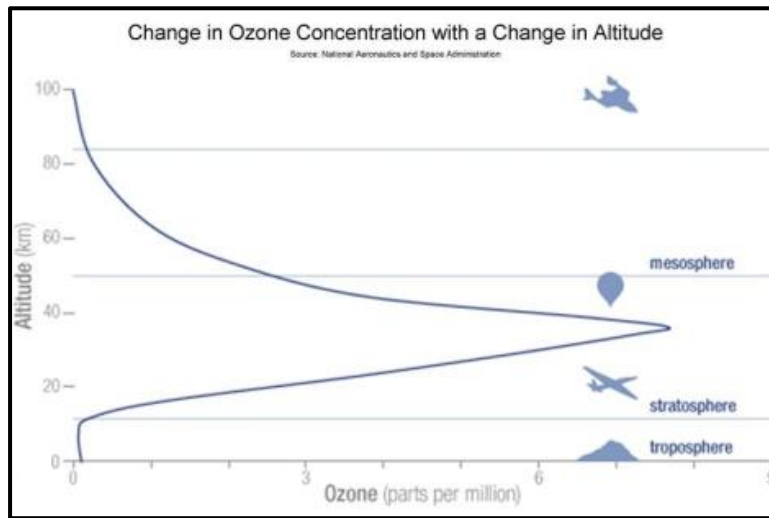


Fig.40 (a) Change in ozone concentration with a change in altitude.

Courtesy: <http://sites.gsu.edu/geog1112/lab-2-part-2/>

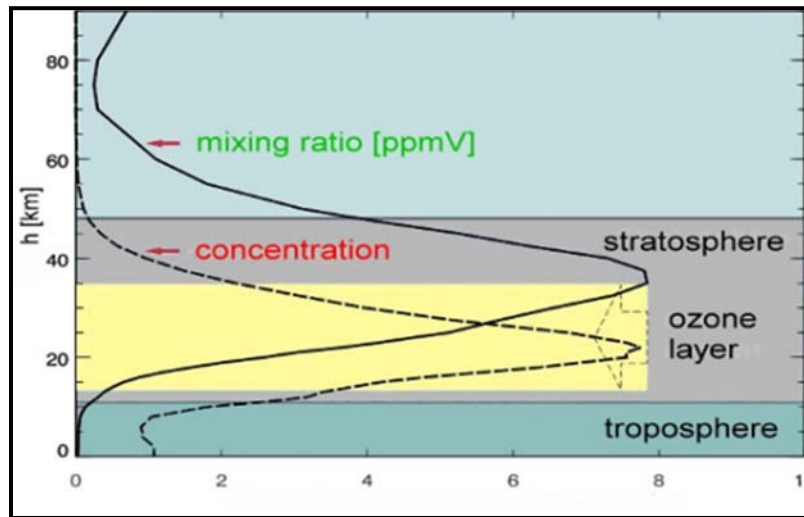


Fig.40 (b) Theoretical ozone profile in stratosphere

Courtesy: <http://www.atmosphere.mpg.de/enid/1yy.html>

(ppmv = parts per million by volume = volume mixing ratio)

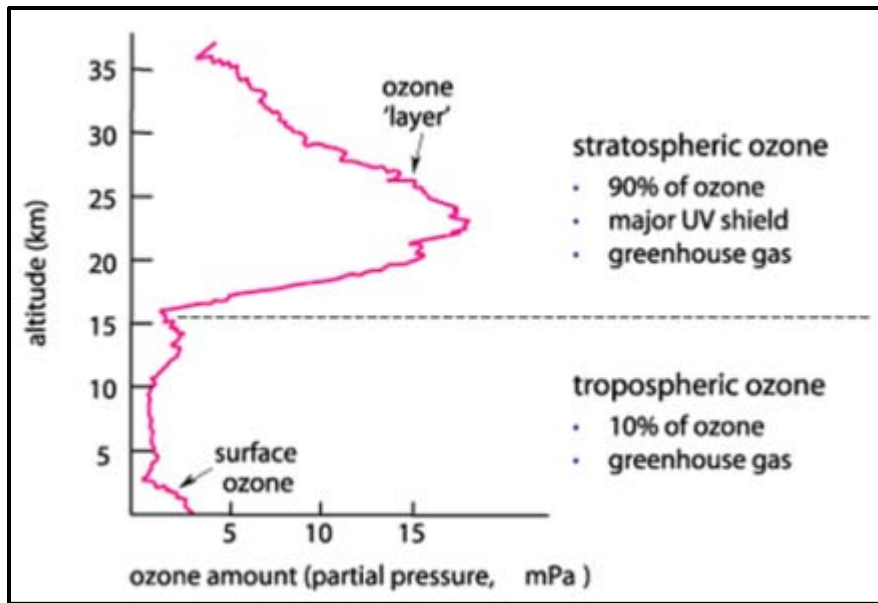


Fig.40(c) Ozone in the atmosphere with its impact

<http://www.environment.gov.au/soe/2001/publications/theme-reports/atmosphere/atmosphere03-1.html>

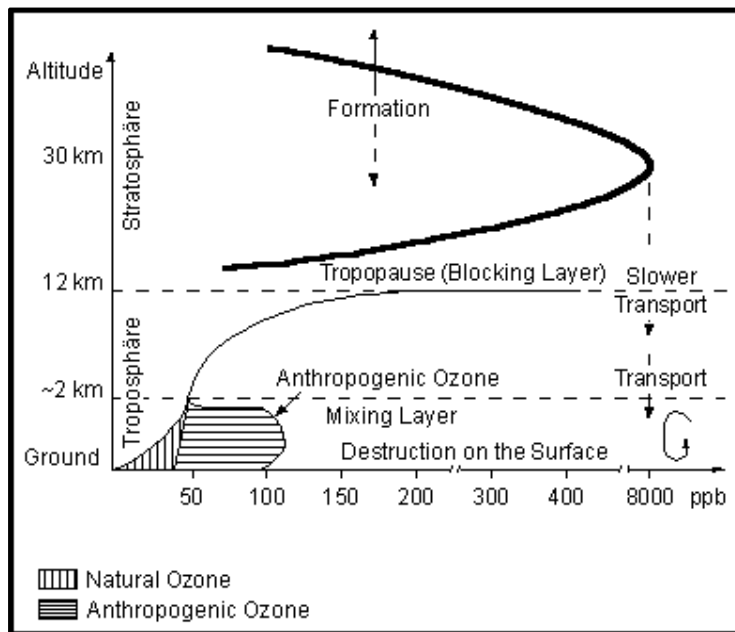


Fig.40 (d) Ozone profile

Courtesy: [http://www.stadtentwicklung.berlin.de/umwelt/umweltatlas/ed306\\_01.htm](http://www.stadtentwicklung.berlin.de/umwelt/umweltatlas/ed306_01.htm)



## 10. Problems, failure analysis and future plan

- (1) Pressure sensor was saturated at 110 mbar. We found that that pressure sensor can work only up to 110 mbar. We planned to replace it by new pressure sensor in the next flight.
- (2) Our nanocrystalline ozone gas sensors (Box # 1 and 2) worked well for measurement of ozone profile. We made new composite of ITO+SnO<sub>2</sub> to enhance detection of ozone in the stratosphere as well as smog in atmosphere / troposphere. Sensors of box #3 worked satisfactory. We will continue to improve the performance of sensors.
- (3) We did not able to add a radio circuit in the payload to communicate data in addition to HASP communication link in order to develop *a free flying payload*. This is because tight time schedule and limited budget. We will try to add it in the next flight.
- (4) We will add one external temperature sensor and humidity sensor mounted on outside of the payload body to measure ambient temperature and humidity.
- (5) We are working on development of nano sensors using an electron beam lithography technique ([www.raith.com](http://www.raith.com)) attached with scanning electron microscope. We are interested to examine the performance of nano sensors. We may try it in the next flight 2017.

## 11. Conclusions:

- (i) We got very good data during the flight. The payload worked very well during the flight.
- (ii) We have reduced the mass of the payload by 500 grams by reducing the height of the payload body.
- (iii) Our UBLOX GPS worked well without any issue.
- (iv) The improved nanocrystalline ITO thin film gas sensors (Box#1) and nanocomposite ZnO+ITO thin film gas sensors fabricated (Box#2) by the UNF team have good selectivity with ozone gas and worked well during entire flight period and measured the ozone profile of the stratosphere. Nanocomposite ITO+SnO<sub>2</sub> thin film gas sensors (Box#3) have satisfactory response with ozone in stratosphere as well as smog in atmosphere-troposphere.
- (v) Light sensor proved the presences of UV light, which are responsible to generate more ozone gas by converting oxygen into ozone.

- (vi) Improved temperature control circuit and software program gave better stability of temperature of sensors during entire flight period. No need to upload the commands during the flight.
- (vii) Our science objectives of all sensors were successfully tested and scientifically verified. We will further improve the performance of our gas sensors and payload during next HASP2017 flight.
- (viii) New modified JAVA based software handles all sensors data and faster conversion of RAW file into EXCEL file for quick view of the plots and also makes the real-time monitoring the plots using LabVIEW.
- (ix) After recovery of payload, we tested the payload, circuit and all sensors and found all parts in good working condition.
- (x) UNF team is interested to make further improve sensors payload and seeking another opportunity for the HASP 2017 flight.

## **12. Acknowledgements**

We are very grateful to

- (i) Dr. Gregory Guzik and Mr. Michael Stewart, HASP-LSU for their continuous help, cooperation and encouragement. We also appreciate help of Mr. Doug Granger for his support and sharing temperature data and pictures. We also thankful to Mr. Doug Smith for his cooperation during the thermal vacuum test.
- (ii) Columbia Scientific Balloon Facilities (CSBF)-NASA, Palestine TX and Fort Sumner, NM, and their team.
- (iii) Florida Space Grant Consortium for providing the support to UNF team.
- (iv) Dr Jaydeep Mukherjee, Director, Florida Space Grant Consortium (FSGC) and Ms. Sreela Mallick, FSGC for their valuable help and encouragement.
- (v) Websites links mentioned in this report for using their pictures to explain the science of this report. Our intention is not to violate any copyright, but only education and research purposes

### 13. Presentation of Research work

- (i) Dr. Nirmal Patel presented an invited talk on “HASP Balloon flight for students’ payloads” in the Florida Space Grant Consortium Advisory Board Meeting on October 13, 2016 at the Kennedy Space Center, FL.
- (ii) UNF students made presentation of a poster on “Ozone Sensors Payload and its Applications on NASA High Altitude Balloon 2016 Flight” at the UNF Biology, Chemistry and Physics 2016 Poster Session on Friday November 4, 2016 at the Sciences & Engineering building #50 of UNF.

